Chemical Engineering Journal 528 (2026) 170938

Contents lists available at ScienceDirect

Chemical Engineering Journal

journal homepage: www.elsevier.com/locate/cej

Review

# A comprehensive review of pristine Pebax-1657 membranes for $CO_2$ gas separations

Dionysios S. Karousos [a,*,1], George V. Theodorakopoulos [a,1], Xuezhong He [b,c], George Em. Romanos [a], Adele Brunetti [d], Evangelos P. Favvas [a,*]

[a] Institute of Nanoscience and Nanotechnology, National Center for Scientific Research "Demokritos", Aghia Paraskevi, 15341, Athens, Greece
[b] Department of Chemical Engineering, Guangdong Technion - Israel Institute of Technology, 241 Daxue Road, Shantou, Guangdong, 515063, PR China
[c] Guangdong Provincial Key Laboratory of Materials and Technologies for Energy Conversion, Guangdong Technion - Israel Institute of Technology, Shantou, Guangdong, 515063, PR China
[d] National Research Council - Institute on Membrane Technology (CNR-ITM), Rende, Cosenza 87036, Italy

ARTICLE INFO

*Keywords:*
Pebax-1657
Membranes
Gas separation
$CO_2$ capture
Polymeric membranes

ABSTRACT

The present review aims to underline the inherent gas separation potential of pristine Pebax-1657, without any chemical modification, nor addition of filler material, by referring to a number of selected outstanding literature results. These results underscore the adequacy of pristine Pebax-1657 membranes in achieving excellent $CO_2$ gas separation performances, within or close to the target area of commercial applicability in terms of techno-economic competitiveness when compared to alternative $CO_2$ separation/capture technologies. These achievements are facilitated by the utilization and combination of cutting-edge membrane preparation techniques. Additionally, the current review provides detailed information regarding material and gas separation properties based on experimental data, which are handpicked from literature and statistically presented to highlight significant differences in reported values. Basic empirical correlations emerging from these data are formulated, in order to provide a guideline for future membrane design, along with clarifications on important claims and points that are often encountered in relevant literature.

## 1. Introduction

Multiblock poly(ether-b-amide) (PEBA) copolymers are represented as a family of thermoplastic elastomers, known under the tradenames PEBAX® (Arkema) and VESTAMID® E (Evonik Industries), that have been proven to be among the most promising candidate materials for use in the gas separation layer of $CO_2$-selective membranes. As presented in the study of Embaye et al. with Robeson plots comparing different PEBA grades [1], current research efforts have primarily focused on Pebax-1657 grade, i.e., characterized by a polyethyleneoxide-*block*-polyamide6 (PEO-b-PA6) structure with PEO:PA6 weight ratio 60:40. This can be attributed to the additional benefit of its solubility in the low-cost, eco-friendly and non-hazardous, green, ethanol/water 70:30 wt% solvent mixture, a feature not commonly shared by almost all other grades (Table S1 in Supplementary). Recent research publications focusing on membranes of this grade are placing significant emphasis on either chemical modification, or mixed-matrix concepts, where co-polymerization [2], or blending with nanoparticles and/or chemical compounds [3–5], are explored in respect to the influence on the final membrane's gas separation properties. The claims of selectivity and/or permeability enhancement are most commonly attributed to mechanisms linked to the chemical modification, or filler material, rather than solely observed under the scope of produced films' quality examination, polymer chain arrangement and polymer's inherent properties. In this regard, the current review attempts to shed light in the direction of giving emphasis on outstanding performances reported for the pristine, neat, polymer material.

In particular, most promising published attempts for preparing high performance PEBA membranes have been achieved so far by forming defect-free ultrathin (sub-micrometer [6]) separation layers on membrane supports, with or without a gutter layer, and specifically on flat sheet geometry supports. In the diagram of Fig. 1a, first published by Jiang et al. [7] in 2021, typical reported $CO_2/N_2$ gas separation performances of such polymeric Pebax and non-Pebax -based membranes

* Corresponding authors.
*E-mail addresses: E-mail address:* d.karousos@inn.demokritos.gr (D.S. Karousos). e.favvas@inn.demokritos.gr (E.P. Favvas).
[1] These authors contributed equally.

https://doi.org/10.1016/j.cej.2025.170938
Received 7 August 2025; Received in revised form 27 October 2025; Accepted 14 November 2025
Available online 17 November 2025

are compared, while in Fig. 1b a more expanded overview is given, yet with $CO_2$ permeability instead of the more practically significant permeance x-scale.

Notably, among top-performing membranes entering the target area of industrial application for $CO_2$-capture from flue gas, Polaris™, developed by Membrane Technology and Research Inc. (MTR) USA, is a Pebax-based membrane with thin-film composite (TFC) structure (Fig. 2) [9,10] and spiral-wound geometry [11]. It is the only Pebax-based membrane that has been demonstrated on the pilot-scale so far (Polyactive™ is not Pebax-based, but a blend of PEG:PBT 77:23 wt%). According to Merkel et al. [12], a PEBA-based membrane with permeance of 1000 GPU and $CO_2/N_2$ selectivity 50 (target area in Fig. 1a) can reach >90 % $CO_2$ capture efficiency from flue gas of coal-fired plant with specific cost less than 30 $/ton $CO_2$, as was set as target by US Department of Energy for the year 2030 [13]. Taking into consideration that, depending on $CO_2$ source and capture technology, today's typical $CO_2$ capture cost ranges are 27–48 $/ton $CO_2$ for concentrated $CO_2$ streams and 50–150 $/ton $CO_2$ for diluted streams [14], a membrane system with a specific cost of 30 $/ton $CO_2$ is highly competitive in respect with mature absorption and adsorbent -based technologies, besides its inherent advantages of much lower space requirement and easier maintenance, given its modularity. However, important recent advances regarding pristine Pebax-1657 membranes, falling within, or close to, the depicted target area of industrial applicability, are not present in the diagram of Fig. 1a and will be mentioned and discussed throughout our review in detail.

## 2. Pebax materials and microstructure

### 2.1. Pebax grades and microstructure

Pebax *block*-copolymer grades comprise the different polyether (PE) and polyamide (PA) building blocks depicted in Fig. 3 in various analogies usually expressed as weight percentages, as shown in Table 1. In particular, the Pebax-1657 grade consists of Poly(ethylene oxide) (PEO) (Fig. 3 (a) with $n$ = 35 repeating units) and poly(ε-caprolactam), commonly known as Nylon 6 or PA6 (Fig. 3 (c) with $n$ = 9 repeating units), building blocks in weight ratio of 60:40, respectively. Its overall molecular structure is represented in Fig. 3 (e).

Depending on the preparation and operational conditions, polymeric membranes derived from the pristine polymer, usually are semi-crystalline materials consisting of both the amorphous and crystalline phases of each building block. A simplified schematic representation of the membrane's microstructure is provided in Fig. 4. The stiff/rigid PA6 building blocks appear as red rods, capable of existing in either an amorphous phase or self-arrange in parallel or folded configurations to

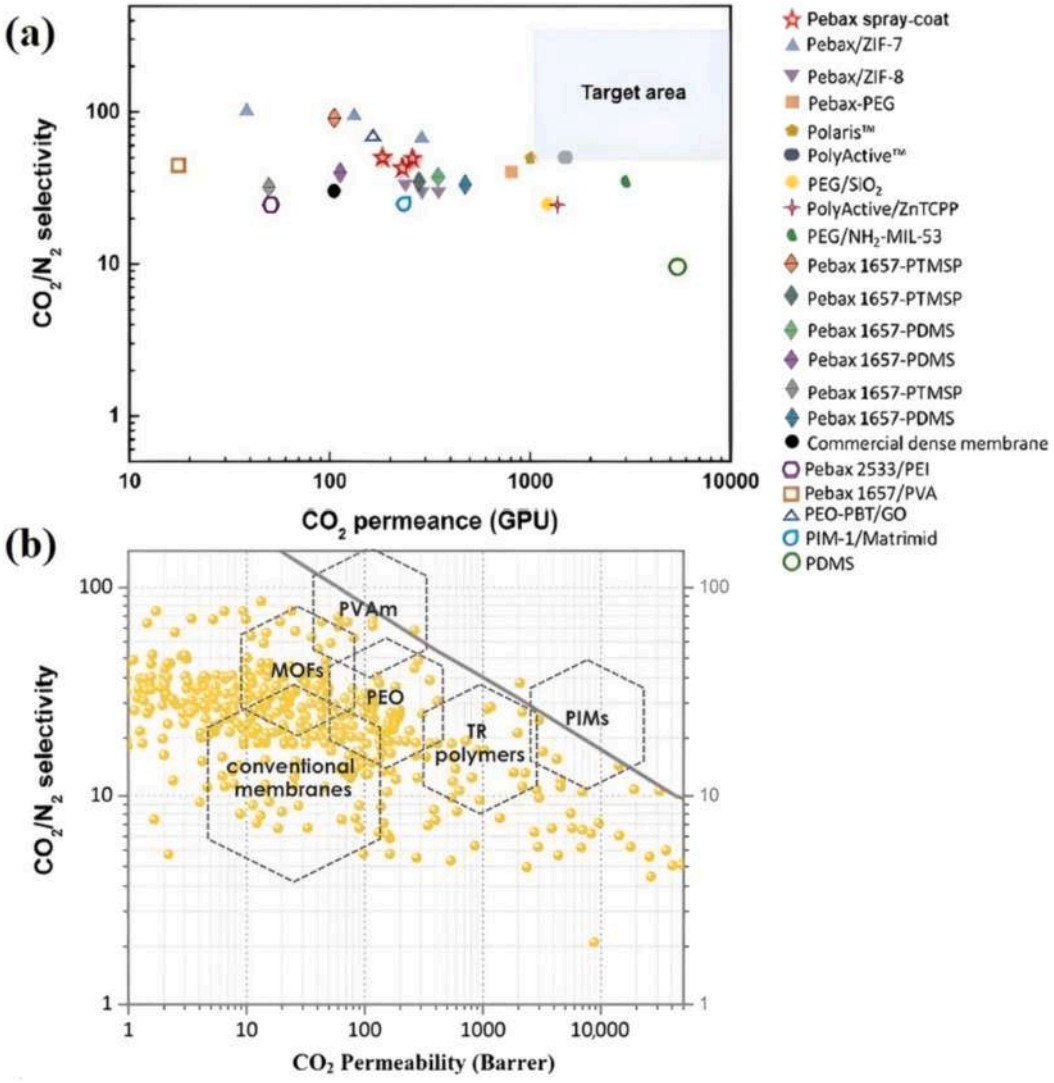


**Fig. 1.** (a) $CO_2/N_2$ separation performance of Pebax -based and -related polymeric membranes. Reproduced and modified with permission from Jiang et al. [7]. (b) Typical $CO_2/N_2$ gas separation performance of known polymeric membrane categories. Reproduced with permission from Tong and Sekizkardes [8].

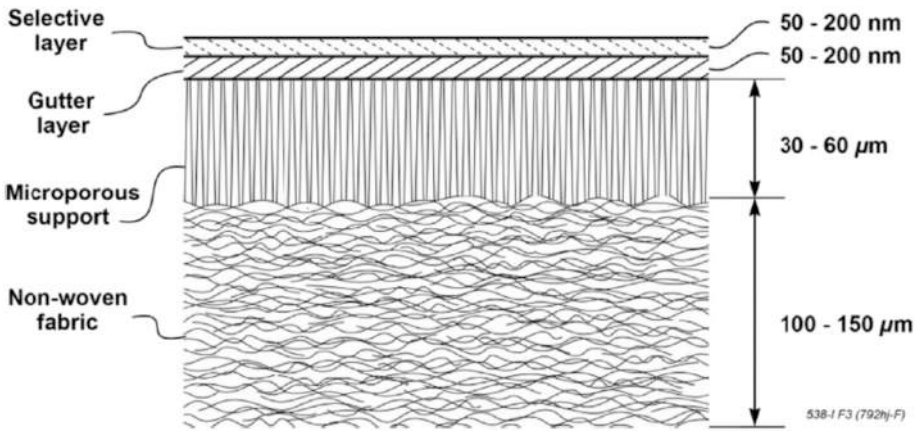


**Fig. 2.** Thin film composite membrane structure of Polaris™. Reproduced with permission from Lin et al. [11].

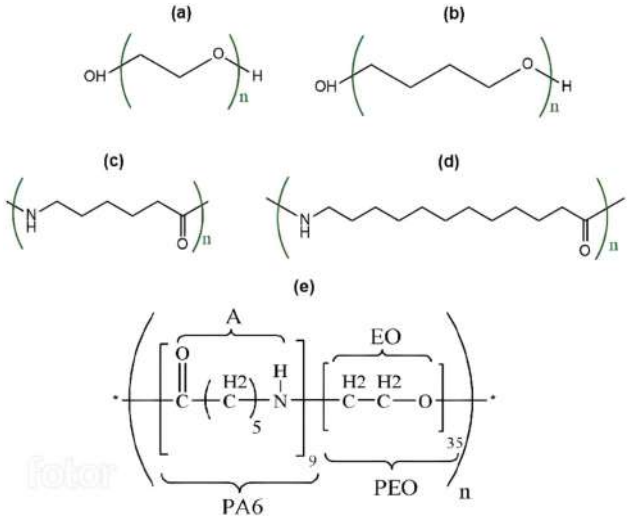


**Fig. 3.** (a) Poly(ethylene oxide) (PEO), also named as polyethylene glycol (PEG), or polyoxyethylene (POE); (b) poly(tetramethylene oxide) (PTMO), also named as polytetrahydrofuran (PTHF), or poly(tetramethylene ether) glycol (PTMEG); (c) Nylon 6 (PA6), also named as poly(ε-caprolactam) and (d) Nylon 12 (PA12) building blocks of different Pebax grades (Reproduced and modified with permission from Nematollahi et al. [15]); (e) Molecular structure of Pebax-1657. **A**: Amide repeating unit, **EO**: Ethylene oxide repeating unit, **PA6**: Polyamide nylon 6, **PEO**: Polyethylene oxide. Terminal groups can be amino and carboxyl groups due to the presence of polyamide blocks and hydroxyl groups (polar groups) in PEO.

**Table 1**
Pebax grades' structural building blocks and analogies. Reproduced and modified with permission from Embaye et al. [1].

| Grade | PE type | PA type | PE/PA (wt%) |
|---|---|---|---|
| 1041 | PTMO | PA12 | 75:25 |
| 1074 | PEO | PA12 | 55:45 |
| Renew®30R51† | PEO | PA11 | 81:19 |
| 2080* | PTMO | PA12 | 50:50 |
| 1657 | PEO | PA6 | 60:40 |
| 4011# | PEO | PA6 | 57:43 |
| 5513* | PTMO | PA6 | 60:40 |
| 2533 | PTMO | PA12 | 80:20 |
| 3533 | PTMO | PA12 | 70:30 |
| 4033 | PTMO | PA12 | 53:47 |
| 5533 | PTMO | PA12 | 38:62 |
| 6333 | PTMO | PA12 | 24:76 |
| 7033 | PTMO | PA12 | 25:75 |
| 7233 | PTMO | PA12 | 20:80 |

† from [16], * from [17], # from [18]

form rigid/sturdy PA6 crystals. Meanwhile, the soft PEO blocks can also exist in both phase types with crystallization predominantly occurring through polymer chain folding. In the Pebax-1657 structure PA6 crystals possess a high melting temperature of $T_m = 479$ K (histogram of Fig. 10 (b)) and, unlike PEO crystals ($T_m = 289$ K from histogram of Fig. 10(a)), do not melt under the typical operating conditions of the membrane for $CO_2/N_2$ gas separation, as applied for post-combustion capture at the stack (1 bar pressure and temperature $< 150$ °C). As explained in following sections, these PEO and PA6 crystal melting temperatures inside the *co*-polymer do not coincide with those of the respective pristine polymers.

### 2.2. PEO and PA6 crystal structures and size

Structurally, crystals form from hydrogen bonding between polymer chain-segments of same lengths, as they are arranged in parallel. PA segments form H-bonds between hydrogen and oxygen of amide groups, whereas PE segments between ether-oxygen and hydrogen of methylene or terminating hydroxyl groups. At temperatures below the crystallization temperature $T_c$, flexible, linear polymers, such as the Pebax-1657 blocks PEO and PA6, commonly undergo chain folding, resulting in the formation of chain-folded sheets that stack together into chain-folded lamellae crystallites with thin-platelet geometry (Fig. 5). These lamellar crystals can further self-arrange in various multi-crystal structures, depending mainly on crystallization rate. For instance, under rapid crystallization rate spherulites may form, characterized by radiating lamellae originating from a central point, whereas slow crystallization rates can lead to the formation of parallel-stack lamellae structures [20]. In particular, PEO crystals exhibit a lamellar structure composed of parallel polymer chains, which can either be distinct chains, or segments of the same chain folded one or more times. As shown in Fig. 6, the monoclinic crystal's elementary cell (EC) comprises four parallel chain segments that extend as four interconnected spirals. In this so-called 7/2 helical structure with a trans–gauche–trans conformation, two periods of the helix have seven EO (ethylene oxide) monomer units. Since the projection of each helix onto the monoclinic EC's c-axis for these two periods has a length of 1.948 nm, the projection length of one EO monomeric unit onto the c-axis is, $L_1 = 1.948/7 = 0.2783$ nm. Therefore, the total lamellar crystal thickness in the direction of c-axis is given by:

$$L_c = \frac{NL_1}{1+n} \quad (1)$$

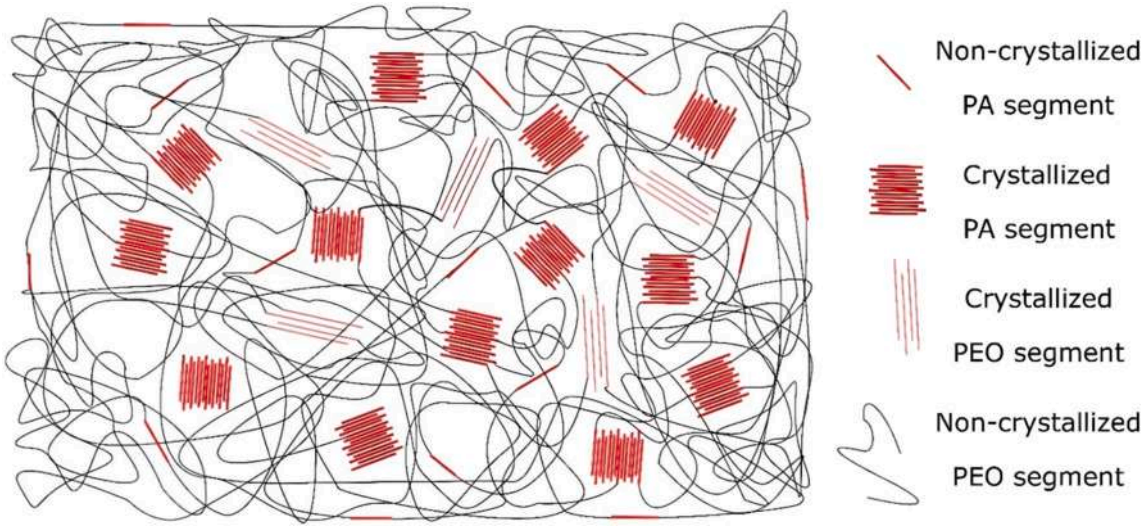


**Fig. 4.** Schematic representation of Pebax-1657 microstructure, at a temperature below the $T_m$ of PEO. Reproduced with permission from Didden et al. [19].

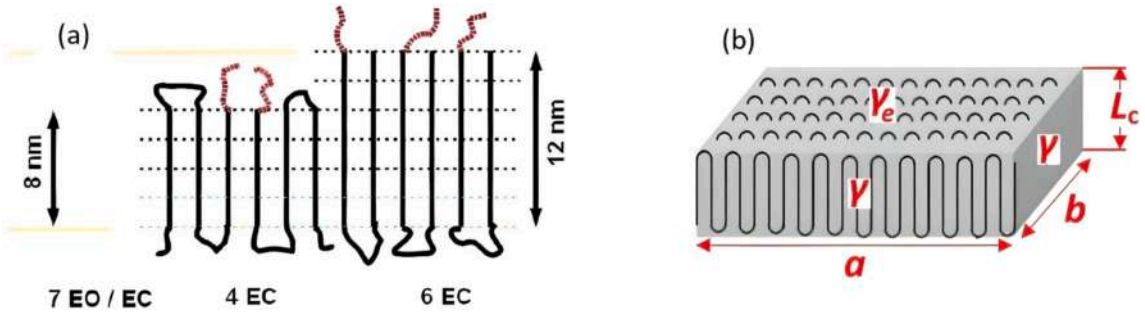


**Fig. 5.** (a) Schematic representation of chain-folded PEO lamellar crystallite's lateral surface (EC stands for "elementary cell" of the crystal, EO for "ethylene oxide" repeating unit of the polymer) reproduced from Braun and Meyer [22]; (b) same crystal in 3D ($\gamma_e$ or $\sigma_e$ is specific free surface energy at the end surface of the lamellar crystal, $\gamma$ or $\sigma$ is specific free surface energy at the lateral surface of the lamellar crystal), reproduced and modified with permission from Bai et al. [23]. The corresponding crystal growth model with primary and second stage nucleation at the lateral surface of the primary crystal is described in Hoffman et al. [24].

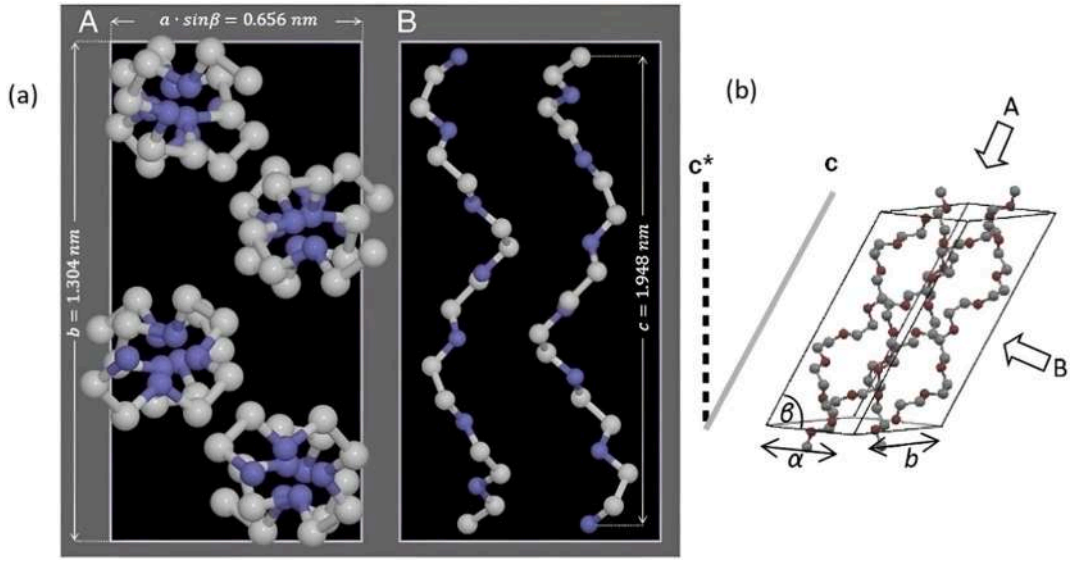


**Fig. 6.** Schematic description of lamellar monoclinic PEO crystal's elementary unit. (a) Top (A) and side (B) views reproduced and modified with permission from Kwon et al. [29]; (b) 3D view (unit cell inclination angle between α-axis and c-axis is $\beta = 54.6°$) reproduced with modifications from Braun and Meyer [22].

where $N$ represents the polymerization index (or degree of polymerization) and $n$ indicates the number of polymer chain folds within the crystal. For fully extended chains $n = 0$ and the lamellar thickness corresponds to the full length of the chain projected onto the c-axis [21]. Number of EC units per chain fold, and therefore also crystal thickness, has a statistical distribution in each crystal. For example, in Fig. 5(a) one crystal with thickness ranging from 4 ECs ($L_c = 4 \times 1.948 = 7.8$ nm) to 6 ECs ($L_c = 6 \times 1.948 = 11.7$ nm) is shown.

However, the following crystal length restriction sets in: typically, Pebax-1657 used in membrane preparation has a PEO-block size of around 1500 g/mol (given by Arkema), which corresponds to approximately 35 EO monomer units and a PA6-block size of around 1000 g/mol, i.e., 9 PA monomer units [25]. Based on the 0.2783 nm c-axis projection length of one EO monomer unit in 7/2 helical lamella crystals with trans–gauche–trans chain conformation, the longest possible PEO crystals correspond to the case where the whole lengths of two fully extended 35 monomer-unit PEO chains are arranged in parallel forming a bundle with entire crystal length, $L_c = 35 \times (1.95/7) = 9.75$ nm (Eq. 1), corresponding to the length of 5 monoclinic EC units. Regarding lowest possible crystal length along the c-axis, obviously no monoclinic crystal can be shorter than the 1.95 nm of one monoclinic EC. Finally, XRD patterns of pure PEO crystals typically exhibit two characteristic peaks at $2\theta = 19.3°$ and 23.6° (Cu target source with Kα radiation wavelength 0.154 nm), corresponding to reflections from the (120) and (010) planes, respectively [26–28].

Regarding PA6 crystals, according to literature [30–33], it also forms monoclinic crystals, but of two distinct main polymorph structures: of a metastable γ-phase exhibiting a twisted chain conformation, and/or of a thermodynamically stable α-phase displaying a planar zigzag chain conformation. The metastable γ-crystals can transform into α-crystals with a solid-crystal-crystal γ–α phase transition, initiated if temperature rises above 100 °C [34], while above 160 °C an α–α' phase transition takes place resulting in the formation of pseudohexagonal phase α' (Brill transition [35]). β-crystals can also form, but at usual cooling rates their formation is not favored. TTT diagrams can be found in the work of Seguela [36], showing that by increasing cooling rate polymorphs are favored in the order: α-, γ-, β-, amorphous. In particular, as shown in Fig. 7(a) & 7(b), both main crystal forms have inter-chain N—H···O═C hydrogen bonding between neighboring PA segments in one crystal axis direction (a-axis direction for α-PA6 & c-axis direction for γ-PA6) and van der Waals bonding in one other axis direction (c-axis direction for α-PA6 & a-axis direction for γ-PA6). As presented in Fig. 7(c), in the case

**Table 2**
Monoclinic elementary cell dimensions of a-PA6 crystal and XRD peak angles and d-spacings of its diffraction planes.

| Miller indices | | | d-spacing | 2θ |
|---|---|---|---|---|
| h | k | l | (nm) | (degrees) |
| 2 | 0 | 2 | 0.359 | 25 |
| 0 | 2 | 0 | 0.862 | 10.3 |
| 0 | 0 | 2 | 0.370 | 24 |
| 2 | 0 | 0 | 0.442 | 20 |
| **EC** | **a (nm)** | **b (nm)** | **c (nm)** | **β (degrees)** |
| monoclinic | 0.956 | 1.724 | 0.801 | 67.5 |

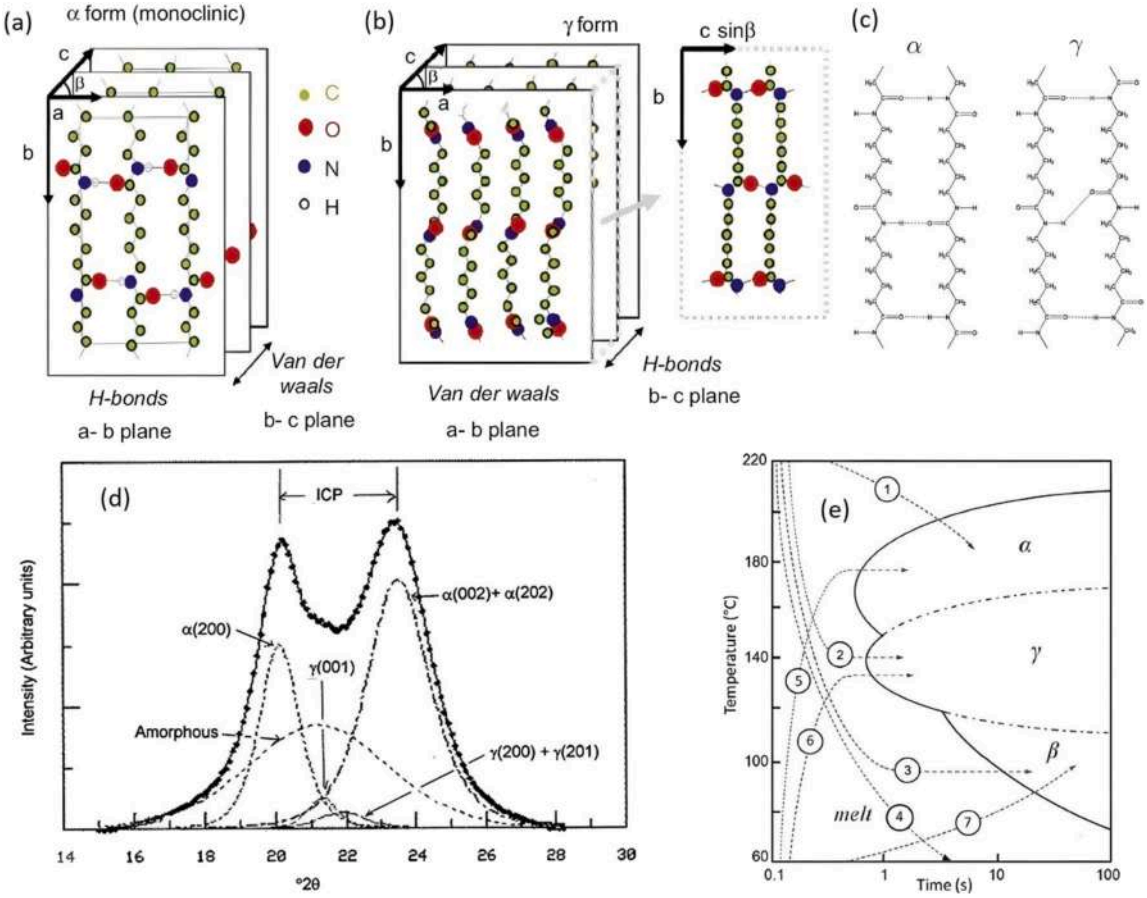


**Fig. 7.** Polymorph structures of PA6 crystals: (a) Main stable α-form and (b) metastable γ-form; (c) inter-chain hydrogen bonding in α- and γ- forms; (d) corresponding XRD peaks; (e) TTT (Time-Temperature-Transformation) diagrams of PA6 for different cooling rates (1 to 4) and heating rates (5 to 7). (a) & (b) reproduced and modified with permission from Millot [47]; (c) reproduced and modified from Parodi et al. [46]; (d) reproduced and modified with permission from Correale and Murthy [48]; (e) reproduced with permission from Seguela [36].

**Table 3**
Monoclinic elementary cell dimensions of a γ-PA6 crystal and XRD peak angles and d-spacings of its diffraction planes.

| Miller indices | | | d-spacing | 2θ |
|---|---|---|---|---|
| h | k | l | (nm) | (degrees) |
| 0 | 0 | 1 | 0.410 | 21.5 |
| 2 | 0 | 2 | 0.239 | 38.5 |
| 0 | 0 | 2 | 0.205 | 45 |
| 2 | 0 | 1 | 0.411 | 21.6 |
| 2 | 0 | 0 | 0.400 | 22 |
| **EC** | **a (nm)** | **b (nm)** | **c (nm)** | **β (degrees)** |
| monoclinic | 0.933 | 1.688 | 0.478 | 59 |

of α-form the hydrogen bonds connect two chains, which are arranged in anti-parallel directions (N → C & C → N) along b-axis, while in the case of γ-form the two chains are in parallel directions (both N → C) along b-axis. Typical monoclinic unit cell dimensions and XRD peak positions with corresponding crystal planes are given in Table 2 for α-crystals [37] and in Table 3 for γ-crystals [38,39], while further crystal polymorphs and variations of unit cells are given by Miller [40] and by Li & Goddard [41]. In Tables 3 & 4 the d-spacings were calculated from Eq. 2 [42,43] based on crystal dimensions given by Holmes et al. [44].

$$\frac{1}{d^2}=\frac{1}{sin^2\beta}\left(\frac{h^2}{a^2}+\frac{k^2\cdot sin^2\beta}{b^2}+\frac{l^2}{c^2}-\frac{2hl\cdot cos\beta}{ac}\right) \quad (2)$$

Respective XRD spectra are illustrated in Fig. 7(d), based on Cu-target source with Kα radiation wavelength 0.154 nm. The γ-PA6 XRD peak at 21.7° might broaden due to the superposition with a reflection from the metastable β-phase if it is present [36,45]. Moreover, for the α-crystal polymorph an increase in index of crystalline perfection (ICP) corresponds to a decrease in the unit cell dimensions, i.e., mainly the spacing between the planes of hydrogen bonded chains. Finally, it should be noted that, in presence of humidity both α-PA6 and γ-PA6 crystals absorb water molecules, thereby weakening inter-chain bonds inside the crystals, which results in a drop of glass transition temperature $T_g$. According to Parodi et al. [46], in an environment of 80 % relative humidity at 23 °C the absorbed water fraction in the crystal is approx. 5 wt%. and the $T_g$ drops to the level of 10 °C vs. 70 °C for dry conditions. This can have a significant impact on $CO_2$ permeability of Pebax membranes, as discussed in section 3.2 "Humidity influence on gas separation performance of Pebax-1657".

Regarding crystal length of PA6 in Pebax-1657, literature data are mainly based on DSC and rarely on XRD, because peak superposition reduces the accuracy of size derivation from Debye-Scherrer method. This becomes very clear in one particular case, the work of Ghadimi et al. [49], who used both methods on the same sample. In specific, they found a sharp XRD peak at 2θ = 30.44° for pristine Pebax-1657 films employing a Fe-target source with Kα radiation wavelength 0.194 nm. Converting this to the corresponding 2θ value for a Cu-target source with Kα radiation wavelength 0.154 nm, it yields 24.06° (derived from Bragg's law), which is characteristic of PA6 crystal α-polymorph's (002) plane reflection. Ghadimi et al. calculated an average crystal length of 8.25 nm, applying the Debye-Scherrer method (FWHM = 1.31) for this peak of α-PA6 crystals. However, the 8.25 nm is almost half the value of the 15.5 nm obtained from calculations based on the Hoffman-Weeks Eq. 3 [50] (derived from Gibbs-Thomson Eq. 4, as described in the next section 2.2.1 "Crystal melting temperatures"), using experimental data from DSC diagrams, including $T_m$ = 478 K and $T_c$ = 422 K values, provided by the same authors, along with other equation parameters, namely $T_m^b$ = 506 K and $\beta$ = 1.5 from $T_m$ vs. $T_c$ slope (see Fig. 11).

$$T_m=\frac{T_c}{2\beta}+T_m^b\left(1-\frac{1}{2\beta}\right) \quad (3)$$

$T_c$ is the crystallization temperature (a function of melt cooling rate), $L_c$ the average lamella thickness at the crystal step (lateral surface of primary crystal) where secondary growth (thickening) occurs and $\beta=\frac{L_c}{L_c^*}$ is the crystal thickening factor [51], where $L_c^*$ ($=\frac{4\gamma_e}{\Delta f}$, where $\Delta f$ represents the free energy difference between the supercooled liquid phase and the bulk crystal phase) is the primary crystal's thickness, i.e., the lamella thickness for which crystal growth in the other two crystal expansion directions a & b is favored the most and has the maximum rate and $T_m^b$ is the melting temperature of the equilibrium bulk-crystal (of infinite size). The main assumptions for validity of equation (Eq. 3) are that no recrystallization and crystal rearrangement phenomena take place.

In the work of Ghadimi et al. the significantly lower crystal size value calculated from XRD is attributed to the fact that the (002) plane's peak at 24° and the (202) plane's peak at 25° merge into a single wide (002) + (202) peak, as shown in the deconvoluted diagram of Fig. 7(d), resulting in a much higher FWHM value than what would be observed based on the single (002) peak. Note that the value of 15.5 nm from DSC corresponds to the c-axis direction (Fig. 7(a)), while polymer chains stretch in the b-axis direction, where the unfolded a-PA6 crystal can reach a maximum thickness of (9/2) × 1.724 = 7.76 nm, since one Pebax-1657 PA6-block contains 9 PA monomer units, as described in the beginning of this section.

### 2.2.1. *Crystal melting temperatures*

During crystal growth the total free energy drops, which implies that the crystal becomes more stable and its melting temperature $T_m$ rises, tending toward the equilibrium bulk-crystal melting temperature $T_m^b$. $T_m$ depends strongly on crystal size for most linear polymers and in the case of block *co*-polymers crystal size can be influenced by interaction between different blocks. For example, as shown by Pfefferkorn et al., for PEO crystals in the diblock co-polymer PEO-*b*-PMA with 113 PEO EC units (max. $L_c$ = 31.5 nm) [52], the reduction in PEO crystal size, in terms of lamellar crystal size $L_c$, can be effectively induced by increasing PMA content in the co-polymer. According to the authors, the more PMA, the less space for PEO lamella to fully extend, which results in crystal length reduction by shrinking through shorter chain-folding. The resultant shift in $T_m$ toward lower temperatures was reported to be approximately 18 degrees when the PMA content increased from 0 to 73.8 wt% and $L_c$ of PEO crystals was calculated to be 5 nm for the diblock *co*-polymer with 73.8 wt% PMA. The basic theoretical correlation between polymer crystal melting temperature and crystal size is referred to as Gibbs-Thomson Eq. 4 and is given below [53,54].

$$T_m\Big/T_m^b=1-\frac{2(\gamma_{SV})_c V}{L_c\Delta h} \quad (4)$$

$T_m$ is the melting temperature of the crystal in the sample, i.e., in contact with the amorphous phase, $T_m^b$ the theoretical melting temperature of the bulk (infinitely thick) crystal, $(\gamma_{SV})_c$ the specific Gibbs free energy of the crystal(solid)-vapor phase boundary, i.e., the surface energy of the crystal (the actual crystal, not the bulk crystal), $L_c$ the thickness (average) of the lamella crystal, $V$ the molar volume of the crystal and $\Delta h$ the specific enthalpy of fusion of the crystal.

In accordance with Eq. 4, a larger crystal has a higher melting temperature. Conversely, a higher bulk crystal surface energy $\gamma_{SV}$ indicates that more energy is needed for crystal growth, or equivalently, that the crystal can melt more easily, which corresponds to a lower $T_m$. For example, in the work of Pfefferkorn et al. [52], surface energy $\gamma_{SV}$ of PEO crystals inside the co-polymer was also found (calculated from Eq. 4 with $T_m$ measured from DSC and $L_c$ from SAXS according to Strobl & Schneider [55]) to increase slightly with PMA content, from 0.0235 N/m up to a maximum value of 0.0322 N/m, thereby intensifying the drop in $T_m$ according to Eq. 4.

In order to calculate crystal size from DSC-derived $T_m$ values, all Eq. 4 parameter values must be known. For the case of Pebax-1657, all these values are either directly known, or derived through calculations as described in the following. In particular, values of $(\gamma_{SV})_a$ of the

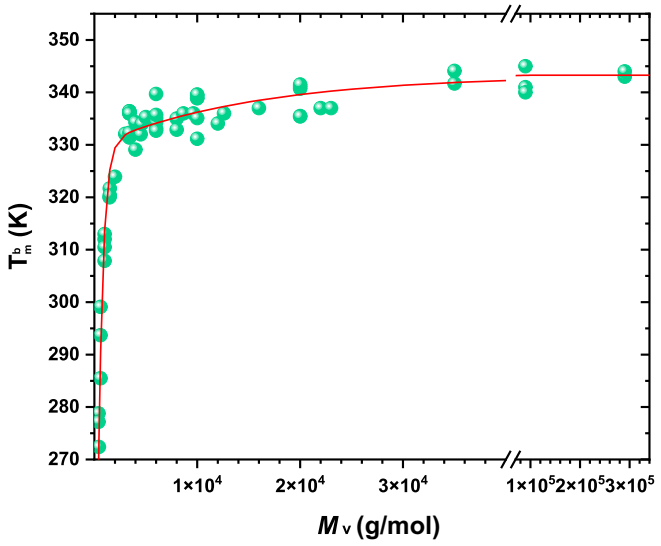


**Fig. 8.** Literature data (from Table S2) of PEO bulk crystal melting point $T_m^b$ vs. PEO viscometric average molecular weight $M_v$ (g/mol). Red line: Fitting curve of Eq. 6 ($R^2$ = 97.5 %).

amorphous polymer surface for PEO and PA6 are given by Souheng Wu [56]. The values are 38 and 42 mN/m, respectively. Then, $(\gamma_{SV})_c$ of the polymer crystallite surface can be calculated based on $(\gamma_{SV})_a$ of the respective amorphous polymer with the following Eq. 5, suggested by Schonhorn [57]:

$$(\gamma_{SV})_c = \left(\frac{\rho_c}{\rho_a}\right)^4 (\gamma_{SV})_a \quad (5)$$

$\rho_a$ and $\rho_c$ are the densities of the amorphous and crystalline phases of the polymer, with values 1.13 and 1.229 g/cm$^3$ for PEO and 1.09 and 1.232 g/cm$^3$ for PA6, respectively, according to R.L. Miller [58]. Consequently, as emerges from Eq. 5, $(\gamma_{SV})_c$ is 53.17 mN/m for PEO and 68.55 mN/m for α-PA6 crystallites. Furthermore, literature values for heats of fusion $\Delta h$ are 245.29 J/g for crystallites of PA-12 (MW 197.32 g/mol), 229.76 J/g for PA-6 (MW 113.16 g/mol) [59], 173.34, or 202.31 [60], or 196.6 [61], or 167–267 J/g (7.33–11.7 kJ/mol) [58] for PEO (MW 44.05 g/mol) and 171.9–199.67 J/g (12.4–14.4 kJ/mol) for PTMO (MW 72.12 g/mol). Melting temperatures of bulk crystals $T_m^b$ are in the ranges 335–349 K for PEO and 308–333 K for PA6, depending on the polymer's average molecular weight, expressed as $M_v$ (viscometric) or $M_n$ (average number) or $M_w$ (average weight), according to numerous experimental data from literature that are provided in Figs. 9 & 10 and Tables S1 & S2 (Supplementary), respectively. Specifically, in the case of PEO bulk crystal the $T_m^b$ dependence on molecular weight is strong, particularly for lower molecular weights, and the experimental literature data of Fig. 8 and Table S2 have been fitted by the following empirical Eq. 6, with all parameters of the equation provided in Table 4. On the contrary, based on the significantly scarcer data of corresponding data for PA6, as depicted in the diagram of Fig. 9, there is no significant influence of molecular weight on $T_m^b$ for neither of α- and γ- forms. As shown in the corresponding Table S3, α- & γ- PA6 bulk crystal melting points $T_m^b$ for PA6 have relatively constant values (493–503 K and 485–491 K, respectively) within an average number molecular weight $M_v$ range of 6000–35,000 g/mol. Finally, measured literature $T_m$ values of PEO and PA6 crystals inside Pebax-1657 are listed in Tables S3 and S4, respectively. These values are also presented as histograms in Fig. 10 (a) & 10(b), in order to give an overview of statistical variance of these experimental data.

$$T_m^b = A + B_1 \times e^{-\frac{(M_v - M_{v,0})}{C_1}} + B_2 \times e^{-\frac{(M_v - M_{v,0})}{C_2}} \quad (6)$$

**Table 4**
Values of the parameters in Eq. 6.

| Parameter | Value |
|---|---|
| $A$ | 343.284 |
| $M_{v,0}$ | −3696.11875 |
| $B_1$ | −398,728.10239 |
| $C_1$ | 466.46463 |
| $B_2$ | −17.16237 |
| $C_2$ | 15,416.19025 |
| Adj. R-Square | 0.97489 |

Finally, the more convenient, in terms of calculating crystal size from DSC, Hoffman-Weeks equation (Eq. 3) is derived from the aforementioned Gibbs-Thomson equation as described in the early publication of Hoffman & Weeks [50] and other more recent works [51,52]. It must be underlined, that the term "crystal thickness" (basic parameter in Eq. 3) refers to the average lamella thickness $L_c$, considering that the number of EC units per chain fold exhibits a statistical distribution within each crystal (see Fig. 5(a)). Consequently, the average crystal thickness of the primary crystal $L_c^*$ can be either larger or smaller than the $L_c$ of the secondary crystal, which is formed after secondary growth at the lateral surfaces of the primary crystal through thickening, allowing $\beta$ to assume any value between the theoretical minimum 0.5 for thickness $\frac{2\gamma_e}{\Delta f}$ and the experimental maximum of about 2 [62].

According to Eq. 3, the relationship $T_m$ vs. $T_c$ is linear as presented in Fig. 11, assuming that $\beta$ remains constant. According to the work of Rahman et al. [63], the crystallization temperature $T_c$ of PEO crystals within Pebax-1657 was estimated to be 254 K based on the peak observed in the cooling trace of DSC measurements. Similarly, in the same work, the crystallization temperature of PA6 crystals in Pebax-1657 was estimated to be 439 K.

### 2.2.2. Crystallinity

Crystallinity $X_c$ is considered a fundamental material parameter which is often given considerable attention the relevant literature. Among the two methods that are usually implemented for crystallinity measurements, namely DSC and XRD, only the former is expected to provide precise data. In XRD diffraction patterns, the area under the broad peak, corresponding to the "amorphous" polymer phase, is in most cases very small, thus introducing a significant margin of error, while the superposition or overlap of multiple peaks of the crystalline

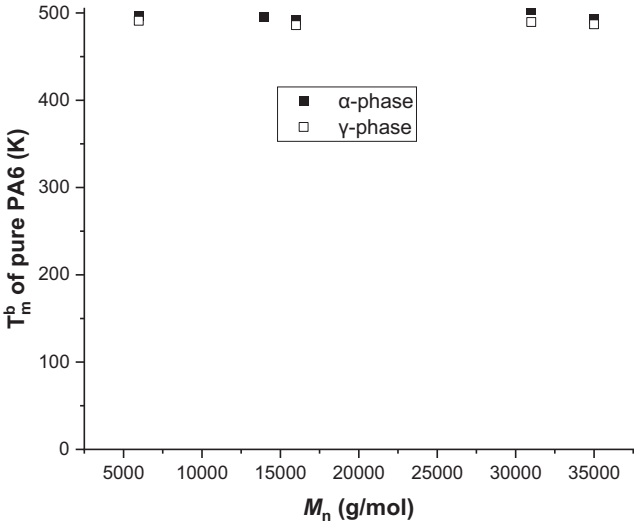


**Fig. 9.** Literature data (from Table S3) of pure PA6 bulk crystal melting point $T_m^b$ vs. number average molecular weight $M_n$. Filled squares: α-phase values, open squares: γ-phase values.

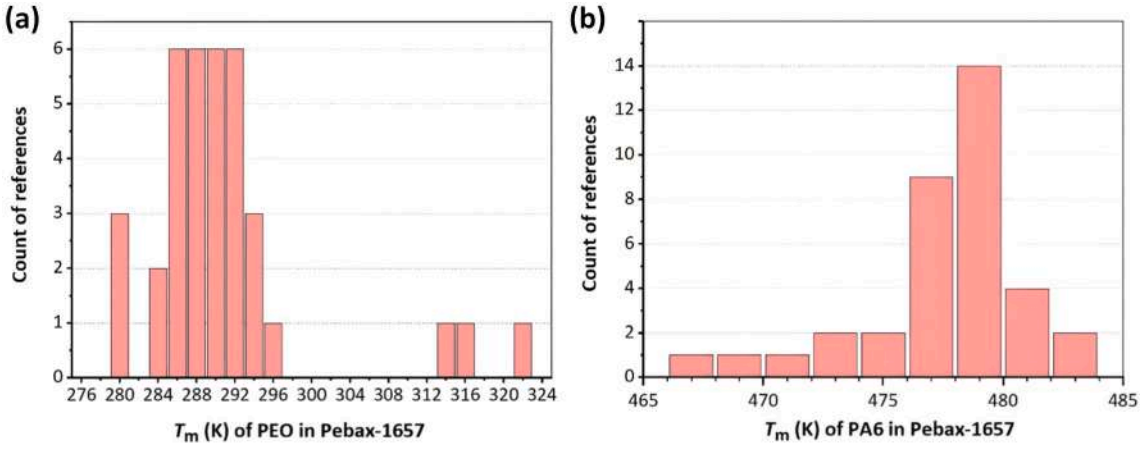


**Fig. 10.** Histogram presenting the number of literature references for each $T_m$ value. (a) $T_m$ is the melting point of PEO crystals in Pebax-1657, based on DSC measurements (data from Table S4); (b) $T_m$ is the melting point of PA6 crystals in Pebax-1657, based on DSC measurements (data from Table S5).

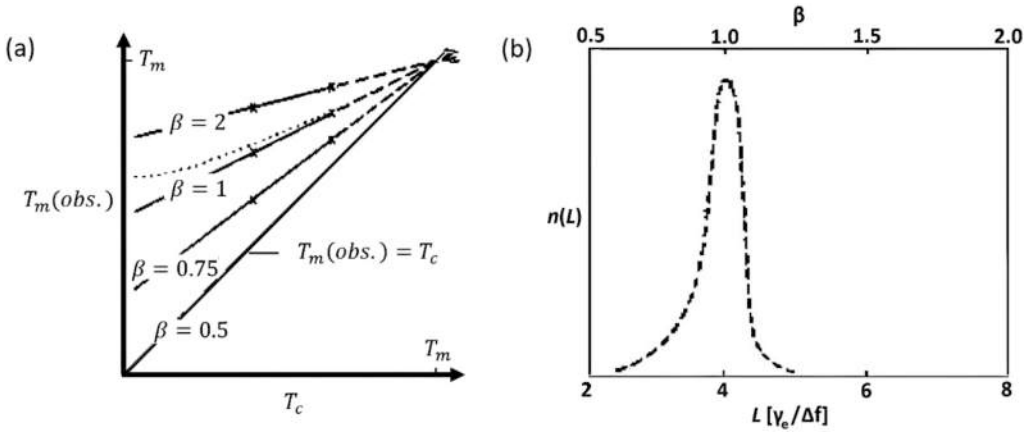


**Fig. 11.** (a) $T_m$ (observed) vs. $T_c$ for various $\beta$ parameter values (solid lines). Dotted line is an experimentally (DSC) measured line, which corresponds to the dashed line of chain-folded lamellar crystal thickness distribution (b) (reproduced and modified with permission from Hoffman & Weeks [50]).

phases presents an additional challenge. On the other hand, in the case of DSC, a careful consideration of the definition of $X_c$ has to be taken into account when comparing data with existing literature. In particular, two distinct definitions of $X_c$ from DSC are encountered:

$X_c$ defined as PA-crystal percent of total Pebax mass, resulting in equation $X_c = \frac{\Delta h}{\Delta h^{\varnothing}}$, or

1) $X_c$ defined as PA-crystal percent of total PA-block mass (note that for Pebax-1657 40 % of total mass is PA6), resulting in equation $X_c = \frac{\Delta h}{0.4 \cdot \Delta h^{\varnothing}}$,

where $\Delta h$ and $\Delta h^{\varnothing}$ are the specific enthalpies of crystal melting from DSC PA-peak area (per gram of Pebax sample) and from theory (per gram of PA-crystal), respectively.

In this review, for comparison reasons, all PA-crystallinity values mentioned in literature have been converted, in order to adjust to the first definition of $X_c$, i.e., as a percentage of PA-crystals relative to the total Pebax mass. Furthermore, in order to determine the $T_m$ values of both PEO and PA blocks, DSC measurements are usually performed by starting the scan from a significantly low temperature, far below ambient conditions. Therefore, it appears that the membrane also possesses PEO-block crystallinity, which might be misleading, since membranes are usually evaluated at, or above, ambient temperatures, surpassing the crystal melting temperature $T_m$ of PEO.

### 2.3. Fractional free volume

Fractional free volume (*FFV*) represents the volume percentage of the material unoccupied by polymer chains. It is defined by Eq. 7:

$$FFV = \frac{V - V_o}{V} \tag{7}$$

where $V$ is the molar volume of the polymer (molecular weight of repeat unit divided by density $\rho_r$) and $V_o$ is the volume occupied by the molecules that can be estimated using Bondi group contribution method, i.e., from the van der Waals volumes $V_w$ of the various groups in the polymer structure, according to Eq. 8 [64].

$$V_o = 1.3 \cdot V_w \tag{8}$$

According to Zhao et al. [65], the van der Waals volume $V_w$ (in $\mathring{A}^3$) of one repeat unit is given by the following Eq. 9:

**Table 5**
Van der Waals volumes of atoms. Reproduced and modified with permission from Zhao et al. [65].

| Atom | $V_W$ (Å$^3$) | Atom | $V_W$ (Å$^3$) |
|---|---|---|---|
| H | 7.24 | P | 24.43 |
| C | 20.58 | S | 24.43 |
| N | 15.60 | As | 26.52 |
| O | 14.71 | B | 40.48 |
| F | 13.31 | Si | 38.79 |
| Cl | 22.45 | Se | 28.73 |
| Br | 26.52 | Te | 36.62 |
| I | 32.52 | | |

$$V_{W repeat\ unit} = \sum (V_W)_{all\ atom\ contributions} - 5.92 \cdot N_B \quad (9)$$

where $N_B$ is the number of bonds between atoms in one repeat unit.

For example, in one EO repeating unit (molecular weight 44.05 g/mol) $N_B$ is 7 and if $V_{W,EO}$ is in cm$^3$/g, then based on values for each atom given in Table 5:

$$V_{W,EO} = [(2 \cdot 20.58) + (4 \cdot 7.24) + (1 \cdot 14.71) - (5.92 \cdot 7)] \cdot (10^{-24}) \cdot (6.023 \times 10^{23}) / 44.05$$

Similarly, for caprolactone (A6) amide repeating unit (molecular weight 113 g/mol) $N_B$ is 21 and:

$$V_{W,A6} = [(6 \cdot 20.58) + (11 \cdot 7.24) + (1 \cdot 14.71) + (1 \cdot 15.6) - (5.92 \cdot 21)] \cdot (10^{-24}) \cdot (6.023 \times 10^{23}) / 113$$

where $\mathring{A}^3$ have been converted to cm$^3$ unit by multiplying with $10^{-24}$.

The resulting calculated van der Waals volume values of each Pebax-1657 polymer block are presented in Table 6.

Finally, the total van der Waals volume of a pristine Pebax-1657 membrane is calculated from Eq. 10, where $X_{c/PEO}$ and $X_{c/PA6}$ represent the crystallinities of PEO and PA6 as fractions of the total Pebax-1657 membrane mass:

$$\sum (V_W)_{all\ groups} = X_{c/PEO} \cdot (V_W)_{c/PEO} + X_{c/PA6} \cdot (V_W)_{c/PA6} + (0.6 - X_{c/PEO}) \cdot (V_W)_{a/PEO} + (0.4 - X_{c/PA6}) \cdot (V_W)_{a/PA6} \quad (10)$$

If PA6 crystallinity value is 11 %, based on the average of literature data presented in Tables 13 & 14 (section 3.7 "Literature data on $CO_2$/$CH_4$ and $CO_2$/$N_2$ separations with pristine Pebax-1657"), and assuming that PEO crystallinity is zero ($T_c$ of PEO is below 298 K room temperature), then the resulting total van der Waals volume for Pebax-1657 is 0.589 cm$^3$/g and the corresponding $V_o$ from Eq. 8 is 0.766 cm$^3$/g. Using the same calculation method (Eq. 10), with densities of Table 6, instead of van der Waals volumes, the resulting total density is 1.13 g/cm$^3$, which can be inverted to give a specific volume $V$ = 0.885 cm$^3$/g. Therefore, based on Eq. 7, the calculated *FFV* turns out to be 0.134, which is in relative agreement with the literature data given in Table 7. It should be noted that misleading FFV values below 0.1 found in literature are usually attributed to $V_W$ calculations based on wrong molecular structures, while abnormally high values above 0.3 are also reported.

Finally, apart from its correlation with density, the high importance of a polymer's FFV is that it is also directly related to diffusion coefficients according to the Cohen-Turnbull model of Eq. 11 [76]:

$$D = \frac{\alpha \cdot u}{6} exp(-\gamma v / FFV) \quad (11)$$

**Table 6**
*FFV* calculation parameters for the different phases present in a Pebax-1657 membrane.

| Phase | $\rho_r$ (g/cm$^3$) [58] | $V_W$ (cm$^3$/mol*) [66] | $V_W$ (cm$^3$/g**) |
|---|---|---|---|
| PEO / amorphous | 1.13 | 24.2 | 0.593 |
| PEO / crystalline | 1.28 | 24.2 | 0.593 |
| PA6 / amorphous | 1.084 | 64.2 | 0.5816 |
| PA6 / crystalline | 1.23 | 64.2 | 0.5816 |

* per mol of one repeating unit.
** per gram of one repeating unit.

**Table 7**
Fractional free volume, density and van der Waals volumes of pristine Pebax-1657 membranes.

| *FFV* | $\rho$ (g/cm$^3$) | $V_W$ (cm$^3$/g) | Ref. |
|---|---|---|---|
| 0.125 from PALS analysis (3 wt% Pebax sol.) | – | – | [67] |
| 0.099† (5 wt% Pebax sol.) | 1.203 | 0.546† | [68] |
| 0.374 (no data) | 1.076 | – | [69] |
| 0.166 (3 wt% Pebax sol.) | – | – | [70] |
| 0.154 (3 wt% Pebax sol.) | 1.13 | – | [71] |
| 0.026† (4 wt% Pebax sol.) | 1.157 | 0.6475† | [72] |
| 0.148 from MD calculations (4 wt% Pebax sol.) | 1.14 | – | [73] |
| 0.134–0.121 (2.5 wt% Pebax sol.) | 1.129–1.146 | 0.59 | [30] |
| 0.67 (8 wt% Pebax sol.) | 1.14 | – | [74] |
| 0.126 (5 wt% Pebax sol.) | 1.14 | 0.59 | [75] |

† Questionable values, because calculations were based on an incorrect molecular structure.

**Table 8**
Diffusivity and Cohen-Turnbull model parameters in pristine Pebax-1657 membranes.

| $D$ | From 1.2 × 10$^{-6}$ to 2.6 × 10$^{-6}$ cm$^2$ s$^{-1}$ for $CO_2$ [31] |
|---|---|
| $\alpha$ | Gas-specific value |
| $u$ | Gas-specific value |
| $\gamma$ | 0.5–1 |
| $v$ | Gas-polymer-specific value |
| *FFV* | 0.134 |

where $D$ is the diffusion coefficient of the gas in the polymer, 1/6 is a typical value of geometric factor $g$, $\alpha$ is the molecular diameter, $u$ the kinetic velocity of the gas, $\gamma$ is an overlap factor which should lie between 0.5 and 1, $v$ a critical volume of void in the polymer just large enough to permit a diffusing molecule to jump in. In the case of Pebax-1657, the usual values of this equation's parameters are given in Table 8.

## 3. Gas separation performance of Pebax-1657

### 3.1. Pebax-1657 vs. other grades

Owing to the higher density of hydrogen bond -forming oxygen atoms in PEO vs. PTMO, the former has a higher density (1.21 g/cm$^3$ vs. 0.98 g/cm$^3$) and, for the same reason, PA6 has also a higher density than PA12 (1.14 g/cm$^3$ vs. 1.01 g/cm$^3$). Consequently, the 1657 grade, which combines the two building blocks with the highest density, has the highest density of all grades with at least one different building block. Fractional free volume (*FFV*) and density are inversely related and higher *FFV* results in higher diffusivity $D$ according to Eq. 11. Since $D$ is analogous to permeability (*Pe*) for most gases, it follows that among all grades, Pebax-1657 has the lowest permeability for most gases. This rule is partly counterbalanced in the case of $CO_2$, where the higher $CO_2$-solubility ($S_{CO_2}$) compared to other grades (Henry's constant at 25 °C is approximately 1.9 cm$^3$/cm$^3$•atm for Pebax-1657 [77] vs. 1.25 cm$^3$/cm$^3$•atm for Pebax-1074 [78] and 1.06 cm$^3$/cm$^3$•atm for Pebax-2533 [79]) gives Pebax-1657 the advantage of highest $CO_2$-philic selectivity among all grades, a property particularly pronounced in the case of $CO_2/N_2$ and to a lesser extent for $CO_2/CH_4$, as shown in Table 9. The importance of polar group content (which is highest for Pebax-1657) on solubility-selectivity is comparatively presented in Fig. 12 for different Pebax grades. Consequently, Pebax-1657 is the grade that is most commonly selected for use in post-combustion carbon capture applications. Typical Robeson plots comparing experimental data of different Pebax types are given in the review of Embaye et al. [1]. However, not all grades have been tested yet with respect to $CO_2$-capture applications. For example, Grade 5513 is the only grade, other than 1657, that can reportedly be dissolved in ethanol/$H_2O$ (70:30 *w*/w) solvent (Table S1, in Supplementary) and that has a selectivity of approximately 7.5 for $C_3H_6/C_3H_8$ gas separation [80], a better performance than the reported 2.9 [81] of 1657 for the same mixture. Yet this grade has not been tested for most $CO_2$-based gas separations.

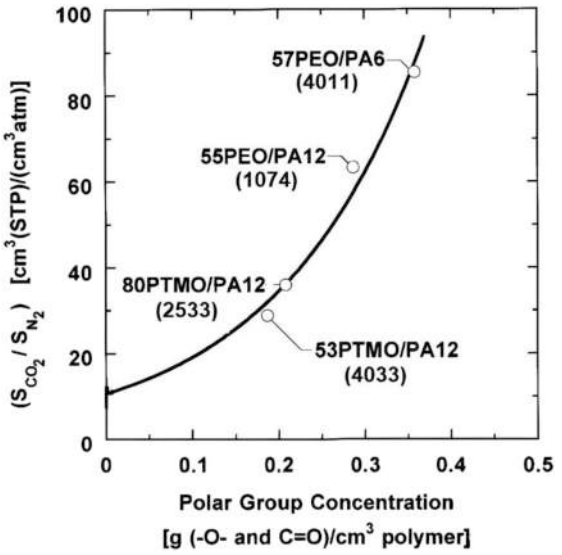


**Fig. 12.** Solubility selectivity of different Pebax grades vs. polar group concentration of the grade. Reproduced and modified with permission from Bondar et al. [95].

**Table 9**
Typical properties and gas separation performances of Pebax grades (reproduced with modifications from Embaye et al. [1]).

| Grade | PE type | PA type | PE/PA (wt%) | $X_c$ of PA (%) | Density (g·cm$^{-3}$) | PA melting point (°C) | Permeability | Selectivity | | References |
|---|---|---|---|---|---|---|---|---|---|---|
| | | | | | | | $CO_2$ (Barrer) | $CO_2/CH_4$ | $CO_2/N_2$ | |
| 1041 | PTMO | PA12 | 75:25 | | 1.04 | 170 | 39.7 | 11 | | [82] |
| | | | | | | | 24.6 | | 22.6 | [83] |
| 1074 | PEO | PA12 | 55:45 | 40† | 1.09 | 158 | 122 | 12 | | [82] |
| | | | | | | | 591 | 24.4 | | [84] |
| | | | | | | | 125 | | 15 | [85] |
| | | | | | | | 120 | | 51.4 | [18] |
| | | | | | | | 168 | | 55 | [86] |
| | | | | | | | 98.2 | 13.5 | | [87] |
| 1657 | PEO | PA6 | 60:40 | 11.5§ | 1.14 | 204 | 60‡ | 19‡ | 55‡ | – |
| 2533 | PTMO | PA12 | 80:20 | 14† | 1.01 | 134 | 171 | | 15.5 | [88] |
| | | | | | | | 386.3 | | 23.5 | [89] |
| | | | | | | | | 12 | | [90] |
| 3533 | PTMO | PA12 | 70:30 | | 1.01 | 144 | 243 | 5.7 | | [82] |
| | | | | | | | 127 | | 21.4 | [91]* |
| 4033 | PTMO | PA12 | 53:47 | 32† | 1.01 | 160 | 84.4 | 6.5 | | [82] |
| | | | | | | | 113 | | 20.4 | [18] |
| 4011 | PEO | PA6 | 57:43 | | | 201 | | | | |
| | | | | 20.4 | 1.14 | | 66 | | 56.4 | [18] |
| 5533 | PTMO | PA12 | 38:62 | 30† | 1.01 | 159 | | | 9.2 | [92]^^ |
| 6333 | PTMO | PA12 | 24:76 | | 1.01 | 169 | 7.4 | 3.9 | | [82] |
| | | | | | | | | | 7.9 | [92] |
| 7033 | PTMO | PA12 | 25:75 | | 1.01 | 172 | | | 6.2 | [92] |
| 7233 | PTMO | PA12 | 20:80 | 17.5 | | 170 | | | | [93] |
| | | | | | 1.01 | | | | | [94] |
| | | | | | | | 4.1 | 8.2 | | [82] |

* Phase inversion of Pebax 3533 in water after dip-coating substrate in Pebax solution.
^^ $CO_2/O_2$.
†: [95].
§: Average from Tables 13 & 14.
‡: From histograms of Fig. 19.

### 3.2. Humidity influence on gas separation performance

Attributed to the hydrophilic amorphous PEO chains, Pebax-1657 has exceptionally high water vapor permeability compared with most other polymeric gas-separation materials. Typical water vapor permeability values depend on relative humidity RH% (equivalently water activity $a_w$, assuming equilibrium at the gas-polymer interface), as shown in the works of Doan et al. [96], who measured $H_2O$ permeability of 7598 Barrer at $a_w = 0.3$, 11571 Barrer at $a_w = 0.6$ and 13,007 Barrer at $a_w = 0.9$ (with respective solubilities being: 14.4 $cm^3$(STP)/$cm^3$•cmHg, 20 $cm^3$(STP)/$cm^3$•cmHg and 32.8 $cm^3$(STP)/$cm^3$•cmHg) for a dense (but emeraldine salt-covered) membrane and Akhtar et al. [97], who additionally mentioned that the water vapor permeance of $1.96 \times 10^5$ Barrer (34,386 GPU for thickness 5.7 μm) measured on a free standing membrane at 100 % RH becomes suppressed to the value of 26,676 Barrer (4680 GPU for selective layer thickness 5.7 μm) when the membrane is supported by a macroporous PAN substrate. This suppression was attributed to the fact that the sweep gas flow is not in direct contact with the membrane when a support is present.

In addition, water acts as a plasticizer, further increasing chain mobility and segmental free volume in the PEO domains, which enhances permeability for water vapor, but also for other co-permeating gases. In most reported experimental works on pristine Pebax-1657 membranes, $CO_2/N_2$ selectivity and $CO_2$ permeance were found to increase when measured with humid gas mixtures, compared to the same membranes under dry gas conditions. However, based on data presented in Table 10, this beneficial effect was only observed when relative humidity was at least 60 % and as long as no water visibly liquified at the membrane surface.

It is known that for these elevated humidities the membrane undergoes swelling (swelling degrees are given in section 3.3 "Degree of water-swelling for Pebax-1657"), which enhances permeance through density reduction. In particular, given the hydrophilic and hydrophobic nature of PEO and PA6 segments, respectively, water mostly accumulates in PEO-rich regions, impeding diffusion through PEO, while PEO-swelling-induced mechanical expansion in the less water containing PA6 block, increases the free volume for gas diffusion through PA6, therefore enhancing permeance. The simultaneous positive effect of humidity on selectivity can be explained based on the following two factors: first, the water-induced partial blocking of gas pathways through hydrophilic PEO, which is weakly $CO_2$-selective, directs gas passage through less water-containing PA6, which is highly $CO_2$-selective. Second, $CO_2$ can also pass through the "water pockets" inside the membrane with the mechanism of water-facilitated $CO_2$ transport [98] (Fig. 13), while $N_2$ or $CH_4$ cannot. Note that the absorbed water is contained, mainly as free and at a much lesser percent as bound water, in both the amorphous phase and inside PA6 crystals, which can absorb 5 wt%. $H_2O$ at 80 % RH, according to Parodi et al. [46].

Based on experimental results found in literature, the percentages of humidity-induced increase in selectivity ($\Delta S$) and permeability ($\Delta Pe$) values, in respect with the corresponding dry conditions, are provided in Table 10, as calculated using the following Eqs. 12 and 13:

$$\Delta S = \frac{S_w - S_d}{S_d} \cdot 100\% \quad (12)$$

$$\Delta Pe = \frac{Pe_w - Pe_d}{Pe_d} \cdot 100\% \quad (13)$$

where "w" and "d" indices denote "wet" and "dry" feed gas states.

Furthermore, valuable insight regarding the simultaneous $CO_2$ permeability and $CO_2/N_2$ or $CO_2/CH_4$ selectivity enhancement through Pebax-1657 humidification are provided in the work of Li et al. [99] (Fig. 14), who blended hygroscopic salts into the polymer matrix, thereby revealing that, whilst under dry conditions membrane performance deteriorated by salt addition, the introduction of humidity to feed and permeate gas had a beneficial effect on both selectivity and permeability. In particular, measurements with constant-volume/variable-pressure gas permeation test (time-lag method) for both single gases and binary mixtures, were found to be linearly correlated with membrane's water uptake, as shown in Fig. 15a and b. However, in the more recent work by Fam et al. [100], hygroscopic salt addition was not found to have any beneficial effect on membrane performance in a humid environment. They attributed this to the salt ion complexation

**Table 10**
Humidity-induced selectivity and $CO_2$-permeability increase for $CO_2/N_2$ separation.

| Selectivity increase (%) based on Eq. (12) | Permeability increase (%) based on Eq. (13) | Measurement conditions | | | Ref. |
|---|---|---|---|---|---|
| | | ΔP (bar) | T (°C) | RH (%) | |
| 22.6 | 24.9 | 2 | 25 | 50–60 | [103] |
| −52 | 11.1 | 1 | 40 | 50 | [86] |
| 350* | 2426 | 2 | 25 | 82 | [104] |
| 0 | −13.8 | 2 | 35 | 20–25 | [70] |
| 18.1 | 162.5 | 1 | – | 100 | [105] |
| 14.3** | 21.1 | 4 | 25 | 100 | [106] |
| 7 | 13.3 | 10 | 30 | – | [107] |
| 150** | 428.3 | 1 | 25 | 98 | [108] |

* Liquid water contacted the membrane and selectivity dropped.
** $CO_2/CH_4$.

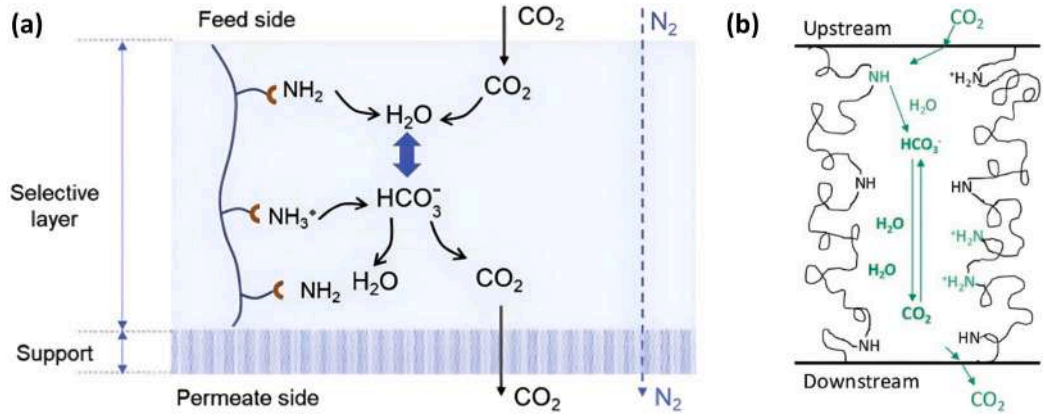


**Fig. 13.** Water-facilitated $CO_2$ transport on (a) primary and (b) secondary (Pebax-1657) amines: complexation of $CO_2$ to the hydrogen carbonate mobile carrier molecule once the gas is dissolved at feed side and decomplexation to gaseous $CO_2$ at permeate side. Reproduced with modifications from: (a) Chen et al. [101]; (b) Dhuiège et al. [102].

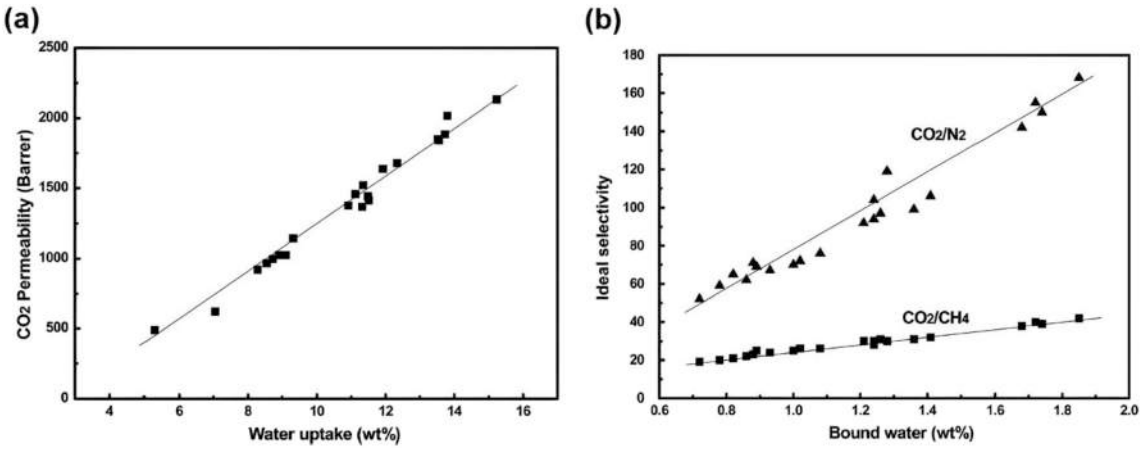


**Fig. 14.** $CO_2$ permeability (a) and ideal selectivity (b) vs. water uptake for Pebax-1657 membrane according to Li et al. [99]. Uptake was regulated by blending alkaline earth chloride salts into the polymer. Reproduced with permission from Li et al. [99].

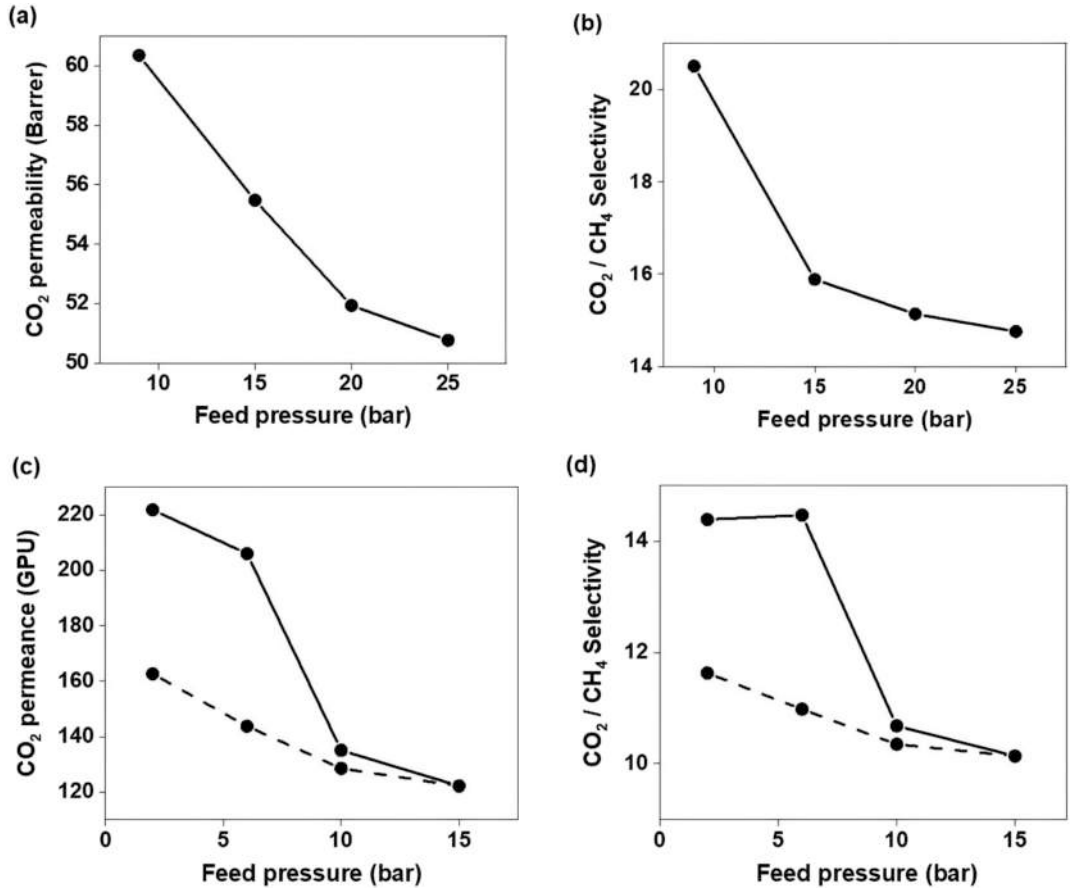


**Fig. 15.** Effect of compaction on pristine $CO_2$ permeation and $CO_2/CH_4$ selectivity of Pebax-1657 membranes, from gas permeation tests with 20/80 *v*/v $CO_2/CH_4$ gas mixture. Panels (a) and (b) correspond to dense, while (c) and (d) to supported hollow fiber membranes. Dashed lines indicate depressurization. Reproduced and modified with permission from Sutrisna et al. [71].

with polymer chains. It must be noted that Fam et al. first dissolved the salt in the solvent and then added the polymer, while Li et al. first dissolved the polymer in the solvent followed by salt addition, which underlines that experimental details/conditions can severely influence the outcome. Additionally, $CO_2$-permeability calculation from measured permeance in the work of Li et al. might have been based on the thickness of the swelled polymer, which would justify the value of approx. 500 Barrer for pristine Pebax-1657 with 5 wt%. water uptake, which is unnaturally high if compared with the usually reported value of approx. 60 Barrer for dry Pebax-1657 (Fig. 19b and d).

### 3.3. Degree of water-swelling

The degree of membrane swelling from a liquid is defined here as the mass ratio $M_s/M_d$, where $M_s$ is the mass of the swollen polymer and $M_d$ the mass of the dry polymer. A swelling degree of 1 represents the lowest possible value, indicating a membrane/liquid system where no swelling occurs. The latter is the case for Pebax 3533 in contact with water. The exceptional resistance to water-swelling exhibited by this grade [109], renders water also as an excellent non-solvent for membrane preparation by phase inversion, using Pebax 3533 polymer dope. Unfortunately, this procedure requires the use of propanol/butanol solvent, which is toxic [110]. For pristine Pebax-1657 membranes, the reported water-swelling degrees commonly lie in the range of 1.05–2.74, as shown in Table S6 (Supplementary).

It should be noted that, if necessary, the presented degrees were recalculated based on the definition provided here. The widespread range of these values is mainly attributed to the low precision of the followed experimental procedure used, as water can evaporate during weight measurement and superficial, adhering water is also included in the measurement. Furthermore, some authors suggest that, if solutes are added to water, then the swelling degree might change. For example, in the case of Pebax-2533 in contact with water containing 50 ppm toluene, the swelling degree was reported to be 1.06 [111], while in contact with water containing 4 wt% isopropanol it was found to be 2.55 [112].

### 3.4. Effects of pressure

Plasticization in the context of polymeric gas separation membranes is the increase in chain mobility (segmental motion) caused by the sorption of a gas or vapor penetrant, leading to a decrease in the polymer's glass transition temperature ($T_g$) and often to a loss of selectivity due to swelling or dilation of the polymer matrix. In specific, unlike glassy polymers that possess low free volume and often undergo plasticization by $CO_2$ at elevated pressures [113], rubbery polymers such as Pebax-1657 are usually not prone to this effect. Increasing $CO_2$ permeability accompanied by a reduction in $CO_2/N_2$ or $CO_2/CH_4$ selectivity with higher pressures is a typical indication of plasticization [114], which has been reported only in a very few cases for Pebax-1657 based mixed matrix membranes [115,116]. However, as shown in Table 11, most reported cases of pristine Pebax-1657 membranes indicate that both $CO_2$ permeability and $CO_2/N_2$ selectivity either increase slightly, or remain almost constant at pressures below 10 bar [117]. On the contrary, at higher pressures, above 10 bar, the opposite trend has been reported, i.e., a slight decrease in both permeability and selectivity with rising pressure, mainly attributed to membrane compaction [118,119]. It must be noted that the latter has also been reported at pressures lower than 10 bar under humid gas conditions [108,120]. Summing up, the changes in $CO_2$ permeability and selectivity with pressure for reported pristine Pebax-1657 membranes are listed in Table 11.

Membrane compaction refers to the phenomenon where a membrane's structure is altered by the force of increased transmembrane pressure [128]. The alteration can involve the collapse of a porous structure and/or material densification resulting in a *FFV* decrease. It can be reversible or irreversible, depending on whether the deformation caused is elastic or plastic, respectively. In the case of dense elastomer membranes, such as Pebax-1657, *FFV* decrease is expected, resulting in a drop in diffusivity and therefore permeability, which is generally known to be more intense for gases with larger molecular diameters [129]. However, in the case of $CO_2/CH_4$ gas pair with kinetic diameters 0.33 nm ($CO_2$) and 0.38 nm ($CH_4$) the opposite behavior is observed, leading to a decrease in selectivity. In this case, since the kinetic diameters of $CO_2$ and $CH_4$ are relatively similar, the size exclusion effect is minimal and as a result, both gases experience a similar decrease in diffusivity, whereas the most significant influence is on solubility. Structural densification of the polymer disproportionately hinders the solubility of $CO_2$ more than $CH_4$, leading to a decrease in $CO_2/CH_4$ selectivity. This becomes also clear by considering the fact, that $CO_2$-philic PEO has a dramatically higher $CO_2$ solubility in its amorphous state, than in its denser semi-crystalline state ($CO_2$ sorption isotherm Henry's constant at 25 °C is approximately 1.3 $cm^3/cm^3$•atm for amorphous PEO vs. 0.375 $cm^3/cm^3$•atm for semi-crystalline PEO [130]). Compaction is thought to hinder access to active sorption centers and at the same time, in scenarios involving mixed gases, the presence of one gas can influence the permeation of another. During compaction, the competitive sorption between $CO_2$ and $CH_4$ can change, which could potentially result in a decrease in $CO_2/CH_4$ selectivity. According to the work of Sutrisna et al. [71], pristine Pebax-1657 undergoes severe, partially permanent, compaction above 8 bar transmembrane pressure, which drops $CO_2/CH_4$ selectivity up to 30 % at 15 bar and $CO_2$ permeance up to 44 % at 15 bar, as illustrated in Fig. 15. The effect was observed in both, dense and supported hollow fiber membranes, but it was more intense in the case of supported membranes.

### 3.5. Effects of concentration

In the Pebax -focused work of Martínez-Izquierdo et al. [16], it was shown that for Pebax-1657 membranes $CO_2$ permeability tends to be 10–20 % higher for low concentration (<15 %) $CO_2/N_2$ mixtures compared to single gas measurements, while $N_2$ permeability remains nearly unchanged between mixture and single gas conditions. This fact results in slightly higher $CO_2/N_2$ selectivity for these mixtures compared with the ideal, single gas selectivity. It must be noticed that, since $N_2$ permeability is not reduced by the presence of $CO_2$, competitive sorption phenomena are negligible within the low (<15 %) $CO_2$ concentration range examined in this publication. Therefore, the presence of the other

**Table 11**
Pressure-induced performance changes for reported pristine Pebax-1657 membranes.

| Membrane type | Pressure range (bar) | $CO_2$ permeability (Barrer) change with rising pressure | $CO_2/N_2$ selectivity change with rising pressure | $CO_2/CH_4$ selectivity change with rising pressure | Ref. |
|---|---|---|---|---|---|
| Dense | 2 → 10 | Increases (80 → 135) | 37.5 → 49 | 12 → 16.5 | [121] |
| Dense | 1 → 9 | Small increase (78 → 85) | 43 → 36 | – | [122] |
| Composite (20 μm on PVC substrate) | 5 → 15 | Small increase (10 → 14) (in GPU) | – | 28 → 26 | [1] |
| Dense | 1.3 → 5 | Approx. constant | Approx. constant | Approx. constant | [123] |
| Dense | 2 → 10 | Approx. constant | Approx. constant | Approx. constant | [124] |
| Dense (or thick composite) | 4, 6, 8 | Small increase (26.51, 33.1, 36.38) | – | (74.26, 77.7, 77.4) | [125] |
| Dense | 4 → 10 | Small increase (50 → 65) | – | – | [126] |
| Dense | 3 → 15 | Increases (120 → 150) | – | 21 → 23 | [127] |
| Dense humidified | 2 → 8 | Decreases (275 → 175) | – | 30 → 18 | [108] |
| Dense | 10 → 25 | Decreases (80 → 55)[a] | – | 97 → 86[a] | [119] |
| Composite | 10 → 25 | Decreases (60 → 50)[a] | – | 20 → 15[a] | |
| Dense | 20 → 50 | Small decrease (55.6 → 52.6) | – | 14 → 12.5 | [118] |

[a] All values of permeability and selectivity changes for Reference 119 are normalized as percentages of the values at 3 bar.

gas provides a benefit of enhanced mobility to $CO_2$ by locally increasing the polymer's free-volume fraction through additional sorbed molecules, without incurring the penalty of sorption competition. However, studies conducted at higher $CO_2$ concentrations (>20 %) [131], report a noticeable decrease in mixed-gas $CO_2$ flux compared to single-gas measurements at equivalent $CO_2$ pressures. This can be attributed to competitive sorption between $CO_2$ and $N_2$ or $CH_4$ molecules, or equivalently, to suppressed $CO_2$ plasticization in the presence of the other gas. Therefore, in this case, the resulting real selectivities are lower than the ideal values. Overall, the observed inversion from $CO_2$ permeability enhancement by the addition of another gas at low $CO_2$ concentrations to $CO_2$ permeability reduction by the addition of another gas at higher $CO_2$ concentrations, can be explained as a result of sorption site saturation at higher $CO_2$ concentrations according to the Henry-Langmuir Sorption Model suggested by W. R. Vieth & K. J. Sladek in 1965 [132]. In agreement with this theory, once all available sorption sites become occupied, the presence of another gas competes for these sites with $CO_2$ and this results in its solubility (and consequently its permeability) reduction.

### 3.6. Effects of other acid gases

Hydrogen sulfide ($H_2S$) is a small, highly condensable, and chemically active acid gas that strongly affects gas-transport behavior in polymer membranes. It has a higher single gas permeability than $CO_2$ with typical values around 350 Barrer at low transmembrane pressures below 1 bar [133]. When present with $CO_2$, it competes for sorption sites in polar polymers and can alter both sorption and transport kinetics. Reviews of polymeric membrane approaches for simultaneous $CO_2/H_2S$ removal note that $H_2S$ has a higher affinity than many non-condensable gases for polar/acidic sites and can therefore modify the dual-mode (Henry + Langmuir) sorption balance that controls $CO_2$ uptake and flux in poly(ether-*block*-amide) materials such as Pebax-1657. This competitive sorption often reduces mixed-gas $CO_2$ permeance relative to pure-gas values and can either delay or aggravate plasticization depending on partial pressures and composition [134]. As a consequence, the presence of $H_2S$ in mixtures with $CO_2$ and $CH_4$ can reduce $CO_2/CH_4$ selectivity significantly [135]. Beyond reversible sorption effects, $H_2S$ raises material-stability concerns for polyamide-containing block copolymers. At elevated pressure, it can induce plasticization and long-term morphological changes. Additionally, $H_2S$ can participate in corrosive or chemically reactive pathways (especially in the presence of water or catalysts), promoting chain scission, oxidation, or other degradation modes in amide domains if conditions permit. For Pebax-type membranes, this means $H_2S$ can accelerate loss of $CO_2/CH_4$ selectivity and permeance over time.

From the process perspective, $H_2S$ influences the most important separation metrics: $CO_2$ permeance, $CO_2/CH_4$ (or $CO_2/N_2$) selectivity, and long-term module durability. Because $H_2S$ often concentrates in the permeate as a highly permeable acid gas, it can contaminate permeate streams and damage downstream units (compressors, amine scrubbers, catalysts) and pose health, safety, and materials-compatibility issues; that is why pre-removal or staged treatment of sour feeds is standard in practice. Pilot and field programs for commercial membranes (e.g., Polaris™) explicitly consider sour-gas exposure and contamination in their testing and scale-up work, since real syngas/natural-gas feeds contain trace $H_2S$ and other contaminants that influence membrane lifetime and overall process economics [136].

Furthermore, $SO_2$ has an even stronger condensability and dipole moment than $CO_2$ or $H_2S$, making it highly interactive with the polar ether and amide groups of Pebax-1657. As a result, even trace $SO_2$ in flue-gas or biogas streams can significantly alter membrane transport behavior. $SO_2$ exhibits very high sorption affinity and readily causes competitive sorption, displacing $CO_2$ and reducing its permeability and selectivity against $CH_4$ or $N_2$. Because of its strong acidity and oxidizing potential, $SO_2$ can also induce irreversible chemical changes, such as amide hydrolysis or oxidation of polyether segments, especially under humid conditions. These processes lead to plasticization, swelling, and eventual loss of mechanical integrity. For this reason, $SO_2$ is usually removed upstream via desulfurization or scrubbing before gas reaches

**Table 12**
$CO_2/CH_4$ separation performance of pristine Pebax-1657 membranes at near room temperature and low (< 5 bar) pressure.

| Type | Thickness (μm) | PA crystallinity (%) | Selectivity $CO_2/CH_4$ | $CO_2$ permeance (GPU) | $CO_2$ permeability (Barrer) | Reference |
|---|---|---|---|---|---|---|
| Dense FS | 30 | 14 | 19 (ideal) | 4.08♠ | 122.4 | [138] |
| Dense FS | 85 | 10.52 | 14.3 (ideal) | 0.54♠ | 45.7 | [139] |
| Dense FS | 80 | 11 | 16 (ideal) | 0.65♠ | 52 | [140] |
| Dense FS | 50 | 9.21 | 20.5 (20/80) | 1.2♠ | 60 | [71] |
| Dense FS | *60* | *8.48* | 16.3 (ideal) | 1.44♠ | 86.4 | [70] |
| Dense FS | 50 | 9.99 | 20.8 (ideal) | 2.2♠ | 110 | [141] |
| Dense FS | – | 10.24 | 18.6 (ideal) | – | 76.2 | [79] |
| Dense FS | 47 | 13.04 | 17 (ideal) | 1.12♠ | 52.6 | [142] |
| Dense FS | 67.5 | – | 12 (10/90) | 0.79♠ | 53 | [108] |
| Dense FS | 24 | 11.68 | 22.7 (ideal) | 4♠ | 96.08 | [74] |
| Dense FS | 70 | – | 18 (ideal) | 0.86♠ | 60 | [143] |
| Dense FS | 29 | – | 19.5 (50/50) | 2.81♠ | 81.35 | [144] |
| Dense FS | 50 | – | 26 (ideal) | 1.3 | 65♠ | [145] |
| Dense FS | 200 | – | 9.5 (ideal) | 0.60♠ | 119.4 | [124] |
| Supported FS* | 0.6 | – | 19 (50/50) | 201 | 120.6♠ | [146] |
| Dense FS ** | 66 | – | 14 (5/95) | 0.80♠ | 52.6 | [118] |
| Dense FS | 110 | 13.9 | 19 (ideal) | 0.76♠ | 84.2 | [147] |
| Dense FS | 40 | 13.1 | 12.5 (ideal) | 1.96♠ | 78.65 | [148] |
| Dense FS | 80 | 11.0 | 16 (ideal) | 0.65♠ | 52 | [140] |
| Dense FS | – | 12.3 | 17.5 (ideal) | – | 53.7 | [149] |
| Dense FS | 90 | – | 20.2 (ideal) | 0.97♠ | 87.6 | [123] |
| Dense FS | 86.5 | 11.1 | 13 (50/50) | 2.40♠ | 208 | [116] |
| Supported FS§ | 2.6 | – | 28 (ideal) | 8 | 20.8♠ | [145] |
| Supported HF*** | ~1 | – | 22.46 (ideal) | 238.36 | 238.36♠ | [3] |

*In parentheses, specify whether the system is ideal or a $CO_2/CH_4$ mixture, indicating the ratio in v/v.*
*Symbol "§" stands for non-commercial, lab-made porous substrate.*
* with PTMSP gutter layer.
** at 20 bar, 30 °C.
*** with cross-PDMS gutter layer.
♠ *The value was calculated according to the definition: permeance (GPU) = permeability (Barrer)/selective layer thickness (μm).*

the membrane unit. Although few studies report quantitative $SO_2$ sorption or permeability in Pebax-1657, with a $SO_2/CO_2$ selectivity of 38.9 [137], experimental data on similar poly(ether-*block*-amide) and polyether membranes show permeability suppression and permanent selectivity loss after repeated exposure. Thus, mitigating $SO_2$ ingress is critical for ensuring long-term stability and consistent $CO_2$-separation performance of Pebax-based membranes.

### 3.7. Literature data on $CO_2/CH_4$ and $CO_2/N_2$ separations

The histograms of Fig. 17, which were derived from experimental data presented in Table 12 ($CO_2/CH_4$) and Table 13 ($CO_2/N_2$), reveal the significant statistical variation in published selectivity and $CO_2$ permeability values regarding dense self-standing Pabax-1657 membranes. In particular, $CO_2$ permeabilities range between 50 and 130 Barrer (with a peak at 60), for both gas mixtures, while the data-dispersion of selectivity values is significantly wider in the case of $CO_2/N_2$ (ranging from 40 to 72, with a peak at 55) versus $CO_2/CH_4$ (ranging from 12 to 28, with a peak at 19). In general, such variations of gas separation performance from sample to sample for the same polymer have been observed in several works, with authors often relating these variations to membrane characteristics, such as thickness, or crystallinity. For example, based on their experimental results, Sánchez-Laínez et al. [83] postulated that for dense Pebax 1041 grade membranes, as thickness decreases, $CO_2$ permeance expectedly tends to get higher, while $CO_2/N_2$ selectivity tends to decrease, even though this could not be related to defects, given the relatively high thickness of the tested membranes. However, in contrast to 1074 grade, Pebax-1657 does not follow this trend and has demonstrated the ability to maintain selectivity even at ultra-low membrane thicknesses.

Despite a few publications on Pebax-1657 that correlate membrane performance with crystallinity and thickness, overall, taking into consideration a wider examination of works on this grade, as presented in Tables 12 and 13, it can be deduced that Pebax-1657 selectivity and permeability cannot be reliably linked to crystallinity or thickness in a predictable manner. This becomes particularly clear from permeability and selectivity data of works using dense self-standing membranes of pristine Pebax-1657, if respective thicknesses and PA-6 crystallinities,

**Table 13**
Pristine Pebax-1657 $CO_2/N_2$ selectivity at near room temperature and low (< 5 bar) pressure.

| Type | PA crystallinity (%) | Selectivity $CO_2/N_2$ | $CO_2$ permeance (GPU) | $CO_2$ permeability (Barrer) | Thickness (μm) | Support pore size (nm) | Ref. |
|---|---|---|---|---|---|---|---|
| Dense FS | – | 42.3 (ideal) | 0.60♣ | 119.4 | 200 | | [124] |
| Dense FS | 10.14 | 67.49 (ideal) | 2.93♣ | 155.6 | 53 | | [154] |
| Supported FS § | – | 48 (ideal) | 2.12♣ | 53 | 25 | -, PES | [117] |
| Dense FS | – | 38.4 (ideal) | 2.11♣ | 211.2 | 100 | | [155] |
| Supported FS *s-c*, § | – | 43.5 (15/85) | 181 | 108.6♣ | 0.6 | -, PSF | [146] |
| Dense FS | 13.9 | 50.1 (ideal) | 0.765♣ | 84.2 | 110 | | [147] |
| Dense FS | – | 77.4 (ideal) | 2.01♣ | 120.8 | 60 | | [156] |
| Dense FS | – | 39 (ideal) | 0.11♣ | 110 | 100 | | [157] |
| Dense FS | – | 48 (ideal) | 1.11♣ | 78 | 70 | | [158] |
| Dense FS | 13.1 | 35.9 (ideal) | 1.965♣ | 78.6 | 40 | | [148] |
| Dense FS | 11 | 54 (ideal) | 0.65♣ | 52 | 80 | | [140] |
| Dense FS | 12.3 | 31 (ideal) | – | 53.7 | – | | [149] |
| Dense FS | 11 | 54 (ideal) | 0.65♣ | 52 | 80 | | [140] |
| Dense FS | – | 42 (ideal) | 0.86♣ | 60 | 70 | | [143] |
| Dense FS | 10 | 71.34 (ideal) | – | 122 | – | | [159] |
| Dense FS | 11.4 | 74.26 (ideal) | 2.65 | 26.5 | 10 | | [125] |
| Dense FS | No data | 57.83 (ideal) | 1.33 | 66.5 | 50 | | [160] |
| Dense FS | 15.03 | 41 (ideal) | 1.17♣ | 105 | 90 | | [161] |
| Dense FS | 12.4 | 55.58 (ideal) | 1.6♣ | 88.06 | 55 | | [162] |
| Dense FS | No data | 48.37 (ideal) | 1.08♣ | 80.97 | 75 | | [163] |
| Dense FS | 13.04 | 51 (ideal) | 1.13♣ | 53 | 47 | | [142] |
| Supported FS § | No data | 47.5 (ideal) | 0.81♣ | 57 | 70 | -, PES | [117] |
| Supported FS *s-c*, ^, $,! | No data | 71.9 [a] (ideal) | 1249 | 10♣ | 0.008 | 8.3†, PAN | [164] |
| Supported FS *s-c*, +, ~ | No data | 32 [b] (20/80) | 342 | 136.8♣ | 0.4 | 10, Zeolite Y on PES | [165] |
| Supported FS *s-c*, @, $ | No data | 58 [c] (ideal) | 190 | 65.17♣ | 0.343 | – | [166] |
| Supported FS *s-c*, #, ^, § | No data | 35.8 [d] (ideal) | 2142.3 | 107.1♣ | 0.050 | 12.5††, PAN | [167] |
| Supported FS "sp", ~, T, § | No data | 50.8 [e] (20/80) | 259.1 | <26♣ | <0.100 | 20, PSF | [7] |
| Supported FS "sp", ^, § | No data | 29.3 [f] (80/20) | 2022 | 60.66♣ | 0.030 | 20, PSF | [168] |
| Supported FS T, >, H, § | No data | 109.6 [g] (10/90) | 1275 | 342.98♣ (for humid membrane, 82 % RH feed, 89 % RH sweep) | 0.269 | 6–16, PES-15 % F127 | [104] |
| Supported FS ^, AF | No data | 68.1[h] (14/86) | 1455 | 101.85♣ | 0.070 | 8.3†, PAN | [4] |
| Supported HF *, § | No data | 42 [I] (ideal) | 481.5 | 144.45♣ | 0.300 | 15.7, PAN | [169] |
| Supported HF | No data | 92 [j] (ideal) | 110.8 | 110.8♣ | 1 | -, PVDF | [170] |
| Supported HF | No data | 32.5 [k] (ideal) | 238.36 | 238.36 | 1 | -, PVDF | [3]* |

Superscript designations "a-k" correspond to the data points in the diagram of Fig. 19.
Symbols "s-c, sp., #, @, ^, AF, +, ~, $,!, T, >, H, *" are explained in Table 14.
Symbol "§" stands for non-commercial, lab-made porous substrate.
In parentheses, specify whether the system is ideal or a $CO_2/N_2$ mixture, indicating the ratio in *v*/v.
* measurements with forced flow through method.
† calculated value based on MWCO to pore diameter correlation suggested by Singh et al. [171].
†† calculated value based on Stokes-Einstein equation with diffusivity from MW-equation of Kim et al. [172].
♣ The value was calculated according to the definition: permeance (GPU) = permeability (Barrer)/selective layer thickness (μm).

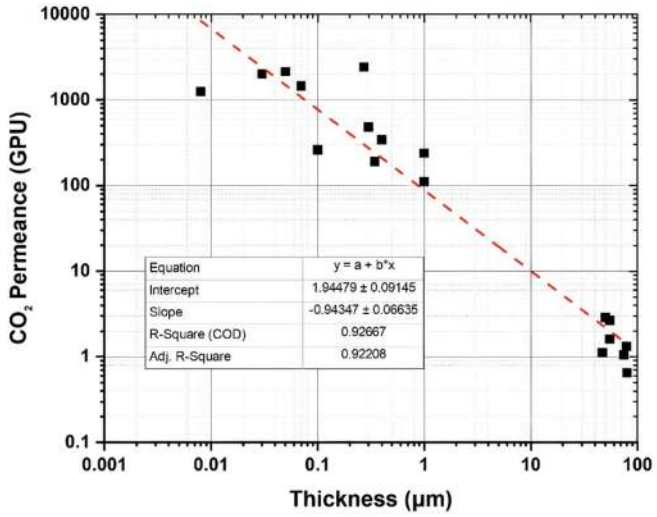


**Fig. 16.** $CO_2$ permeance versus separation layer thickness and corresponding fitting line for $CO_2/N_2$ separation based on literature data of Table 13.

calculated from DSC or XRD measurements, are considered. It can be observed that PA-6 crystallinities ($X_c$) in dense membranes from different works have almost the same values, ranging mostly between 10 and 11 %, with a few exceptions expanding this range to 8.5–15 %. In contrast with these almost unchanged crystallinities, respective selectivities and permeabilities vary widely, ranging from 16 to 22 and 52–110 Barrer for $CO_2/CH_4$ and 41–74 and 52–146 Barrer for $CO_2/N_2$. This implies that parameters other than crystallinity $X_c$ must be accountable for these variations.

Overall, as noted, there is no indication of a link between membrane thickness and selectivity or permeability, nor between crystallinity and selectivity or permeability. However, when both dense and supported pristine Pebax-1657 membranes are considered, an expected strong and clear dependence of permeance on thickness becomes apparent. Based on the literature data in Table 13 ($CO_2/N_2$), there is an approximately linear correlation ($R^2$ = 92.7 %) between the logarithms of $CO_2$ permeance and Pebax-1657 separation layer thickness (Fig. 16), as represented by the following Eq. 14:

$$log(GPU) = -0.9435 \cdot log(microns) + 1.945 \quad (14)$$

As becomes evident by the literature's experimental data points in the plot of Fig. 16, in order to achieve permeances of at least 1000 GPU, which is necessary for entering the commercially applicable target area (Fig. 1a), separation layer thicknesses of less than 300 nm are required. The linearity on a logarithmic scale between permeance and thickness has been reported in recent literature for both PDMS [150] and Pebax-1657 [6]. In particular, the linear correlation in the case of Pebax-1657, as reported by Castro-Muñoz [6], closely matches the one given here.

It should be noted that, despite the lack of a direct correlation between permeability and thickness, overall, there is an indication that supported membranes with thicknesses below 1 μm tend to exhibit lower permeability with decreasing thickness. This trend was first been reported by Fujikawa et al. [150] for PDMS membranes. The authors

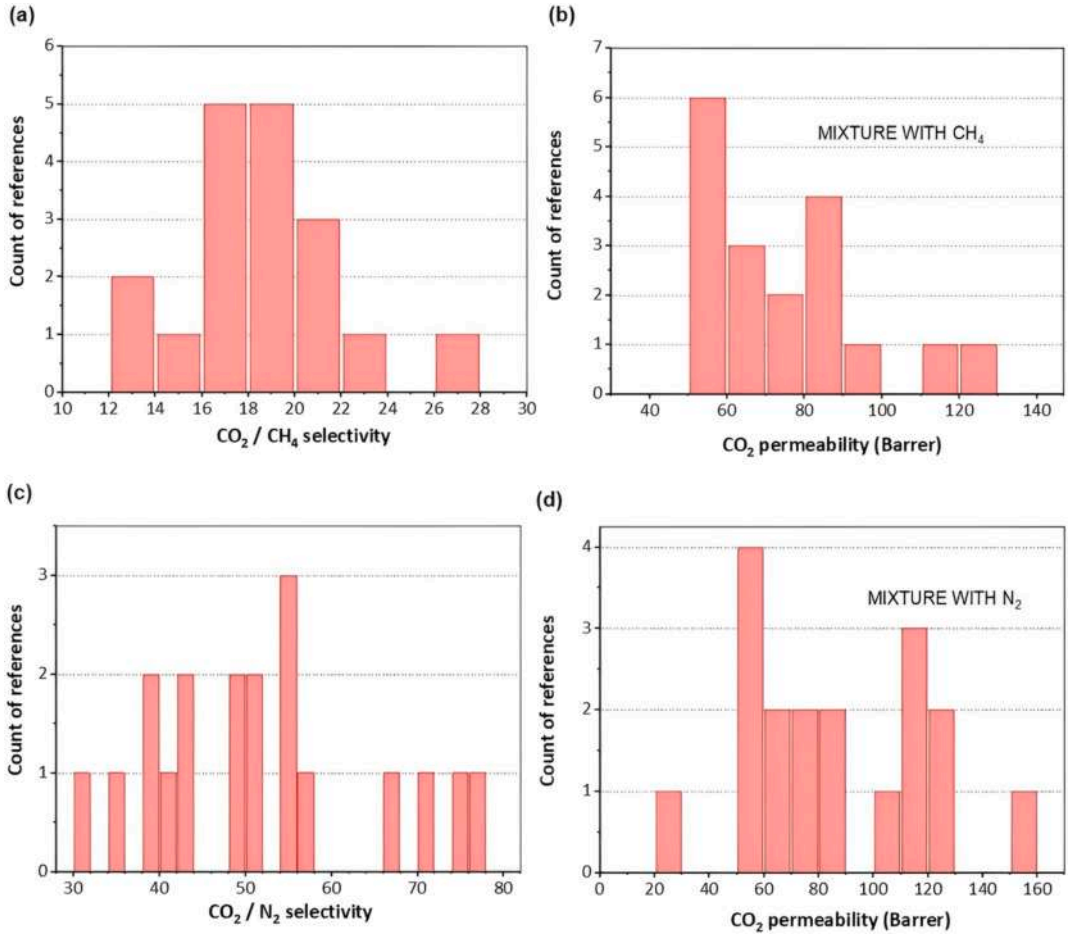


**Fig. 17.** Histograms of selectivity and permeability values reported in selected literature for dense Pebax-1657 membranes, based on data from Tables 12 and 13 for $CO_2/CH_4$ (a & b) and $CO_2/N_2$ (c & d).

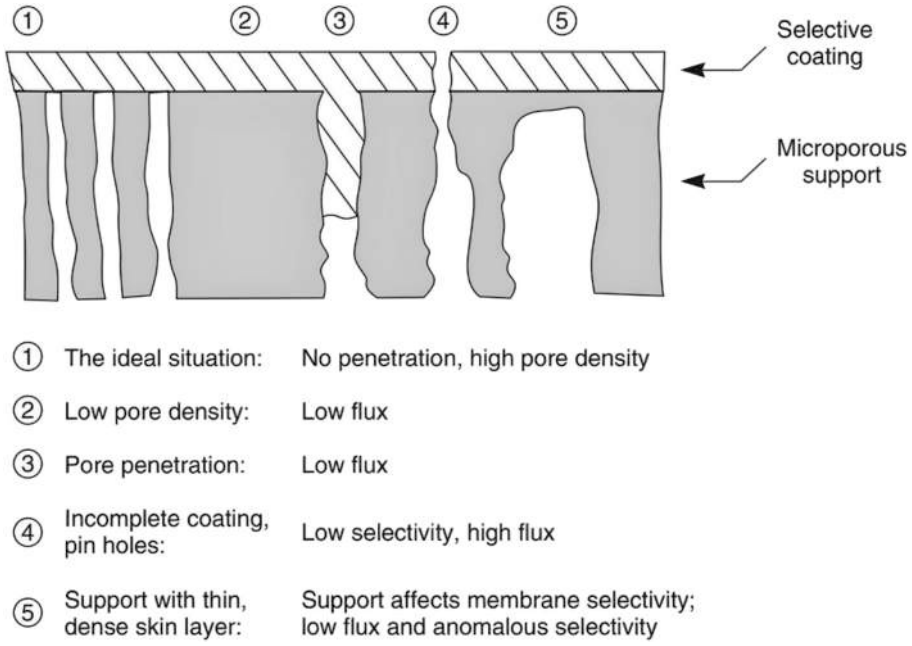


**Fig. 18.** Ideal situation of supported composite membrane vs. most common structural problems deteriorating gas separation performance. Reproduced with permission from Baker [152].

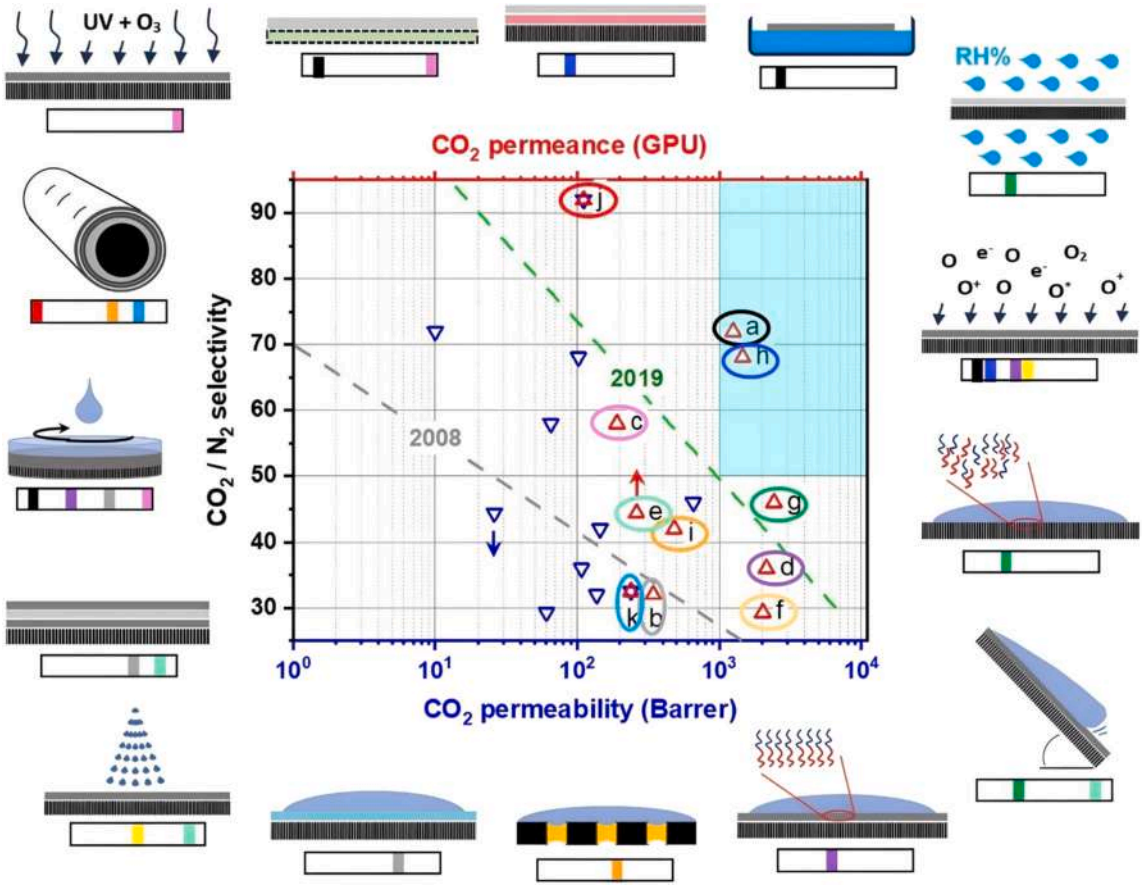


**Fig. 19.** The fabrication techniques and other performance-enhancing aspects that are implemented for each of the top-performing pristine Pebax-1657 membranes referenced a-k in Table 13 are outlined below. The colors below each technique correspond to the data points encircled with the same color. The symbols for techniques are explained in Table 14 and their enhancing effects are discussed in sections 4.1.1–4.1.13. Red triangles are data of selectivity vs. permeance (red x-axis), while blue inversed triangles the corresponding data of selectivity vs. permeability (blue x-axis). The upper bound limit for 2019 in the diagram is adopted from Comesana-Gandara et al. [175] and the upper bound for 2008 is from Robeson [114]. Both upper bounds refer to permeability as the "x-axis".

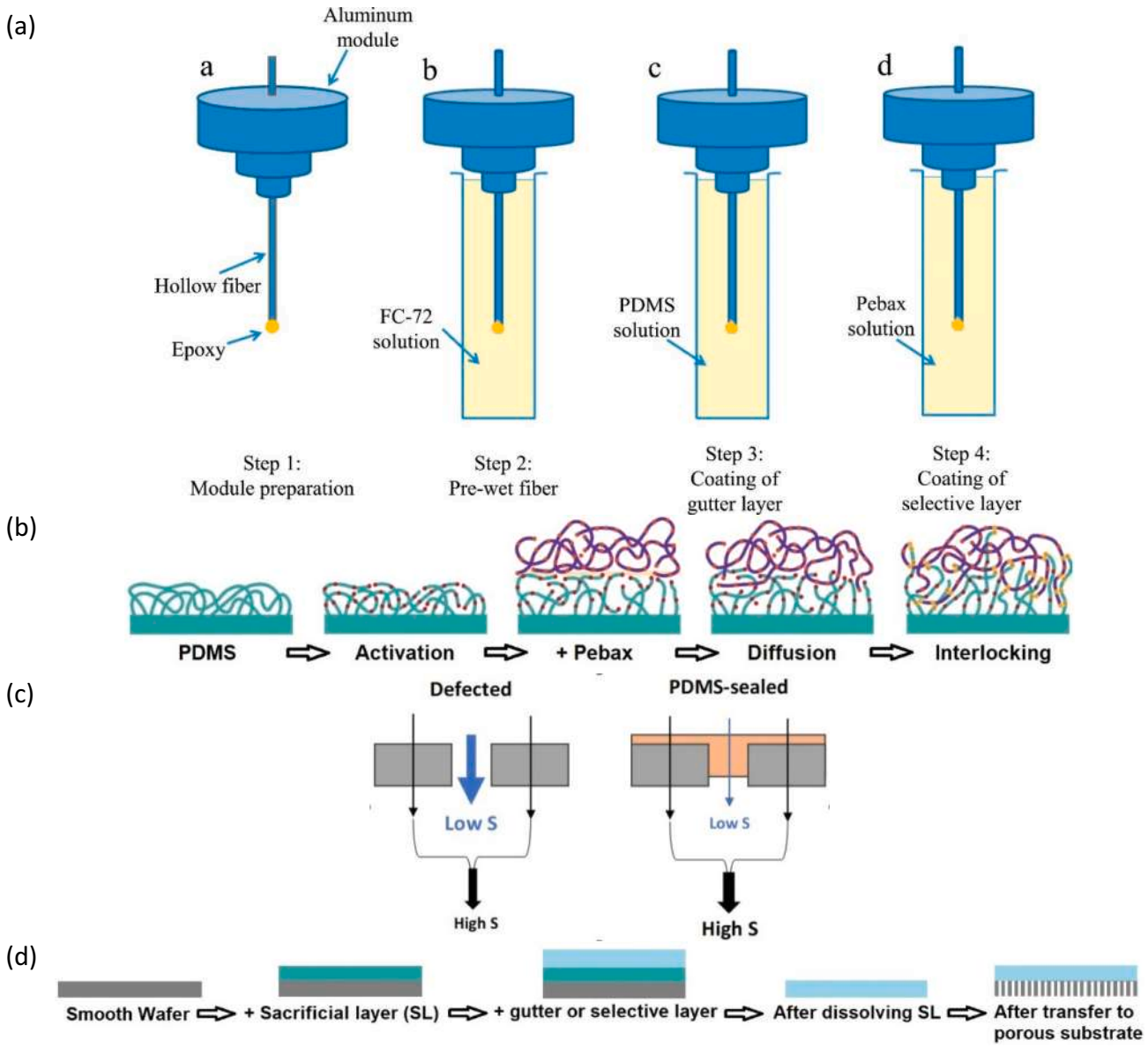


**Fig. 20.** (a) Pore-filling with liquid (FC-72) as an additional step before gutter and selective dip-coating. Reproduced with permission from Chen et al. [169]; (b) Scheme representing Pebax-1657 coating on plasma-treated PDMS. Reproduced and modified with permission from Selyanchyn et al. [164]; (c) Schematic representation explaining the selectivity increase after application of a PDMS cover layer on a defected separation layer of a selective membrane, as reported by Jiang et al. [168]; (d) Use of sacrificial layer for the preparation of smooth, free-standing film.

postulated that as the membrane becomes extremely thin, the most important (slowest) permeation step shifts from diffusion through the thickness to the preceding surface adsorption step. This change in the permeation mechanism renders permeance unchanged despite decreasing thickness, which corresponds to dropping permeability. In a more recent work, Firpo et al. [151] also noticed that for PDMS thin films ranging from 50 nm to 200 μm permeability becomes thickness-dependent. However, they attributed this to polymer chain rearrangement induced by thickness reduction.

Finally, regarding the widespread ranges of reported $CO_2/N_2$ selectivity and $CO_2$ permeance values, for supported pristine Pebax-1657 membranes, in contrast to dense self-standing membranes, it can be partly explained based on the non-idealities commonly encountered in such cases, as schematically described in Fig. 18 [152]. In an ideal scenario (situation 1), the separation/gutter layer rests atop a porous substrate without penetrating into the pores. This occurs when the pores are small in diameter and the pore-density is high enough to provide sufficient flux. However, if the pore-density is low (situation 2), or the pore diameter is too wide, allowing pore intrusion (situation 3), flux, and consequently permeance, are significantly lowered. On the other hand, in cases of pinhole formation in the separation layer (situation 4), because of incomplete coating, or underlying defects in the substrate, permeance may appear high, but selectivity is very low, possibly tending to 1. There are also commonly instances (situation 5), where the support possesses a skin layer (closed pores) resulting in low permeance, but selectivity values can be significantly higher than expected, if the substrate material is more selective than the material of the selective layer. Finally, the approximation of taking the active membrane area as equal with geometrical active membrane area (substrate percent covered by pores is the true active area) can lead to significantly reduced calculated fluxes, permeances and permeabilities compared with the respective true values. The deviation becomes particularly significant in cases

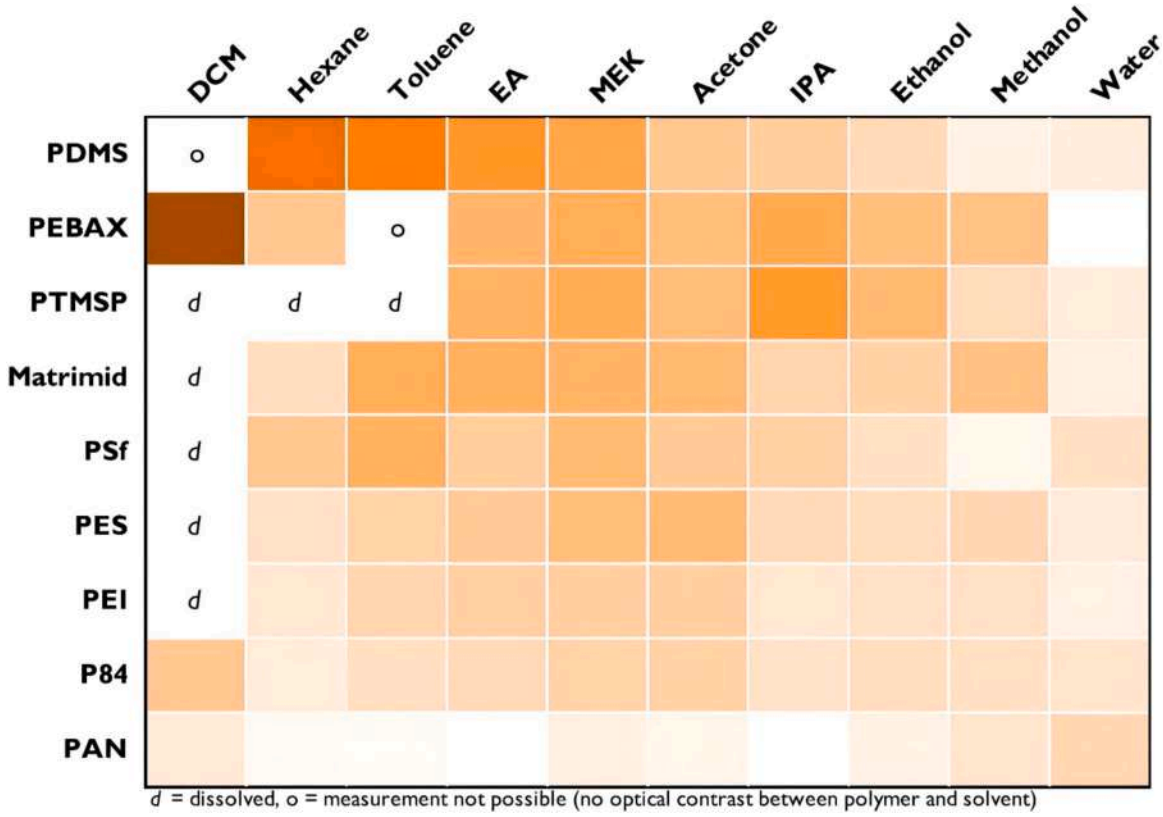


**Fig. 21.** Solvent-polymer interaction magnitude for different solvent-polymer combinations. Deeper color is higher swelling degree, "d" is dissolution, "o" means measurement was not possible (reproduced with permission from Kappert et al. [109]). Pebax here refers to the 3533 grade.

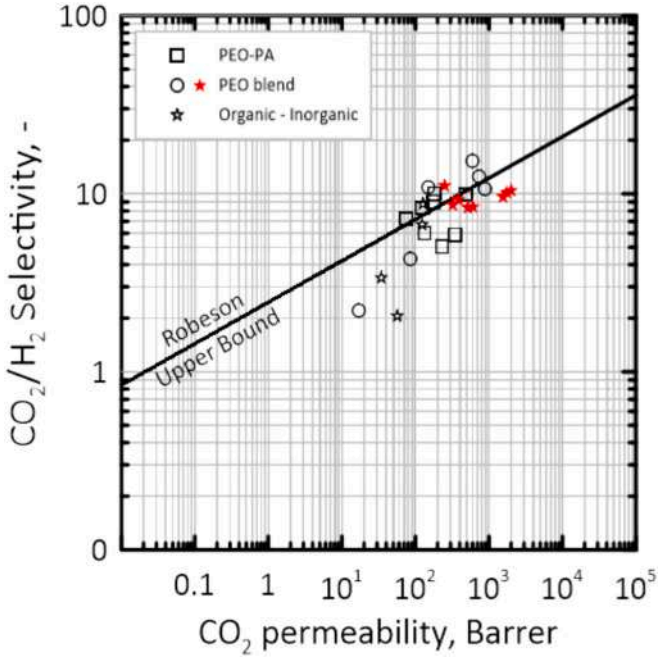


**Fig. 22.** $CO_2/H_2$ selectivity vs. $CO_2$ permeability diagram and Robeson 2008 upper bound for PEO-containing polymers. Reproduced and modified with permission from Liu et al. [199].

where the substrate has low pore density (mostly for "home-made" substrates). Similarly, in measurements of dense membranes, fluxes can be low if the membrane is positioned into the cell directly contacting a porous sintered metal plate without an intermediate mesh, as foreseen by test-cell standards [153].

### 3.8. Long-term stability

The evolution of polymeric membranes for post-combustion $CO_2$ capture has advanced steadily from laboratory-scale evaluations to industrial-scale pilot demonstrations. Early research on Pebax®-based membranes, particularly those incorporating hydrophilic additives such as PEG-MEA and graphene oxide, demonstrated the ability to combine high $CO_2$ permeability with stable selectivity under humid, flue-gas-like conditions. Continuous permeation tests exceeding 60–100 h confirmed the chemical and mechanical stability of the polymeric matrix, with no detectable loss of $CO_2$ flux or selectivity over time [122].

Building on these findings, the development of bio-based Pebax Renew® thin-film composite (TFC) membranes represented a significant step toward industrial viability. These membranes maintained over 95

**Table 14**
Explanations of scheme-symbols used in Fig. 19 and Table 13.

| Spin-coating (s-c) | Spray-coating (sp) | Coating on tilted substrate (T) |
|---|---|---|
| Defect-sealing protective layer (~) | Floating gutter layer (!) | Humid measurement conditions (H) |
| Ozone treatment (@) | $O_2$ plasma treatment (^) | Block copolymer gutter layer (#) |
| Substrate with filled pores (*) | Pre-coating on sacrificial layer ($) | Agent blended into substrate (>) |
| High permeance gutter layer (AF) | Porous hydrophilic layer (+) | |

**Table 15**
Comparison of thin-film deposition methods for Pebax-1657 gas separation membranes.

| Method | Film Thickness Control | Defect Risk | Substrate Compatibility | Pore Intrusion Risk | Lab Scale | Industrial Scale | Max Area | |
|---|---|---|---|---|---|---|---|---|
| | | | | | | | one sample | continuous scale |
| Spin coating | Excellent (sub-μm, uniform) | Low (if flat & smooth) | Flat sheets, rigid wafers or glass | High (unless modified) | Excellent | Poor (limited to wafers) | 100–300 $cm^2$ | Not scalable |
| Spray coating | Good (depends on nozzle) | Moderate (overspray, pinholes) | Flat sheets, curved supports, hollow fibers | Moderate (reduced with pore filling) | Good | Good (R2R, hollow fibers) | 100–1000 $cm^2$ | 100–1000 $m^2$ |
| Drop casting | Poor (thickness gradients) | High (cracks, inhomogeneity) | Flat substrates only | High | Simple | Very poor (too slow) | 10–100 $cm^2$ | Not scalable |
| Dip coating | Good (withdrawal speed dependent) | Low-moderate (edge effects) | Flat sheets, hollow fibers | Low (good wetting) | Good | Excellent (already industrial) | 100–1000 $cm^2$ | 1000+ $m^2$ |

% of their initial $CO_2$ permeance (~1500 GPU) and selectivity after more than 1000 h of continuous operation at 35–40 °C and 90 % relative humidity, whereas preserving surface morphology and interfacial integrity [173]. The demonstrated long-term stability under realistic temperature and humidity conditions highlights the robustness of the Pebax polymer architecture and underscores its potential for sustained deployment in humid flue-gas environments.

As recently reported, the successful transition from laboratory durability studies to field-scale validation was realized by Membrane Technology and Research (MTR) through its Polaris™ membrane process. Initial pilot tests at the U.S. National Carbon Capture Center (NCCC) achieved cumulative operation exceeding 11,000 h, confirming consistent $CO_2$ permeance (~1000 GPU) and $CO_2/N_2$ selectivity of around 50 under real coal-derived flue gas. The success of these trials enabled the construction of a large-pilot plant at the Wyoming Integrated Test Center (ITC), designed to process a 10 MW slipstream (~150 $tCO_2$/day) using a two-stage vacuum membrane configuration with integrated $CO_2$ compression and purification. The facility, now in long-term operation, targets to achieve >90 % $CO_2$ capture with permeate purities exceeding 85 mol%, whereas generating long-term data on membrane module durability and overall process reliability across multi-month campaigns [174].

Consequently, these studies collectively illustrate the continuous advancement of polymeric membrane technology starting from short-term bench-scale stability tests to extended laboratory durability testing, and finally to multi-year industrial validation. The consistent retention of performance, along with sustained tolerance to humidity, impurities, and mechanical resilience across scales, demonstrates that modern Pebax-derived and related polymeric membranes have reached a level of maturity suitable for industrial post-combustion $CO_2$ capture.

## 4. Fabrication techniques and membrane design

### *4.1. Top-performing pristine Pebax-1657 membranes for $CO_2/N_2$ and key fabrication techniques*

As noted with symbols in the selected literature results of Table 13 and the respective diagram in Fig. 19 (clarified in the symbol-explaining Table 14), the ultra-low thicknesses of top-performing membranes have been achieved by implementing membrane preparation techniques that enhance the surface hydrophilicity and/or smoothness of the support and/or gutter layer, while additional defect-clogging is also reported as a final step in two cases (works with reference letters “b” and “e” in Table 13 and Fig. 19). The most successful strategies encountered in literature for implementing these techniques are described in the following paragraphs. Combinations of these strategies are denoted with respective symbols in Tables 14 & 15 and Fig. 19. In particular, in Fig. 19, plots of selectivity versus $CO_2$ permeability (blue inverted triangles), as well as, selectivity versus $CO_2$ permeance (red triangles) are presented for the best-performing pristine Pebax-1657 membranes reported in literature. Labels a-k correspond to the references in Table 13. All selectivities are real values obtained from gas mixture measurements, except for labels “g” and “h”, which represent ideal single gas selectivities. All membranes have a flat sheet geometry, except for “i, j, k”, which are hollow fibers. The light blue rectangle (corresponding to permeance as the x-axis) indicates the target area of industrial applicability, i.e., where the specific cost of Pebax membranes falls below the competitive specific cost of 30 $/ton $CO_2$ (DoE [13]) according to Merkel et al. [12].

As can be observed in Fig. 19, the limited number of membranes within the target area are all in flat sheet geometry. Unfortunately, the more readily up-scalable option of HF geometry, which also offers a higher module packing density, expressed as surface to volume ratio (HF: 500–5000 $m^2/m^3$, spiral wound: 500–1000 $m^2/m^3$, plate frame: 200–500 $m^2/m^3$, tubular: 70–100 $m^2/m^3$) [176,177], still remains a challenge for future research. In the following sections 4.1.1–4.1.13 the key fabrication techniques for the top-performing membranes “a-k” presented in Fig. 19 are described.

#### *4.1.1. Spin-coating selective layer and/or gutter layer*

Spin-coating is widely considered as a widespread standard method, which can lead to the formation of ultrathin films in a repeatable manner. Unlike drop-casting and dip-coating, the adjustment of the rotation speed (rpm) offers an additional parameter to fine tune the method, with the only restriction being the requirement for flat-sheet substrates of relatively small size. This method has been applied to form gutter, selective and protective layers in four works listed in Table 13 and Fig. 19, represented with letters “a, b, c & d”. It should be noted that in works “b” and “d” [165,167], the first spin-coated layer is applied onto the porous substrate, while in “a” and “c” [164,166], it is applied onto a sacrificial substrate. The latter two works are found to result in more selective membranes, while the use of the non-porous sacrificial substrate also offers practical benefits such as higher smoothness and easier mounting (with suction) onto the spin coater.

#### *4.1.2. Spray-coating selective layer and/or gutter layer*

In recent works by Jiang et al. [7,168] (referred as letters “e” and “f” in Table 13 and Fig. 19), spray coating has been introduced as a versatile method for applying both gutter and selective layers onto a substrate, facilitating the fabrication of thin-film composite (TFC) membranes. These membranes are preferred for industrial-scale applications due to their high selectivity and good processability. Notably, in one of their studies [7], they managed to streamline the membrane fabrication process by eliminating the need for a gutter layer. They achieved this by directly spraying the polymer solution containing Pebax-1657 onto a porous PSF substrate under ambient temperature to deposit thin films. The resulting TFC membranes exhibited respectable separation performance, with $CO_2$ permeance exceeding 200 GPU and $CO_2/N_2$ selectivity surpassing 50 in mixed gas tests. In another work [168], they enhanced the interfacial compatibility between the selective and gutter layer by treating the surface of the PDMS gutter layer with air plasma before applying the Pebax-1657 spray coating. This process yielded a defect-

free Pebax-1657 selective layer with an ultrathin thickness as low as 30 nm. The optimized TFC membrane achieved a peak $CO_2$ permeance of 2022 GPU with a $CO_2/N_2$ selectivity approaching 30. These advancements in spray-coating techniques for applying selective and/or gutter layers carries significant implications for large-scale $CO_2$ capture applications, demonstrating the potential of this method for industrial $CO_2$ separation.

#### 4.1.3. Pluronic F127 blended into substrate

In the work of Li et al. (letter "g" in Table 13 and Fig. 19), Pluronic F127 serves as both a pore-forming agent (by micelle formation) and a hydrophilicity-increasing agent when blended into the PES substrate, enhancing the substrate permeance, dropping water contact angle (WCA) down to 42 degrees and improving the adhesion of the selective Pebax-1657 layer, while the selective layer thickness remains almost unchanged. According to the authors, the PEO segments of Pebax-1657 accumulate at the PEO-rich surface of the PES/F127 blend, forming a thin $CO_2$-selective PEO-layer. This PEO-layer is more prone to water-swelling than the bulk Pebax, causing $CO_2$ permeance to increase with the humidity of the gas streams. Simultaneously, since $CO_2$ can permeate through the membrane by water-facilitated transport [98], while $N_2$ does not dissolve in water, the $CO_2/N_2$ selectivity is also much higher in wet samples compared to dry ones (see also section 3.3 "Degree of water-swelling for Pebax-1657"). At too high concentrations of F127 (above 15 % *w*/w), more cylindrical F127 micelles form, which shifts the mean pore diameter to higher values, causes undesired discontinuity in the selective PEO layer and drops selectivity from 110 at 15 % w/w to 46 at 30 % w/w F127 [104].

#### 4.1.4. PDMS-b-PEO blended into gutter layer

An amphipathic PDMS-b-PEO copolymer can be blended with PDMS to render it hydrophilic, since the PEO segments provide hydrophilic groups. As shown by Gökaltun et al. [178], the addition of less than 2 % w/w PDMS-b-PEO to PDMS can, under the condition of keeping the formed film in contact with water for 24 h before use (swelling facilitates migration of PEO segments to the surface), drop the WCA from 100 degrees to 20 degrees or less, without the need for plasma treatment. However, in the work by Liu et al. (letter "d" in Table 13 and Fig. 19), the gutter layer, which consisted of a 1:1 blend of cross-linked PDMS with PDMS-b-PEO copolymer, underwent mild surface treatment with atmospheric air plasma (55 W, 4 s) to etch the surface and reveal PEO segments. In this work, plasma treatment reduced the WCA from 100 to 79 degrees, while the usual issue of $SiO_x$ layer formation (it blocks gases) was avoided by keeping the treatment time very short. The best Pebax-1657 membrane was prepared with a 0.1 wt%. coating solution blade-casted on 4 s plasma-treated PDMS [167]. It must be noted, that coating with Pebax solution in this work had to be performed immediately, within 5 min after plasma treatment, because otherwise, the gutter layer would become less hydrophilic due to the reorientation of polar groups. As reported by Gökaltun et al., preserving hydrophilicity may be feasible when the PDMS-b-PEO content is very low and the gutter layer film is first kept in contact with water for 24 h. Overall, PEO-PDMS *co*-polymers are known as "super-spreaders" and commercially available (e.g., under the trademark "Silwet" by Momentive) and can be used as additives blended into several polymers used in $CO_2$ separation membranes (e.g., Matrimid® [170]).

#### 4.1.5. Pore filling (pre-wetting) with low surface tension liquid

In order to prevent pore intrusion during both the PDMS and Pebax-1657 solution dip-coating steps, Chen et al. [169] (letter "i" in Table 13 and Fig. 19) introduced a pre-wetting step for the substrate using a suitable liquid. "Suitable" is any liquid, that is non-miscible with the polymer-coating solvent and has very low surface tension, in order to fully spread on, impregnate, and fill the pores of the substrate, so that the curvature of the meniscus inside the pore is also minimized, leading to formation of a smooth dip-coated layer on top of it. In particular, in the work of Chen et al., HF substrates were immersed for 5 s into perfluorohexane (FC-72) with a surface tension of 12.23 mN/m at 25 °C [179] and then immediately dip-coated with PDMS in hexane (2 wt%, 5 s). After 48 h of drying, they were coated with Pebax-1657 in $H_2O$/ethanol (0.75 wt%, 3 s) as schematically presented in Fig. 20(a).

#### 4.1.6. Ozone or plasma treatment of gutter layer

Overall, the introduction of polar oxygen-containing groups to the surface of the gutter layer is primarily aimed at enhancing hydrogen bonding and physical segments entanglement at the interface with Pebax, as well as promoting better water-based Pebax solution wetting/spreading to form a thinner layer. A schematic representation of this process and resulting interactions is given in Fig. 20(b), as detailed in the publication of Selyanchyn et al. [164], who implemented plasma treatment on PDMS gutter layer in conjunction with other techniques mentioned here (letter "a" in Table 13 and Fig. 19). Yoo et al. [4] (letter "h" in Table 13 and Fig. 19) also utilized the same treatment, but under different conditions (200 W, 3 min), for the even more hydrophobic Teflon AF2400 gutter layer (WCA drop from 116 to 73.5 degrees), achieving similarly astonishing results. Furthermore, in a work akin to Liu et al. (letter "d" in Table 13 and Fig. 19), Jiang et al. (letter "f" in Table 13 and Fig. 19) treated a cross-linked PDMS gutter layer with vacuum air plasma at 200 W for a short duration of 20 s, dropping the PDMS WCA from 110 to 22.6 degrees. The best Pebax-1657 membrane was obtained using a 0.5 wt% coating solution spray-coated on 10 s plasma-treated PDMS. An additional PDMS protective/sealing layer was also applied in this work [168]. Finally, as an alternative to plasma treatment, ozone treatment of PDMS was implemented by Selyanchyn et al. [166] (letter "c" in Table 13 and Fig. 19) to obtain high-performance membranes, albeit with significantly lower permeance compared to the previously mentioned plasma-based approaches.

#### 4.1.7. Hydrophilic zeolite layer on substrate

Substrate modification to become more hydrophilic [165] (letter "b" in Table 13 and Fig. 19), represents successful attempts toward thickness reduction, when Pebax-1657 solutions (see Table S1 in Supplementary for other grades), which are water-containing (70/30 ethanol/water), are applied to this modified substrate, since they tend to spread on such surfaces. Therefore, integrating a hydrophilic zeolite (a microporous aluminosilicate mineral) layer onto a substrate is a promising approach for enhancing membrane performance, particularly in $CO_2$ capture from flue gas. Chen et al. [165] have successfully advanced this approach by developing novel Pebax/zeolite Y composite membranes. Their work focuses on modifying the substrate to increase its hydrophilicity, facilitating the reduction of membrane thickness. By incorporating a hydrophilic zeolite Y layer, they achieved improved adhesion and spreading of the Pebax-1657 solution, resulting in enhanced membrane formation. Performance testing revealed that the composite membranes exhibited a $CO_2$ permeance of 342 GPU and a $CO_2/N_2$ selectivity of 32. This strategy not only addresses the challenge of thickness reduction but also opens up new possibilities for tailoring membrane properties to specific separation processes. Thus, this study underscores the potential of Pebax/zeolite Y composite membranes for industrial $CO_2$ capture applications, providing a promising solution for reducing membrane thickness while maintaining high selectivity and permeance. Overall, the findings emphasize the importance of substrate modification in optimizing membrane performance and highlight the potential of advanced composite membranes for gas separations.

#### 4.1.8. PDMS cover layer as defect correction for Pebax layer

The concept of adding a protective layer over the selective layer gains significance as the latter becomes very thin making defect formation more likely. For example, in the case of the ultra-thin supported membrane, marked with the symbol "g" in Table 13 and Fig. 19, the authors state that for the dry-state membrane, the selective layer is prone to damage upon pressing [104]. In general, the typically used

PDMS protective and gutter layer is only weakly $CO_2$-selective. According to Merkel et al., the ideal selectivities for $CO_2/N_2$ and $CO_2/CH_4$ in PDMS are 9.5 and 3.16, respectively, with a $CO_2$ permeability of 3800 Barrer [180]. Higher published $CO_2/N_2$ selectivity values of approximately 11 for PDMS on PAN substrate can be explained as the result of PDMS clogging defects in the PAN substrate, which forces gases to permeate through the skin layer of the PAN substrate, as schematically presented in Fig. 20(c) ($CO_2/N_2$ selectivity of PAN is 11.4 according to the early work of S.M. Allen et al. [181]).

In this same manner defect clogging by PDMS cover layer was also found to repair the pristine ultrathin spray-coated Pebax-1657 membranes by Jiang et al. (letter "e" in Table 13 and Fig. 19), as shown in Fig. 20(c), improving selectivity to reach values around 50 for $CO_2/N_2$ without significant permeance reduction [7,168]. Chen et al. (letter "b" in Table 13 and Fig. 19) also applied a protective PDMS layer with similar results [165].

#### 4.1.9. Pre-coating on smooth sacrificial layer

To prevent pore intrusion, which usually occurs when the gutter layer is coated directly onto the porous substrate, a few works have employed a method, schematically shown in Fig. 20(d), involving the initial formation of a very smooth hydrophilic sacrificial polymer layer on a flat surface. The gutter polymer was then deposited on top to form an ultrathin layer. In a subsequent step, the sacrificial layer was dissolved and the remaining gutter layer was transferred onto a porous substrate, which can have large pore diameter and/or high pore density to achieve very high permeance (e.g., PAN ultrafiltration membrane from SolSep BV, UF010104, has a retention (>95 %) for molecules ~10,000 Da and offers 220,000 GPU for $CO_2$ [150]), since pore intrusion is effectively circumvented with this technique.

For example, Selyanchyn et al. (letter "c" in Table 13 and Fig. 19) used ethanol-soluble Polyhydroxystyrene (PHS) as the sacrificial layer and spin-coated a very thin and smooth cross-PDMS layer on it, which was then transferred onto a highly permeable (> 55,000 GPU) porous substrate after PHS dissolution with ethanol. The surface was then modified with ozone to become hydrophilic before being coated with Pebax-1657 [166]. Notably, as an alternative to ethanol-soluble PHS, water-soluble poly(sodium 4-styrenesulfonate) (PSS) can also be used for the same procedure, as demonstrated by the same authors in a more recent work [164,182] (letter "a" in Table 13 and Fig. 19), where the membrane was transferred onto the SolSep BV, UF010104 PAN substrate.

#### 4.1.10. Membrane floating on water

Recently, a floating crosslinked PDMS thin film was recently prepared by dropping its solution onto the surface of warm water, which instantly initiated the crosslinking reaction between Sylgard 184 elastomer parts A and B [183]. The lower-than-water density of the crosslinked PDMS (0.982 g/cm$^3$) allowed it to float on the water surface, which facilitated its transfer onto a scooper/ring. Similarly, Selyanchyn et al. [164] utilized this water-floating ability of crosslinked PDMS, even after a Pebax-1657 layer was deposited on top of it by spin-coating, while a water-soluble PSS layer on a perfectly-even glass surface served as a non-porous, sacrificial substrate underneath. As the PSS layer dissolved in water, the cross-PDMS/Pebax-1657 TFC membrane remained floating on water, allowing its transfer onto a porous substrate practically easily.

#### 4.1.11. Coating of tilted substrate

In the works by Jiang et al. and Li et al. [7,104], the Pebax-1657 solution was either sprayed or shed, respectively, onto a 45-degree tilted surface of a homemade substrate, which was either PDMS-coated, or non-coated, respectively. The tilt apparently helped the solution to spread on the surface more evenly, forming a thinner selective layer with thickness of 100 nm and 271 nm, respectively. Despite the fact that both cases resulted in ultrathin selective layers, a high difference in measured $CO_2$ permeance values (261.3 vs. 2426 GPU, respectively) was observed, which can mainly be attributed to the use of homemade porous substrates with very different permeances.

**Table 16**
Comparison of surface treatments & pore-blocking techniques.

| Technique | Purpose & Effect | Scalability |
|---|---|---|
| Oxygen plasma etching | Increases surface energy, improves wetting and adhesion | Scalable (R2R plasma systems exist) |
| Ozone etching | Mild oxidation, improves hydrophilicity | Scalable, simpler than plasma |
| Additive blending | Modifies viscosity, reduces defects | Highly scalable (solution-based) |
| Substrate pore filling with liquid | Blocks pores to avoid intrusion | Lab-to-pilot feasible, adds complexity |
| Sacrificial substrate followed by film transfer | Prevents pore intrusion, ultrathin free-standing films | Limited scalability (yield issues) |

#### 4.1.12. Use of advanced gutter layer material

According to Yoo et al., whilst a Sylgard 184 layer with a thickness of 200 nm thickness has a measured $CO_2$ permeance of approximately 4000 GPU (which is much lower than its theoretically expected permeance, since below 1 μm permeability drops with decreasing thickness, as reported by Fujikawa et al. [150]), a 200 nm layer of Teflon™ AF2400 achieves 14,000 GPU [4]. Additionally, since the latter polymer contains no Si, in contrast with PDMS and PTMSP, it allows $O_2$-plasma treatment without formation of a permeability-blocking $SiO_2$ layer. However, like PDMS, Teflon™ AF2400 also requires surface modification in order to become hydrophilic (untreated, it has 116° WCA) for use as a gutter layer with Pebax-1657. $O_2$-plasma treatment conducted under vacuum conditions has demonstrated the production of a highly promising membrane, as presented by Yoo et al., with performance values listed in Table 13 (marked with letter "h"). However, the drawbacks in the use of Teflon AF2400 include its relatively high cost and the demand for expensive and highly toxic solvents.

#### 4.1.13. Measurements under humid conditions

Li et al. [104] (letter "g" in Table 13 and Fig. 19) found that the presence of water vapor (RH% >60) in both feed and permeate streams leads to $CO_2$ permeance and selectivity increase, as well as partial recovery of any collapsed substrate pores, thereby enhancing permeance. However, notably the beneficial effect of humidity was pronounced in this work through blending of substrate polymer with Pluronic F127 (PEO-PPO-PEO *co*-polymer), which formed a thin PEO-enriched hydrophilic surface layer that concentrated water and allowed water-facilitated $CO_2$ transport in accordance with the explanations given in section 3.3 "Degree of water-swelling for Pebax-1657". Furthermore, this study provides valuable insights into the practical utility of membranes in $CO_2$ separation, emphasizing their potential for large-scale industrial processes, where humidity is a critical factor.

### 4.2. Practical scalability potential of fabrication methods

Overall, supported $CO_2$ gas separation membranes consisting of ultrathin (sub-micrometer) Pebax-1657 films can be fabricated using various methods: spin-coating, spray-coating, drop-casting and dip-coating. As described in detail in sections 4.1.1–4.1.13, these methods are combined with substrate and/or gutter layer surface modification techniques, such as: oxygen plasma etching, ozone treatment and additive blending, in order to allow the formation of ultrathin films without defects. In parallel, strategies, such as substrate pore filling with liquid during deposition, or deposition on sacrificial substrates followed by film transfer onto the porous supports ensures that no pore intrusion can happen. All these methods are compared in Tables 15 and 16, in terms of achievable membrane surface area and upscaling potential.

As emerges from Table 15, among the examined deposition methods, dip-coating and spray-coating stand out as the most promising candidates for industrial-scale production of ultrathin Pebax-1657 membranes. These methods are compatible with both large-area flat sheets and hollow fiber supports and can also be readily integrated to continuous roll-to-roll processing. On the contrary, spin-coating and drop-coating, although useful for fundamental research and proof-of-concept demonstrations, are restricted to small, rigid substrates of flat sheet geometry and cannot practically be scaled beyond the laboratory. Also, as shown in Table 16, surface modification strategies such as plasma or ozone etching and additive blending are directly scalable and enhance film adhesion and uniformity, whereas use of pore-blocking liquids and sacrificial transfer methods are effective at producing defect-free membranes at the lab-scale, but remain impractical for industrial manufacturing due to their complexity. Overall, the ability to upscale fabrication processes is crucial for translating membrane research into viable commercial separation technologies, with the most effective path combining scalable coating methods (dip- or spray-coating) with scalable surface treatments (plasma, ozone, blending), while the more complex pore-blocking and transfer-based approaches need to be further developed to reduce process complexity.

## 5. Substrates and gutter layers

### 5.1. Typical substrates and gutter layers for supported Pabax-1657 membranes

A typical supported membrane for gas separation possesses a composite structure, where a porous support is overlaid with a highly permeable, yet weakly selective, gutter layer and a thin selective separation layer on top (Fig. 2). In particular, according to a computational study by Kattula et al., a gutter layer thickness of 1–2 times the pore radius of the support yields the maximum improvement in membrane permeance without a significant selectivity decrease, provided the permeability of the gutter layer surpasses that of the selective layer by 5–10 times [184]. At the same time, as emerges from Table 13, membranes exhibiting high performance are either deposited on substrates with pore sizes in the range of 8–20 nm [165], and/or prepared initially via deposition on a sacrificial dense substrate and thereafter transferred onto the porous substrate with such pore sizes [164,166]. Narrower pores are expected to lead to very low permeance, while wider pores are more prone to defect formation. Given the highly significant impact of pore diameter, it is recommended to use the method of perporometry, also known as capillary flow porometry (CFP), for substrate characterization prior to conducting membrane measurements. This is in particular pertinent when the substrate is homemade (works with letters "d, e, f, g, i" in Table 13 / Fig. 19), or has unknown pore-characteristics [185]. Typical materials employed as gutter layers for Pebax-based membranes are shortly outlined below:

#### 5.1.1. PTMSP

This polymer exhibits a $CO_2$ permeability of approximately 37,000 Barrer with a $CO_2/N_2$ selectivity of 6 [186,187]. Even though PTMSP initially exhibits high $CO_2$ permeability, this value drops rapidly over time due to intense physical ageing of the polymer [188]. Nevertheless, in a considerable number of works report thin-film composite Pebax-1657 gas separation membranes that utilize a PTMSP gutter layer resting on a microporous HF substrate. For example, PVDF ultrafiltration hollow fiber membranes with a pore diameter of 50 nm, dip-coated 3–4 times with PTMSP, can result in a relatively effective pristine Pebax-1657 gas separation membrane [70,170,189,190].

**Table 17**
Gas permeabilities of PDMS membranes crosslinked at different temperatures (Barrer). Reproduced with permission from Berean et al. [191].

| Penetrant | 25 °C | 50 °C | 75 °C | 100 °C | 150 °C |
|---|---|---|---|---|---|
| $CH_4$ | 850 | 940 | 1000 | 860 | 480 |
| $N_2$ | 360 | – | 590 | – | 280 |
| $CO_2$ | 3180 | 3430 | 3970 | 3190 | 1150 |

#### 5.1.2. Commercial cross-linked PDMS

The commercial Dow Corning Sylgard 184 elastomer with PDMS-base comprises two liquid parts/components, which are mixed in a "base" to "curing agent" weight ratio of 10:1. Curing leads to solidification after 24 h at 23 °C, 4 h at 65 °C, or 1 h at 100 °C. Different curing temperatures lead to different gas permeabilities, with an optimum value at 75 °C, as shown in Table 17.

#### 5.1.3. Non-commercial cross-linked PDMS types

Cross-linked PDMS gutter layers, commonly used, are prepared by curing of deposited mixtures containing OH-terminated PDMS, tetraethoxysilane (TEOS) cross-linker and dibutyltin dilaurate (DBD) catalyst [3,168,190,192]. The mechanism entails the interaction between hydroxyl (OH) groups in PDMS and silanol (Si-OH) groups in TEOS through condensation reactions, forming siloxane bonds and leading to the crosslinking of PDMS with TEOS. A simplified representation of this crosslinking mechanism is as follows:

Hydrolysis of TEOS

$$TEOS + H_2O \rightarrow Si(OH)_4$$

Hydrolysis of OH-terminated PDMS

$$PDMS - OH + H_2O \rightarrow PDMS - O^- + H_3O^+$$

Condensation with catalyst

$$Si(OH)_4 + PDMS - O^- \rightarrow PDMS - O - Si - O - Si - O - Si - OH + H_3O^+$$

Polymerization and Crosslinking

$$PDMS - O - Si - O - Si - O - Si - OH + PDMS - O^- \rightarrow (PDMS - O - Si - O - Si - O - Si)_n + H_3O^+$$

In a slightly modified method for turning the PDMS gutter layer hydrophilic, $NH_2$-containing (3-Aminopropyl)triethoxysilane (APTES) is added to the mixture solution, in order to form a PDMS coating layer containing $NH_2$-groups [193]. PVP grafting onto these $NH_2$-groups renders the surface hydrophilic (with a WCA of 28.1° after 50 s immersion time), while $CO_2$-permeance remains adequately high at 1500 GPU. Alternatively, aiming to increase hydrophilicity, the amphipathic PDMS-b-PEO copolymer can also be used instead of APTES/PVP [167]. Alternatively, a mixture of vinyl-terminated PDMS with amino silicone (containing $NH_2$– and Si—H— groups) can also be used [194]. In this reaction, the vinyl group (-CH=$CH_2$) of vinyl-terminated PDMS reacts with the Si—H group of amino-silicone resulting in the formation of a solid crosslinked polymer network. The reaction is catalyzed by a platinum-based catalyst [194]. Finally, (bicycloheptenyl)ethyl -terminated PDMS can be cross-linked through ring-opening metathesis polymerization reactions, as described in the work of Hong et al. [195], who studied the influence of cross-linking density on $CO_2$ permeability and observed a maximum of 6800 Barrer at a cross-linking density of $1.19 \times 10^{-5}$ mol•$cm^{-3}$.

### 5.2. Solvent effects during drop-casting

The adhesion among substrate, gutter, and selective layers can be influenced by the solvents used during each dip-coating step. Swelling or partial dissolution are possible outcomes, which can lead to stronger adhesion and make it more difficult to distinguish between layers in SEM images. Kappert et al. investigated the effects of various commonly used solvents on the most common gutter and substrate materials found in Pebax-based composite membranes [109]. Their results are summarized

in the diagram of Fig. 21. Even though the examined grade in the work of Kappert et al. was Pebax-3533, for example, it becomes evident that the 70:30 ethanol/water system used for dip-coating with Pebax-1657 induces a more pronounced swelling effect on PTMSP than on the PDMS gutter layer.

## 6. Gas separation for other gas pairs

Pristine Pebax membranes have been widely recognized for their good processability, flexibility, and inherent selectivity toward polar gases such as $CO_2$ and $H_2S$ due to the presence of polyether segments that interact favorably with condensable gases. However, despite these advantages, the intrinsic $H_2S$ permeability and selectivity of pristine Pebax remain relatively limited, restricting its applicability for efficient acid gas separation. Reported studies show $H_2S/CO_2$ selectivities of ~3.6 and $H_2S/CH_4$ selectivities of 51–57 indicating low discrimination between $H_2S$ and $CO_2$ but strong selectivity over $CH_4$. This results from the similar polarity and size of $H_2S$ and $CO_2$, which interact comparably with Pebax, while nonpolar $CH_4$ shows much weaker interaction and diffusivity. Thus, pristine Pebax provides a stable yet moderately selective base that benefits from further modification to enhance $H_2S/CO_2$ separation.

The long-term gas separation performance and stability of Pebax-1657 membranes were systematically evaluated under humid sour gas conditions containing $H_2S$, $CO_2$, and $CH_4$ [118]. Experiments were conducted at 30 °C and operating pressures of 20 and 40 bar, with humidity levels ranging from 400 to 1700 ppm, corresponding to RH values between 19 % and 80 %. The influence of humidity on permeability and selectivity was examined over extended operation periods to assess the membrane's robustness and potential for natural gas sweetening applications. At 20 bar and 30 °C in the presence of 15 % $H_2S$, the introduction of humidity (400–1700 ppm) caused only minor variations in $H_2S$ permeability, which remained close to its original value after 150 h of continuous operation. Increasing humidity resulted in a slight decrease in $CO_2$ and $H_2S$ permeabilities (up to 6 % and 2 %, respectively) but led to enhanced $CO_2/CH_4$ and $H_2S/CH_4$ selectivities by approximately 5 % and 10 %. Upon humidity removal, membrane performance returned to initial levels, indicating reversible behavior. Similar trends were observed at 40 bar, where humidity introduction caused a small reduction in permeability but a minor increase in selectivity, confirming the membrane's consistent behavior at higher pressure. Long-term testing over 450 h, including 360 h in $H_2S$ and 190 h in humid $H_2S$ conditions, showed that Pebax-1657 maintained excellent stability with negligible degradation. The slight decline in $CO_2$ permeability during prolonged exposure was attributed to minor compaction rather than humidity effects. These findings suggest that the hydrophilic and rubbery nature of Pebax, combined with competitive sorption among $H_2S$, $CO_2$, and $H_2O$, contributes to increased selectivity while preserving permeability.

Moreover, the exceptional properties of Pebax films, including their ease of casting and excellent mechanical resistance, make them highly suitable for investigating the recovery of difluoromethane (R32) from the near-azeotropic refrigerant mixture R410A, composed of 50 wt% R32 and 50 wt% pentafluoroethane (R125) [214]. R32 exhibits high permeability exceeding 200 Barrer due to its small molecular size and high solubility in the Pebax copolymer, while Pebax demonstrates moderate selectivity, enabling effective separation of R32 from R410A. These characteristics highlight Pebax as a promising membrane material for the practical application of membrane technology in the recovery of value-added compounds from azeotropic or close-boiling refrigerant mixtures.

The demonstrated and proven versatility and efficiency of Pebax-based membranes in separating complex mixtures such as R32/R125 have inspired their further application in $CO_2/CO$ separation, taking advantage of Pebax's excellent permeability-selectivity balance and mechanical stability under industrially relevant conditions. $CO_2/CO$

**Table 18**
Selectivity values of pristine Pebax-1657 membranes for gas pairs other than $CO_2/N_2$ and $CO_2/CH_4$.

| Gas pair | Selectivity | Type | ΔP (bar(a)) | T (°C) | Reference |
|---|---|---|---|---|---|
| $CO_2/H_2$ | 9.1 | Dense | 2 | 25 | [139] |
| | 9.5 | Dense | 4 | 35 | [25] |
| | 9.2 | Dense | 2 | 25 | [169] |
| | 9.1 | Dense | 0.6 | 30 | [67] |
| | 8.1 | Composite | 5 | 20 | |
| | 9.1 | Dense | 1 | 30 | [200] |
| | 8.4 | Composite | 1 | 30 | |
| | 11 | Dense | 2.3 | 21 | [201] |
| | 5.0 | Dense | 3 | 35 | [202] |
| | 10.3 | Dense | 1 | 25 | [160] |
| | 4.1 | Dense | 4 | 25 | [203] |
| | 9.1 | Dense | 0.6 | 30 | [204] |
| | 9.0 | Dense | 1 | 30 | [63] |
| $CO_2/O_2$ | 19.7 | Dense | 3 | 25 | [71] |
| | 20.8 | Dense | 4 | 35 | [25] |
| | 21 | Dense | 1 | 30 | [63] |
| | 22.5 | Dense | – | 30 | [205] |
| $CO_2$/He | 15.9 | Dense | 4 | 35 | [25] |
| | 6.6 | Dense | 3 | 25 | [159] |
| $CO_2/CO$ | 30.2 | Dense | 1 | 30 | [198] |
| | 48.3 | Composite | 4 | 25 | [196] |
| $H_2/CH_4$ | 1.9 | Dense | 1 | 25 | [206] |
| | 2.4 | Composite | 2 | 30 | [207] |
| | 3.24 | Composite | 4 | 25 | [203] |
| | 2.55 | Dense | 10 | 35 | [208] |
| | 2.02 | Dense | 4 | 25 | [209] |
| | 2 | Dense | 1 | 30 | [63] |
| | 1.9 | Dense | 1 | – | [210] |
| | 1.69 | Dense | 4 | 35 | [25] |
| | 2.12 | Dense | 7 | 35 | [211] |
| $CH_4/N_2$ | 3.12 | Dense | 1 | 25 | [79] |
| $He/CH_4$ | 21.6 | Composite | 0 | 25 | [212] |
| $He/N_2$ | 4.0 | Dense | 1 | 25 | [79] |
| | 18.4 | Composite | 0.3 | 25 | [212] |
| $H_2/N_2$ | 5.62 | Dense | 1 | 25 | [160] |
| | 6.0 | Dense | 1 | 25 | [79] |
| | 6.0 | Dense | 1 | 25 | [206] |
| $H_2O/N_2$ | 10,000 | Composite | Modified upright permeability cup method (modified ASTM E96B) | 21 | [97] |
| | 1800 | Composite | 0.0034 | 21 | [213] |
| $H_2O$/DME | 24–40 | Dense | 3 | 35 | [96] |
| $C_4H_{10}/CH_4$ | 9.6 | Dense | 0.6 | 30 | [67] |
| | 12.3 | Composite | 1.2 | 30 | |
| $C_3H_6/C_3H_8$ | 2.9 | Composite | 1 | 30 | [81] |
| $H_2S/CH_4$ | 51 | Dense | 10 | 35 | [200] |
| Ternary mixture | 62.2 | Dense | 20 | 30 | [118] |
| | 70.4 | Dense | 20 | 30 | |
| $H_2S/CO_2$ Ternary mixture | 3.59 | Dense | 10 | 35 | [200] |
| $H_2S/CO_2$ | 3.52 | Dense | 0.05 | 40 | [133] |
| $H_2S/CH_4$ | 57.1 | Dense | 0.05 | 40 | |
| $CH_2F_2$/ $CF_3CHF_2$ 50/50 wt% | 7.0 | Dense | 0.86 | 30 | [214] |
| $O_2/N_2$ | 2.4 | Dense | 3 | 25 | [71] |
| | 6.6 | Dense | 5 | 25 | [201] |
| | 6.1 | Dense | 5 | 25 | [202] |
| | 3.94 | Dense | 5 | 28 | [203] |
| | 2.48 | Dense | 1 | 25 | [160] |
| | 3.0 | Dense | 3 | 25 | [204] |
| | 3.4 | Dense | 4.9 | 25 | [205] |
| | 7.8 | Dense | 4 | 25 | [198] |
| | 2.56 | Dense | 1 | 25 | [79] |
| | 3.4 | Dense | 10 | 30 | [72] |
| | 2.5 | Dense | 1 | 25 | [206] |
| | 3.4 | Dense | 3 | 25 | [159] |
| | 4.3 | Dense | 0.3 | 25 | [212] |

separation is now as significant as $CO_2/N_2$ and $CO_2/CH_4$ separations, as the related technologies are vital for climate change mitigation and the transition toward sustainability by enabling the production of high-value chemicals from industrial byproducts [196,197]. In this context, D.S. Karousos et al. developed composite HF membranes by coating porous polyimide/graphene nanoplatelet HFs with a PDMS gutter layer and a Pebax-1657 selective layer employing an upscaled, innovative HF coating device based on an underflow drop-casting technique. The membranes were evaluated for $CO_2/CO$ separation using a binary $CO_2$/CO (33/67 vol%) mixture, simulating a Linz-Donawitz converter gas (LDG) byproduct stream from the steel industry, as the feed under elevated pressure. The $CO_2/CO$ selectivity reaches a maximum of approximately 50 at 4 bar(a). Beyond this pressure, the selectivity gradually declines and stabilizes around 40 at higher pressures up to 8 bar(a). This performance surpasses the reported the $CO_2/CO$ selectivity of 30 for a pristine Pebax-1657 dense membrane with flat-sheet geometry [198]. Similarly, Pebax membranes exhibit promising and strong potential for $CO_2/CO$ separation, achieving an effective trade-off between permeability and selectivity. Their flexible copolymer structure facilitates efficient $CO_2$ transport due to strong $CO_2$-polymer interactions, while maintaining sufficient mechanical stability for operation under elevated pressures, making them attractive candidates for industrial gas separation applications.

In Table 18 pristine Pebax-1657 membrane selectivity values are given for each of different binary gas separations, according to one or more published works. For each value, specific measurement conditions regarding membrane type, transmembrane pressure, and temperature are denoted in parentheses. References are listed in the same sequence as the corresponding values. Among the most scarcely reported gas separations for pristine Pebax-1657, the $CO_2/CO$, $He/CH_4$ and $H_2S/CH_4$ gas pairs stand out for their comparatively high selectivities, while $CH_4/N_2$, $CO_2/H_2$ and $CO_2$/He selectivities are inversed in comparison with most other polymeric membrane materials. In Fig. 22 the typical example of $CO_2/H_2$ selectivity-permeability diagram for PEO-containing polymers is presented, with the noticeable characteristic Robeson upper bound with positive slope.

## 7. Perspectives, unresolved issues

Overall, the reported $CO_2$ permeances exceeding 1000 GPU and $CO_2/N_2$ selectivities over 50 demonstrate clearly that ultrathin supported membranes composed of pristine Pebax-1657 grade, without any filler or additive, exhibit performance levels within the range of industrial applicability for $CO_2$ capture from flue gas. The few outstanding works that have presented such membranes to date have implemented similar fabrication techniques to achieve ultrathin structures. In particular, the best reported performances under dry conditions so far, have been achieved for thicknesses of 70 nm or lower. These thicknesses were achieved by implementing oxygen plasma etching to render surface of the planar gutter layer hydrophilic, enabling uniform coverage with a very thin Pebax-1657 solution. Performance enhancement by adding humidity to both membrane sides, was shown to allow reaching the same performance even with a 270 nm thick separation layer. However, all of these works exclusively focused on flat sheet membranes and implemented either spin- or spray- coating methods for applying the Pebax layer. Given that spin-coating upscaling for large membrane areas is not feasible and that conventional air-assisted spray coating often leads to inhomogeneous layer thickness, the need emerges to explore new improved coating techniques, such as ultrasound-assisted spray-coating. Furthermore, reducing thickness of the selective Pebax-1657 layer on hollow fiber substrates to below 300 nm, in order to reach permeances comparable to supported flat sheet membranes, remains a major challenge. Finally, data scarcity on pristine Pebax-1657 membrane separation data regarding gas pairs, such as $CO_2/CO$, $H_2/CH_4$, $He/N_2$, $H_2S/CH_4$ and $H_2S/CO_2$, also opens promising paths for future exploration.

## 8. Conclusions

Poly(ether-b-amide) (PEBA) copolymers have emerged as highly promising materials for gas separation membranes, particularly in $CO_2$ capture applications, presenting an auspicious balance between permeability and selectivity. This review explores the recent advancements in utilizing PEBA copolymers, focusing on Pebax grades, for enhancing gas separation efficiency. Through a comprehensive analysis of research efforts, it is evident that current strategies are predominantly centered on chemical modification and mixed-matrix concepts to optimize membrane performance. However, notably, Pebax-1657 has garnered significant attention due to its solubility in environmentally friendly solvents, excellent performance in $CO_2$ gas separation and versatile application potential. The microstructural features of PEBAX membranes, including crystallinity and polymer chain arrangement, significantly influence their performance. Moreover, progress in membrane fabrication techniques, such as defect-free ultrathin separation layers, contribute to enhancing membrane efficiency. Membrane systems, like Polaris™, demonstrate the practical feasibility of PEBA-based membranes at a pilot scale. Finally, the review discusses critical factors impacting membrane performance, including permeance-thickness relation, crystal size, polymorph structures and crystallization temperatures, providing insights into future research directions. In particular:

- *FFV*, a key parameter in membrane performance, was calculated based on van der Waals volumes, yielding a value of 0.134 for Pebax®-1657.
- Humidity-induced swelling at 60 % RH or higher enhances selectivity and permeability in $CO_2/N_2$ gas mixtures due to density reduction and water-facilitated $CO_2$ transport.
- High transmembrane pressures above 8 bar(a) lead to irreversible compaction, reducing $CO_2/CH_4$ selectivity and $CO_2$ permeance.
- In contrary to expectations, there was no clear correlation found between thickness, crystallinity, and membrane performance. Despite similar crystallinity, the selectivity and permeability presented wide variations among different studies, suggesting that other factors influence performance.
- Various methods such as spin-coating, spray-coating and surface modifications were explored to optimize membrane performance. Surface hydrophilicity enhancement and defect reduction were found to significantly enhance performance.
- Different gutter materials and coating methods significantly impacted membrane performance, especially regarding $CO_2$ permeance and selectivity.

In conclusion, this review of pristine Pebax-1657 membranes for $CO_2$ gas separations highlights their potential and versatility in addressing the urgent challenges of carbon capture and separation. Despite the inherent advantages, challenges remain in terms of optimizing membrane thickness, enhancing mechanical stability, ensuring reproducibility and scaling up for industrial applications. Further research should focus on overcoming these hurdles, exploring novel composite materials and further refining processing and fabrication techniques. This approach aims to unlock the full potential of Pebax-1657 membranes in $CO_2$ separation technologies.

## CRediT authorship contribution statement

**Dionysios S. Karousos:** Writing – original draft, Methodology, Investigation, Data curation, Conceptualization. **George V. Theodorakopoulos:** Writing – original draft, Validation, Methodology, Investigation, Data curation. **Xuezhong He:** Writing – review & editing, Validation, Supervision. **George Em. Romanos:** Writing – review & editing, Validation, Supervision. **Adele Brunetti:** Writing – review & editing, Validation, Supervision. **Evangelos P. Favvas:** Writing – review & editing, Validation, Supervision, Methodology, Conceptualization.

## Declaration of competing interest

The authors declare that they have no known competing financial interests or personal relationships that could have appeared to influence the work reported in this paper.

## Appendix A. Supplementary data

Supplementary data to this article can be found online at https://doi.org/10.1016/j.cej.2025.170938.

## Data availability

Data will be made available on request.

## References


[1] A.S. Embaye, L. Martínez-Izquierdo, M. Malankowska, C. Téllez, J. Coronas, Poly (ether-block-amide) copolymer Membranes in $CO_2$ separation applications, Energy Fuel 35 (21) (2021) 17085–17102, https://doi.org/10.1021/acs.energyfuels.1c01638.

[2] Y.-W. Hong, L. Laysandra, Y.-C. Chiu, D.-Y. Kang, Vacuum-assisted self-healing amphiphilic copolymer Membranes for gas separation, ACS Appl. Mater. Interfaces 15 (28) (2023) 34075–34086, https://doi.org/10.1021/acsami.3c06518.

[3] Y. Zhang, K. Sheng, Z. Wang, W. Wu, B.H. Yin, J. Zhu, Y. Zhang, Rational design of MXene hollow Fiber Membranes for gas separations, Nano Lett. 23 (7) (2023) 2710–2718, https://doi.org/10.1021/acs.nanolett.3c00004.

[4] M.J. Yoo, K.H. Kim, J.H. Lee, T.W. Kim, C.W. Chung, Y.H. Cho, H.B. Park, Ultrathin gutter layer for high-performance thin-film composite membranes for $CO_2$ separation, J. Membr. Sci. 566 (2018) 336–345.

[5] Y. Liu, S. Yu, H. Wu, Y. Li, S. Wang, Z. Tian, Z. Jiang, High permeability hydrogel membranes of chitosan/polyether-block-amide blends for $CO_2$ separation, J. Membr. Sci. 469 (2014) 198–208, https://doi.org/10.1016/j.memsci.2014.06.050.

[6] R. Castro-Muñoz, K.V. Agrawal, J. Coronas, Ultrathin permselective membranes: the latent way for efficient gas separation, RSC Adv. 10 (21) (2020) 12653–12670, https://doi.org/10.1039/D0RA02254C.

[7] X. Jiang, C.Y. Chuah, K. Goh, R. Wang, A facile direct spray-coating of Pebax® 1657: towards large-scale thin-film composite membranes for efficient $CO_2/N_2$ separation, J. Membr. Sci. 638 (2021) 119708, https://doi.org/10.1016/j.memsci.2021.119708.

[8] Z. Tong, A.K. Sekizkardes, Recent developments in high-performance Membranes for $CO_2$ separation, Membranes 11 (2021) 156, https://doi.org/10.3390/membranes11020156.

[9] X. He, The latest development on membrane materials and processes for post-combustion $CO_2$ Capture: a review, SF J. Material Chem. Eng. 1 (1) (2018) 1009.

[10] J.D. Figueroa, T. Fout, S. Plasynski, H. McIlvried, R.D. Srivastava, Advances in $CO_2$ capture technology—the U.S. Department of Energy's carbon sequestration program, International Journal of Greenhouse Gas Control 2 (1) (2008) 9–20, https://doi.org/10.1016/S1750-5836(07)00094-1.

[11] H. Lin, Z. He, Z. Sun, J. Vu, A. Ng, M. Mohammed, J. Kniep, T.C. Merkel, T. Wu, R.C. Lambrecht, $CO_2$-selective membranes for hydrogen production and $CO_2$ capture – part I: membrane development, J. Membr. Sci. 457 (2014) 149–161, https://doi.org/10.1016/j.memsci.2014.01.020.

[12] T.C. Merkel, H. Lin, X. Wei, R. Baker, Power plant post-combustion carbon dioxide capture: an opportunity for membranes, J. Membr. Sci. 359 (2010) 126–139, https://doi.org/10.1016/j.memsci.2009.10.041.

[13] Carbon Capture, Utilization and Storage: Climate Change, Economic Competitiveness and Energy Security, U.S. Department of Energy, Page (August 2016) 5. https://www.energy.gov/policy/articles/carbon-capture-utilization-and-storage-climate-change-economic-competitiveness-and.

[14] K. Sievert, L. Cameron, A. Carter (Eds.), Why the Cost of Carbon Capture and Storage Remains Persistently High September 2023, International Institute for Sustainable Development, 2023, https://doi.org/10.3929/ethz-b-000664437.

[15] M.H. Nematollahi, P.J. Carvalho, J.A.P. Coutinho, R. Abedini, Recent progress on Pebax-based thin film nanocomposite membranes for $CO_2$ capture: the state of the art and future outlooks, Energy Fuel 36 (2022) 12367–12428, https://doi.org/10.1021/acs.energyfuels.2c01880.

[16] L. Martínez-Izquierdo, A. Perea-Cachero, M. Malankowska, C. Téllez, J. Coronas, A comparative study between single gas and mixed gas permeation of polyether-block-amide type copolymer membranes, J. Environ. Chem. Eng. 10 (5) (2022) 108324, https://doi.org/10.1016/j.jece.2022.108324.

[17] G. Clarizia, P. Bernardo, Polyether block amide as host matrix for nanocomposite Membranes applied to different sensitive fields, Membranes 12 (2022) 1096, https://doi.org/10.3390/membranes12111096.

[18] V.I. Bondar, B.D. Freeman, I. Pinnau, Gas transport properties of poly(ether-b-amide) segmented block copolymers, J. Polym. Sci. B Polym. Phys. 38 (2000) 2051–2062.

[19] J. Didden, R. Thür, A. Volodin, I.F.J. Vankelecom, Blending PPO-based molecules with Pebax MH 1657 in membranes for gas separation, J. Appl. Polym. Sci. (2018), https://doi.org/10.1002/APP.46433.

[20] J.D. Hoffman, G.T. Davis, J.I. Lauritzen Jr. "The Rate of Crystallization of Linear Polymers with Chain Folding", Chapter 7 in "Treatise on Solid State Chemistry", N.B. Hannay (ed.), © Bell Telephone Laboratories, Incorporated 1976, Springer, Boston, MA. https://doi.org/10.1007/978-1-4684-2664-9_7.

[21] J. Yin, A. Raegen, S.H.J. Idziaka, J.A. Forrest, Crystallization and melting of highly monodisperse poly ethylene-oxide, Soft Matter 16 (2020) 7958, https://doi.org/10.1039/d0sm00559b.

[22] H.-G. Braun, E. Meyer, Structure formation of ultrathin PEO films at solid interfaces—complex pattern formation by Dewetting and crystallization, Int. J. Mol. Sci. 14 (2) (2013) 3254–3264, https://doi.org/10.3390/ijms14023254.

[23] X. Bai, H. Li, X. Chu, M. Liu, H. Li, H. Wang, X. Sun, S. Yan, The tuning of crystallization behavior of ferroelectric poly(vinylidene fluoride-co-trifluoroethylene), J. Polym. Sci. 62 (9) (2024) 1742–1770, https://doi.org/10.1002/pol.20230296.

[24] J.D. Hoffman, J.I. Lauritzen Jr., E. Passaglia, G.S. Ross, L.J. Frolen, J.J. Weeks, Kinetics of polymer crystallization from solution and the melt, Kolloid-Zeitschrift und Zeitschrift für Polymere 231 (1–2) (1967) 564–592.

[25] S.R. Reijerkerk, M.H. Knoef, K. Nijmeijer, M. Wessling, Poly(ethylene glycol) and poly(dimethyl siloxane): combining their advantages into efficient $CO_2$ gas separation membranes, J. Membr. Sci. 352 (2010) 126–135, https://doi.org/10.1016/j.memsci.2010.02.008.

[26] W. Wieczorek, Z. Florjanczyk, J.R. Stevens, Composite polyether based solid electrolytes, Electrochim. Acta 40 (13–14) (1995) 2251–2258.

[27] H.T. Ahmed, O.G. Abdullah, Preparation and composition optimization of PEO: MC polymer blend films to enhance electrical conductivity, Polymers 11 (2019) 853, https://doi.org/10.3390/polym11050853.

[28] P. Prabakaran, R.P. Manimuthu, S. Gurusamy, Influence of barium titanate nanofiller on PEO/PVdF-HFP blend-based polymer electrolyte membrane for Li-battery applications, J. Solid State Electrochem. 21 (2017) 1273–1285, https://doi.org/10.1007/s10008-016-3477-z.

[29] O.-H. Kwon, V. Ortalan, A.H. Zewail, Macromolecular structural dynamics visualized by pulsed dose control in 4D electron microscopy 108 (15) (2011) 6026–6031, https://doi.org/10.1073/pnas.1103109108.

[30] J. Militký, M. Venkataraman, R. Mishra, Chapter 12 "the chemistry, manufacture, and tensile behavior of polyamide fibers", in: A.R. Bunsell (Ed.), The Textile Institute Book Series, Handbook of Properties of Textile and Technical Fibres, Second Edition, Woodhead Publishing, 2018, pp. 367–419. ISBN 9780081012727, https://doi.org/10.1016/B978-0-08-101272-7.00012-2.

[31] P. Sharma, Y.-J. Kim, M.-Z. Kim, S.F. Alama, C.H. Cho, A stable polymeric chain configuration producing high performance PEBAX-1657 membranes for $CO_2$ separation, Nanoscale Adv. 1 (7) (2019) 2633–2644, https://doi.org/10.1039/C9NA00170K.

[32] D. Cho, E. Zhmayev, Y.L. Joo, Structural studies of electrospun nylon 6 fibers from solution and melt, Polymer 52 (20) (2011) 4600–4609, https://doi.org/10.1016/j.polymer.2011.07.038.

[33] C.B. Giller, D.B. Chase, J.F. Rabolt, C.M. Snively, Effect of solvent evaporation rate on the crystalline state of electrospun nylon 6, Polymer 51 (18) (2010) 4225–4230, https://doi.org/10.1016/j.polymer.2010.06.057.

[34] F.J. Medellın-Rodrıguez, L. Larios-Lopez, A. Zapata-Espinoza, O. Da valos-Montoya, P.J. Phillips, J.S. Lin, Melting behavior of polymorphics: molecular weight dependence and steplike mechanisms in Nylon-6, Macromolecules 37 (2004) 1799–180.

[35] H. Suzuki, S. Ishii, C. Otani, H. Hoshina, Low-frequency vibrations of polyamide-6 as a function of temperature and thermal history investigated by terahertz absorption spectroscopy, Eur. Polym. J. 67 (2015) 284–291, https://doi.org/10.1016/j.eurpolymj.2015.04.009.

[36] R. Seguela, Overview and critical survey of polyamide6 structural habits: misconceptions and controversies, J. Polym. Sci. 58 (2020) 2971–3003, https://doi.org/10.1002/pol.20200454.

[37] D.R. Holmes, C.W. Bunn, D.J. Smith, The crystal structure of polycaproamide: nylon 6, J. Polym. Sci. 17 (1955) 159.

[38] T. Alfrey Jr, E.B. Bradford, J.W. Vanderhoff, G. Oster, Optical properties of uniform particle-size latexes, J. Opt. Soc. Am. 44 (1954) 603.

[39] H. Arimoto, M. Ishibashi, M. Hirai, Y. Chatani, Crystal structure of the γ-form of nylon 6, J. Polym. Sci. A 3 (1965) 317.

[40] R.L. Miller, Crystallographic data and melting points for various polymers, in: J. Brandrup, E.H. Immergut, E.A. Grulke, A. Abe, D.R. Bloch (Eds.), Polymer Handbook, fourth ed, John Wiley & Sons, Hoboken, New Jersey, USA, 1999 (pp. VI/33).

[41] Y. Li, W.A. Goddard III, Nylon 6 crystal structures, folds, and lamellae from theory, Macromolecules 35 (2002) 8440–8455.

[42] B.D. Cullity, S.R. Stock (Eds.), Appendix 2 "Lattice Geometry" in "Elements of X-Ray Diffraction", 3rd edition, Prentice Hall, New Jersey, 2001 (ISBN 0–201–61091-4).

[43] H.P. Klug, L.E. Alexander, Chapter 1 "Elementary Crystallography" in "X-Ray Diffraction Procedures", 2nd edition, John Wiley and Sons, New York, 1974, ISBN 0-471-49369-4.

[44] D.R. Holmes, C.W. Bunn, D.J. Smith, The crystal structure of polycaproamide: nylon6, J. Polym. Sci. 17 (84) (1955) 159–177, https://doi.org/10.1002/pol.1955.120178401.

[45] X. Zhang, A. Gohn, G. Mendis, J.F. Buzinkai, S.J. Weigand, A.M. Rhoades, Probing three distinct crystal polymorphs of melt-crystallized polyamide 6 by an

integrated fast scanning calorimetry Chip system, Macromolecules 54 (2021) 7512–7528, https://doi.org/10.1021/acs.macromol.1c00811.
[46] E. Parodi, G.W.M. Peters, L.E. Govaert, Structure–properties relations for polyamide 6, part 1: influence of the thermal history during compression moulding on deformation and failure kinetics, Polymers 10 (2018) 710, https://doi.org/10.3390/polym10070710.
[47] C. Millot, Multi-Scale Characterization of Deformation Mechanisms of Bulk Polyamide 6 under Tensile Stretching below and above the Glass Transition, Doctoral Thesis., Materials INSA de Lyon, 2015.
[48] S.T. Correale, N.S. Murthy, Secondary crystallization and premelting endo- and exotherms in oriented polymers, J. Appl. Polym. Sci. 101 (1) (2006) 447–454, https://doi.org/10.1002/app.23267.
[49] A. Ghadimi, M. Amirilargani, T. Mohammadi, N. Kasiri, B. Sadatnia, Preparation of alloyed poly(ether block amide)/poly(ethylene glycol diacrylate) membranes for separation of $CO_2/H_2$ (syngas application), J. Membr. Sci. 458 (2014) 14–26, https://doi.org/10.1016/j.memsci.2014.01.048.
[50] J.D. Hoffman, J.J.J. Weeks, Melting process and the equilibrium melting temperature of polychlorotrifluoroethylene, Res. Natl. Bur. Stand. 66A (1962) 13–28 (J. Res. Natl. Bur. Stand. Sect. A Phys. Chem.).
[51] H. Marand, J. Xu, S. Srinivas, Determination of the equilibrium melting temperature of polymer crystals: linear and nonlinear Hoffman-Weeks extrapolations, Macromolecules 31 (23) (1998) 8219–8229, https://doi.org/10.1021/ma980747y.
[52] D. Pfefferkorn, S.O. Kyerematen, K. Busse, H.-W. Kammer, T. Thurn-Albrecht, J. Kressler, Crystallization and melting of poly(ethylene oxide) in blends and Diblock copolymers with poly(methyl acrylate), Macromolecules 44 (8) (2011) 2953–2963, https://doi.org/10.1021/ma102867d.
[53] B. Wunderlich, G. Czornyj, A study of equilibrium melting of polyethylene, Macromolecules 10 (5) (1977) 906–913.
[54] J. Yin, A. Raegen, S.H.J. Idziak, J.A. Forrest, Crystallization and melting of highly monodisperse poly(ethylene-oxide), Soft Matter 16 (2020) 7958–7969, https://doi.org/10.1039/d0sm00559b.
[55] G.R. Strobl, M. Schneider, Direct evaluation of the Electron density correlation function of partially crystalline polymers, J. Polym. Sci. Polym. Phys. Ed. 18 (1980) 1343–1359, https://doi.org/10.1002/pol.1980.180180614.
[56] S. Wu (Ed.), Polymer Interface and Adhesion, CRC Press Taylor & Francis Group, Boca Raton FL, 1982, ISBN 0824715330 (p.80 & 186).
[57] H. Schonhorn, Heterogeneous nucleation of polymer melts on high-energy surfaces. II. Effect of substrate on morphology and wettability, Macromolecules 1 (2) (1968) 145.
[58] R.L. Miller, Crystallographic data and melting points for various polymers, in: J. Brandrup, E.H. Immergut, E.A. Grulke, A. Abe, D.R. Bloch (Eds.), Polymer Handbook, fourth ed., John Wiley & Sons, Hoboken, New Jersey, USA, 1999 (pp. VI/33 & 53).
[59] A. Xenopoulos, B. Wunderlich, Thermodynamic properties of liquid and semicrystalline linear aliphatic polyamides, J. Polym. Sci. Polym. Phys. 28 (12) (1990) 2271–2290, https://doi.org/10.1002/polb.1990.090281209.
[60] L. Mandelkern, Crystallization kinetics in high polymers. II. Polymer-diluent mixtures, J. Appl. Phys. 26 (4) (1955) 443.
[61] U. Gaur, B. Wunderlich, Heat capacity and other thermodynamic properties of linear macromolecules. III. Polyoxides, J. Phys. Chem. Ref. Data Monogr. 10 (4) (1981) 1001–1049, https://doi.org/10.1063/1.555649.
[62] J.D. Hoffman, J.I. Lauritzen Jr., Crystallization of bulk polymers with chain folding: theory of growth of lamellar Spherulites, J. Research of the National Bureau of Standards-A. Physics and Chemistry 65A (4) (1961) 297–336, https://doi.org/10.6028/jres.065A.035.
[63] Md.M. Rahman, V. Filiz, S. Shishatskiy, C. Abetz, S. Neumann, S. Bolmer, M. M. Khan, V. Abetz, PEBAX® with PEG functionalized POSS as nanocomposite membranes for $CO_2$ separation, J. Membr. Sci. 437 (2013) 286–297, https://doi.org/10.1016/j.memsci.2013.03.001.
[64] A. Bondi, Physical Properties of Molecular Crystals, Liquids, and Glasses, John Wiley & Sons, New York, 1968.
[65] Y.H. Zhao, M.H. Abraham, A.M. Zissimos, Fast calculation of van der Waals volume as a sum of atomic and bond contributions and its application to drug compounds, J. Organomet. Chem. 68 (2003) 7368–7373.
[66] D.W. Van Krevelen, K. Te Nijenhuis (Eds.), Properties of Polymers 4th, Elsevier B. V. Amsterdam, 2009 completely revised edition. (p.83, 84).
[67] W. Yave, A. Car, K.-V. Peinemann, M.Q. Shaikh, K. Rätzke, F. Faupel, Gas permeability and free volume in poly(amide-b-ethylene oxide)/polyethylene glycol blend membranes, J. Membr. Sci. 339 (2009) 177–183.
[68] S. Meshkat, S. Kaliaguine, D. Rodrigue, Mixed matrix membranes based on amine and non-amine MIL-53(Al) in Pebax® MH-1657 for $CO_2$ separation, Sep. Purif. Technol. 200 (2018) 177–190.
[69] P.A. Gamali, A. Kazemi, R. Zadmard, M.J. Anjareghi, A. Rezakhani, R. Rahighi, M. Madani, Distinguished discriminatory separation of $CO_2$ from its methane-containing gas mixture via PEBAX mixed matrix membrane, Chin. J. Chem. Eng. 26 (2018) 73–80.
[70] W. Fam, J. Mansouri, H. Li, V. Chen, Improving $CO_2$ separation performance of thin film composite hollow fiber with Pebax®1657/ionic liquid gel membranes, J. Membr. Sci. 537 (2017) 54–68.
[71] P.D. Sutrisna, J. Hou, H. Li, Y. Zhang, V. Chen, Improved operational stability of Pebax-based gas separation membranes with ZIF-8: a comparative study of flat sheet and composite hollow fibre membranes, J. Membr. Sci. 524 (2017) 266–279.
[72] R.S. Murali, S. Sridhar, T. Sankarshana, Y.V.L. Ravikumar, Gas permeation behavior of Pebax-1657 nanocomposite membrane incorporated with multiwalled carbon nanotubes, Ind. Eng. Chem. Res. 49 (2010) 6530–6538.
[73] S.K. Salestan, A. Rahimpour, R. Abedini, Experimental and theoretical studies of biopolymers on the efficient $CO_2/CH_4$ separation of thin-film Pebax®1657 membrane, Chem. Eng. Process. Process Intensif. 163 (2021) 108366.
[74] F. Amirkhani, M. Mosadegh, M. Asghari, M.J. Parnian, The beneficial impacts of functional groups of CNT on structure and gas separation properties of PEBA mixed matrix membranes, Polym. Test. 82 (2020) 10628, https://doi.org/10.1016/j.polymertesting.2019.106285.
[75] Y. Li, Q. Xin, H. Wu, R. Guo, Z. Tian, Y. Liu, S. Wang, G. He, F. Pan, Z. Jiang, Efficient $CO_2$ capture by humidified polymer electrolyte membranes with tunable water state, Energy Environ. Sci. 7 (2014) 148.
[76] D. Turnbull, M.H. Cohen, Free-volume model of the amorphous phase: glass transition, J. Chem. Phys. 34 (1961) 120–125.
[77] E. Lasseuguette, L. Fielder-Dunton, Q. Jian, M.-C. Ferrari, The effect of solution casting temperature and ultrasound treatment on PEBAX MH-1657/ZIF-8 mixed matrix Membranes morphology and performance, Membr 12 (2022) 584, https://doi.org/10.3390/membranes12060584.
[78] A.A. Jameh, T. Mohammadi, O. Bakhtiari, Preparation of PEBAX-1074/modified ZIF-8 nanoparticles mixed matrix membranes for $CO_2$ removal from natural gas, Sep. Purif. Technol. 231 (2020) 115900.
[79] P. Bernardo, J.C. Jansen, F. Bazzarelli, F. Tasselli, A. Fuoco, K. Friess, P. Izák, V. Jarmarová, M. Kačírková, G. Clarizia, Gas transport properties of Pebax®/room temperature ionic liquid gel membranes, Sep. Purif. Technol. 97 (2012) 73–82, https://doi.org/10.1016/j.seppur.2012.02.041.
[80] K. Jung, S.W. Kang, Effect of functional group ratio in PEBAX copolymer on propylene/propane separation for facilitated olefin transport membranes, Sci. Rep. 9 (2019) 11454, https://doi.org/10.1038/s41598-019-47996-7.
[81] R.S. Murali, K.Y. Rani, T. Sankarshana, A.F. Ismail, S. Sridhar, Separation of binary mixtures of propylene and propane by facilitated transport through silver incorporated poly(ether-block-amide) membranes, oil & gas Science and Technology – rev. IFP Energies nouvelles 70 (2) (2015) 381–390, https://doi.org/10.2516/ogst/2013190.
[82] G. Chatterjee, A.A. Houde, S.A. Stern, Poly(ether urethane) and poly(ether urethane urea) membranes with high $H_2S/CH_4$ selectivity, J. Membr. Sci. 135 (1) (1997) 99–106, https://doi.org/10.1016/S0376-7388(97)00134-8.
[83] J. Sánchez-Laínez, M. Ballester-Catalán, E. Javierre-Ortín, C. Téllez, J. Coronas, Pebax®1041 supported membranes with carbon nanotubes prepared via phase inversion for $CO_2/N_2$ separation, Dalton Trans. 49 (9) (2020) 2905–2913, https://doi.org/10.1039/c9dt04424h.
[84] F. Karamouz, H. Maghsoudi, R. Yegani, Synthesis and characterization of high permeable PEBA membranes for $CO_2/CH_4$ separation, J. Nat. Gas Sci. Eng. 35 (Part A) (2016) 980–985.
[85] X. Guan, Y. Wu, Y. Zheng, B. Zhang, Improved $CO_2/N_2$ separation performance of Pebax-1074 blend membranes containing poly(ethylene glycol), Sci. Prog. 106 (1) (2023), https://doi.org/10.1177/00368504231156295.
[86] Y. Wang, H. Li, G. Dong, C. Scholes, V. Chen, Effect of fabrication and operation conditions on $CO_2$ separation performance of PEO−PA block copolymer membranes, Ind. Eng. Chem. Res. 54 (2015) 7273–7283, https://doi.org/10.1021/acs.iecr.5b01234.
[87] A.A. Jameh, T. Mohammadi, O. Bakhtiari, Preparation of PEBAX-1074/modified ZIF-8 nanoparticles mixed matrix membranes for $CO_2$ removal from natural gas, Sep. Purif. Technol. 231 (2020) 115900, https://doi.org/10.1016/j.seppur.2019.115900.
[88] J. Gao, H. Mao, H. Jin, C. Chen, A. Feldhoff, Y. Li, Functionalized ZIF-7/Pebax® 2533 mixed matrix membranes for $CO_2/N_2$ separation, Microporous Mesoporous Mater. 297 (2020) 110030, https://doi.org/10.1016/j.micromeso.2020.110030.
[89] G. Li, W. Kujawski, A. Tonkonogovas, K. Knozowska, J. Kujawa, E. Olewnik-Kruszkowska, N. Pedišius, A. Stankevičius, Evaluation of $CO_2$ separation performance with enhanced features of materials – Pebax® 2533 mixed matrix membranes containing ZIF-8-PEI@[P(3)HIm][Tf2N], Chem. Eng. Res. Des. 181 (2022) 195–208, https://doi.org/10.1016/j.cherd.2022.03.02.
[90] J.M.P. Scofield, P.A. Gurr, J. Kim, Q. Fu, S.E. Kentish, G.G. Qiao, Development of novel fluorinated additives for high performance $CO_2$ separation thin-film composite membranes, J. Membr. Sci. 499 (2016) 191–200, https://doi.org/10.1016/j.memsci.2015.10.035.
[91] L. Martínez-Izquierdo, M. Malankowska, C. Téllez, J. Coronas, Phase inversion method for the preparation of Pebax® 3533 thin film membranes for $CO_2/N_2$ separation, J. Environ. Chem. Eng. 9 (2021) 105624.
[92] S.R. Armstrong, Novel Applications of Co-Extruded Multilayer Polymeric Films, PhD Thesis, Case Western Reserve University, Cleveland, 2013.
[93] S. Armstrong, B. Freeman, A. Hiltner, E. Baer, Gas permeability of melt-processed poly(ether block amide) copolymers and the effects of orientation, Polymer 53 (6) (2012) 1383–1392, https://doi.org/10.1016/j.polymer.2012.01.037.
[94] M.R. Barzegari, N. Hossieny, D. Jahani, C.B. Park, Characterization of hard-segment crystalline phase of poly(ether-block-amide) (PEBAX®) thermoplastic elastomers in the presence of supercritical $CO_2$ and its impact on foams, Polymer 114 (2017) 15–27, https://doi.org/10.1016/j.polymer.2017.02.088.
[95] V.I. Bondar, B.D. Freeman, I. Pinnau, Gas sorption and characterization of poly (ether-b-amide) segmented block copolymers, J. Polym. Sci. B Polym. Phys. 37 (1999) 2463–2475.
[96] B.K. Doan, G.Q. Chen, C.A. Scholes, Enhanced water/dimethyl ether separation by surface modified PEBAX 1657 membranes containing a nanocomposite layer, Separation and Purification Technology 380 (2026) 135313, https://doi.org/10.1016/j.seppur.2025.135313.

[97] F.H. Akhtar, M. Kumar, K.-V. Peinemann, Pebax®1657/graphene oxide composite membranes for improved water vapor separation, J. Membr. Sci. 525 (2017) 187–194, https://doi.org/10.1016/j.memsci.2016.10.045.

[98] S.C. Park, I.S. Chae, G.H. Moon, B.S. Kim, J. Jang, M. Wessling, Y.S. Kang, Lewis acidic water as a new carrier for facilitating $CO_2$ transport, J Mater Chem A 7 (2019) 5190–5194, https://doi.org/10.1039/c8ta10871d.

[99] Y. Li, Q. Xin, H. Wu, R. Guo, Z. Tian, Y. Liu, S. Wang, G. He, F. Pan, Z. Jiang, Efficient $CO_2$ capture by humidified polymer electrolyte membranes with tunable water state, Energy Environ. Sci. 7 (2014) 1489–1499, https://doi.org/10.1039/c3ee43163k.

[100] W. Fam, J. Mansouri, H. Li, J. Hou, V. Chen, Effect of inorganic salt blending on the $CO_2$ separation performance and morphology of Pebax1657/ionic liquid gel Membranes, Ind. Eng. Chem. Res. 58 (2019) 3304–3313, https://doi.org/10.1021/acs.iecr.8b05027.

[101] G. Chen, T. Wang, G. Zhang, G. Liu, W. Jin, Membrane materials targeting carbon capture and utilization, Advanced Membranes 2 (2022) 100025, https://doi.org/10.1016/j.advmem.2022.100025.

[102] B. Dhuiège, E. Lasseuguette, M.-C. Brochier-Salon, M.-C. Ferrari, K. Missoum, Crosslinked facilitated transport Membranes based on Carboxymethylated NFC and amine-based fixed carriers for carbon Capture, utilization, and storage applications, Appl. Sci. 10 (2020) 414, https://doi.org/10.3390/app10010414.

[103] W. Fam, J. Mansouri, H. Li, J. Hou, V. Chen, Effect of inorganic salt blending on the $CO_2$ separation performance and morphology of Pebax1657/ionic liquid gel Membranes, Ind. Eng. Chem. Res. 58 (2019) 3304–3313.

[104] Y. Li, S. Wang, H. Wu, R. Guo, Y. Liu, Z. Jiang, Z. Tian, P. Zhang, X. Cao, B. Wang, High-performance composite membrane with enriched $CO_2$-philic groups and improved adhesion at the Interface, ACS Appl. Mater. Interfaces 6 (2014) 6654–6663.

[105] Z. Dai, J. Deng, K.-J. Peng, Y.-L. Liu, L. Deng, Pebax/PEG grafted CNT hybrid Membranes for enhanced $CO_2/N_2$ separation, Ind. Eng. Chem. Res. 58 (2019) 12226–12234.

[106] M. Mozafari, R. Abedini, A. Rahimpour, Zr-MOFs-incorporated thin film nanocomposite Pebax 1657 membranes dip-coated on polymethylpentyne layer for efficient separation of $CO_2/CH_4$, J Mater Chem A 6 (2018) 12380.

[107] M.H. Nematollahi, P.J. Carvalho, J.A.P. Coutinho, R. Abedini, Tailoring the $CO_2$ permeation of Pebax1657/polyether imide thin film composite membrane via embedding ag-based metal-organic framework, Chem. Eng. Res. Des. 197 (2023) 109–126, https://doi.org/10.1016/j.cherd.2023.07.028.

[108] Y. Liu, X. Li, Y. Qin, R. Guo, J. Zhang, Pebax–polydopamine microsphere mixed-matrix membranes for efficient $CO_2$ separation, J. Appl. Polym. Sci. 134 (10) (2017) 44564–44574, https://doi.org/10.1002/app.44564.

[109] E.J. Kappert, M.J.T. Raaijmakers, K. Tempelman, F.P. Cuperus, W. Ogieglo, N. E. Benes, Swelling of 9 polymers commonly employed for solvent-resistant nanofiltration membranes: a comprehensive dataset, J. Membr. Sci. 569 (2019) 177–199, https://doi.org/10.1016/j.memsci.2018.09.059.

[110] L. Martínez-Izquierdo, M. Malankowska, C. Téllez, J. Coronas, Phase inversion method for the preparation of Pebax® 3533 thin film membranes for $CO_2/N_2$ separation, J. Environ. Chem. Eng. 9 (2021) 105624.

[111] S. Matavos-Aramyan, G. Bagheri, M.H. Jazebizadeh, Pervaporation separation of toluene from aqueous solutions using Nano-based PEBA/NaX mixed matrix membrane, Silicon 11 (2019) 1725–1730.

[112] M. Najafi, S.M. Mousavi, E. Saljoughi, Preparation and characterization of poly (ether block amide)/graphene membrane for recovery of isopropanol from aqueous solution via pervaporation, Polym. Compos. 39 (2018) 2259–2267.

[113] F. Kadirkhan, P.S. Goh, A.F. Ismail, W.N.F.W. Mustapa, M.H.M. Halim, W.K. Soh, S.Y. Yeo, Recent advances of polymeric Membranes in tackling plasticization and aging for practical industrial $CO_2/CH_4$ applications - a review, Membranes 12 (2022) 71, https://doi.org/10.3390/membranes12010071.

[114] L.M. Robeson, J. Membr. Sci. 320 (1–2) (2008) 390–400, https://doi.org/10.1016/j.memsci.2008.04.030.

[115] X. Wang, Y. Zhang, X. Chen, Y. Wang, M. He, Y. Shan, Y. Li, F. Zhang, X. Chen, H. Kita, Preparation of Pebax 1657/MAF-7 mixed matrix membranes with enhanced $CO_2/N_2$ separation by active site of triazole ligand, Membranes 12 (8) (2022) 786, https://doi.org/10.3390/membranes12080786.

[116] T. Narkkun, W. Kraithong, S. Ruangdit, C. Klaysom, K. Faungnawakij, V. Itthibenchapong, Pebax/modified cellulose nanofiber composite Membranes for highly enhanced $CO_2/CH_4$ separation, ACS Omega 8 (48) (2023) 45428–45437, https://doi.org/10.1021/acsomega.3c04800.

[117] S.A. Habibiannejad, A. Aroujalian, A. Raisi, Pebax-1657 mixed matrix membrane containing surface modified multi-walled carbon nanotubes for gas separation, RSC Adv. 6 (2016) 79563–79577, https://doi.org/10.1039/C6RA14141B.

[118] T. Peters, L. Ansaloni, M.R. De La Viuda, A. Tena, O. Karvan, T. Visser, D. Chinn, N. Bhuwania, Performance and stability of selected polymeric membrane materials for use in high-$H_2S$ and humid natural gas feeds, Ind. Eng. Chem. Res. 64 (2025) 3441–3452, https://doi.org/10.1021/acs.iecr.4c03485.

[119] P.D. Sutrisna, J. Hou, H. Li, Y. Zhang, V. Chen, Improved operational stability of Pebax-based gas separation membranes with ZIF-8: a comparative study of flat sheet and composite hollow fibre membranes, J. Membr. Sci. 524 (2017) 266–279, https://doi.org/10.1016/j.memsci.2016.11.048.

[120] H. Wu, X. Li, Y. Li, S. Wang, R. Guo, Z. Jiang, C. Wu, Q. Xin, X. Lu, Facilitated transport mixed matrix membranes incorporated with amine functionalized MCM-41 for enhanced gas separation properties, J. Membr. Sci. 465 (2014) 78–90, https://doi.org/10.1016/j.memsci.2014.04.023.

[121] K. Shahrezaei, R. Abedini, M. Lashkarbolooki, A. Rahimpour, A preferential $CO_2$ separation using binary phases membrane consisting of Pebax®1657 and [Omim][PF6] ionic liquid, Korean J. Chem. Eng. 36 (2019) 2085–2094, https://doi.org/10.1007/s11814-019-0402-z.

[122] J.E. Shin, S.K. Lee, Y.H. Cho, H.B. Park, Effect of PEG-MEA and graphene oxide additives on the performance of Pebax®1657 mixed matrix membranes for $CO_2$ separation, J. Membr. Sci. 572 (2019) 300–308, https://doi.org/10.1016/j.memsci.2018.11.025.

[123] A.N. Vasileiou, G.V. Theodorakopoulos, D.S. Karousos, M. Bouroushian, A. A. Sapalidis, E.P. Favvas, Nanocarbon-based mixed matrix Pebax-1657 flat sheet Membranes for $CO_2/CH_4$ separation, Membranes 13 (2023) 470, https://doi.org/10.3390/membranes13050470.

[124] C.Z. Liang, F. Feng, J. Wu, T.-S. Chung, Elevating gas separation performance of Pebax-based membranes by blending with a PDMS-PEO block copolymer for $CO_2$ capture and separation, J. Membr. Sci. 716 (2025) 123528, https://doi.org/10.1016/j.memsci.2024.123528.

[125] F. Pazani, A. Aroujalian, Enhanced $CO_2$-selective behavior of Pebax-1657: a comparative study between the influence of graphene-based fillers, Polym. Test. 81 (2020) 106264, https://doi.org/10.1016/j.polymertesting.2019.106264.

[126] S. Meshkat, S. Kaliaguine, D. Rodrigue, Enhancing $CO_2$ separation performance of Pebax® MH-1657 with aromatic carboxylic acids, Sep. Purif. Technol. 212 (2019) 901–912, https://doi.org/10.1016/j.seppur.2018.12.008.

[127] Z. Farashi, S. Azizi, M.R.-D. Arzhandi, Z. Noroozi, N. Azizi, Improving $CO_2/CH_4$ separation efficiency of Pebax-1657 membrane by adding $Al_2O_3$ nanoparticles in its matrix, J. Nat. Gas Sci. Eng. 72 (2019) 103019, https://doi.org/10.1016/j.jngse.2019.103019.

[128] A. Volkov, Membrane Compaction, in: E. Drioli, L. Giorno (Eds.), Encyclopedia of Membranes, Springer, Berlin, Heidelberg, 2014, https://doi.org/10.1007/978-3-642-40872-4_1404-2.

[129] J.H. Kim, W.J. Koros, D.R. Paul, Physical aging of thin 6FDA-based polyimide membranes containing carboxyl acid groups. Part I. Transport properties, Polymer 47 (9) (2006) 3094–3103, https://doi.org/10.1016/j.polymer.2006.02.083.

[130] H.Z. Chen, T.-S. Chung, $CO_2$-selective membranes for hydrogen purification and the effect of carbon monoxide (CO) on its gas separation performance, Int. J. Hydrog. Energy 37 (7) (2012) 6001–6011, https://doi.org/10.1016/j.ijhydene.2011.12.124.

[131] A. Car, W. Yave, Č. Stropnik, K.-V. Peinemann, Pebax®/polyethylene glycol blend thin-film composite membranes for $CO_2$ separation: performance with mixed gases 62 (1) (2008) 110–117, https://doi.org/10.1016/j.seppur.2008.01.001.

[132] W.R. Vieth, K.J. Sladek, A model for diffusion in glassy polymers, J. Colloid Sci. 20 (1965) 1014–1033, https://doi.org/10.1016/0095-8522(65)90012-6.

[133] Z. Tu, P. Zhang, X. Zhang, X. Hu, Y. Wu, Engineering highly reversible hydrogen bonding interaction in Pebax/deep eutectic solvent blended Membranes for efficient separation of $H_2S$ from $CO_2$ and $CH_4$, J. Membr. Sci. 699 (2024) 122618, https://doi.org/10.1016/j.memsci.2024.122618.

[134] S. Rao, B. Prasad, Y. Han, W.S.W. Ho, Polymeric Membranes for $H_2S$ and $CO_2$ removal from natural gas for Hydrogen Production: a review, Energies 16 (2023) 5713, https://doi.org/10.3390/en16155713.

[135] D.J. Harrigan, J. Yang, B.J. Sundell, J.A. Lawrence, J.T. O'Brien, M.L. Ostraat, Sour gas transport in poly(ether-b-amide) membranes for natural gas separations, J. Membr. Sci. 595 (2020) 117497, https://doi.org/10.1016/j.memsci.2019.117497.

[136] J. Kniep, H. Lin, S. Thomas-Droz, Z. He, K. Amo, Z. Sun, M. Mohammad, J. Vu, T. Merkel, Field Tests of MTR Membranes for Syngas Separations: Final Report of $CO_2$-Selective Membrane Field Test Activities at the National Carbon Capture Center December 15, Membrane Technology and Research, Inc., 39630 Eureka Drive Newark, CA 94560, 2017.

[137] E.H. Cho, K.B. Kim, J.W. Rhim, Transport properties of PEBAX blended Membranes with PEG and Glutaraldehyde for $SO_2$ and other gases, Polymer Korea 38 (6) (2014) 687–693, https://doi.org/10.7317/pk.2014.38.6.687.

[138] H.H. Beiragh, M. Omidkhah, R. Abedini, T. Khosravi, S. Pakseresht, Synthesis and characterization of poly (ether-block-amide) mixed matrix membranes incorporated by nanoporous ZSM-5 particles for $CO_2/CH_4$ separation, Asia Pac. J. Chem. Eng. 11 (2016) 522–532, https://doi.org/10.1002/apj.1973.

[139] L.G. Boutsika, C. Tampaxis, K. Papadokostaki, M. Sanopoulou, G. Charalambopoulou, I. Bratsos, T. Steriotis, Uio-based mixed matrix membranes for efficient $CO_2$ separations, ChemPlusChem (2025) e202500151, https://doi.org/10.1002/cplu.202500151.

[140] T. Eljaddi, J. Bouillon, D. Roizard, L. Lebrun, Pebax-based composite membranes with high transport properties enhanced by ZIF-8 for $CO_2$ separation, Membranes 12 (2022) 836, https://doi.org/10.3390/membranes12090836.

[141] E.G. Estahbanati, M. Omidkhah, A.E. Amooghin, Preparation and characterization of novel ionic liquid/Pebax membranes for efficient $CO_2$/light gases separation, J. Ind. Eng. Chem. 51 (2017) 77–89, https://doi.org/10.1016/j.jiec.2017.02.017.

[142] R.L. Thankamony, X. Li, S.K. Das, M.M. Ostwal, Z. Lai, Porous covalent triazine piperazine polymer (CTPP)/PEBAX mixed matrix membranes for $CO_2/N_2$ and $CO_2/CH_4$ separations, J. Membr. Sci. 591 (2019) 117348, https://doi.org/10.1016/j.memsci.2019.117348.

[143] S. Mosleh, M.R. Mozdianfard, G. Khanbabaei, ZIF-8 incorporated in an optimized Pebax®1657/PES membrane for pure and mixed $CO_2/CH_4$ gas separation, Chem. Eng. Technol. 46 (00) (2023) 1–11, https://doi.org/10.1002/ceat.202300174.

[144] Y. Liu, C. Wu, Z. Zhou, W. Liu, H. Guo, B. Zhang, Upgrading $CO_2/CH_4$ separation performances of Pebax-based mixed-matrix membranes incorporated with core/shell-structured ZIF-L(CO)@ZIF-8 composite nanosheets, J. Membr. Sci. 659 (2022) 120787, https://doi.org/10.1016/j.memsci.2022.120787.

[145] H.R. Afshoun, M.P. Chenar, A.F. Ismail, Effect of coating method and feed pressure and temperature on $CO_2/CH_4$ gas separation performance of Pebax/PES composite Membranes, Journal of Gas Technology 3 (2018) 48–59.

[146] L. Martínez-Izquierdo, C. García-Comas, S. Dai, M. Navarro, A. Tissot, C. Serre, C. Téllez, J. Coronas, Ultrasmall functionalized UiO-66 nanoparticle/polymer Pebax 1657 thin-film nanocomposite Membranes for optimal $CO_2$ separation, ACS Appl. Mater. Interfaces 16 (3) (2024) 4024–4034, https://doi.org/10.1021/acsami.3c16093.

[147] H.Z. Ferrari, F. Bernard, L. dos Santos, G. Dias, C. Le Roux, P. Micoud, F. Martin, S. Einloft, Enhancing $CO_2/N_2$ and $CO_2/CH_4$ separation in mixed matrix membrane: a comprehensive study on Pebax®1657 with SSMMP/IL for improved efficiency, Polym. Eng. Sci. 64 (6) (2024) 2875–2893, https://doi.org/10.1002/pen.26732.

[148] D. Nobakht, R. Abedini, Improved gas separation performance of Pebax®1657 membrane modified by poly-alcoholic compounds, J. Environ. Chem. Eng. 10 (3) (2022) 107568, https://doi.org/10.1016/j.jece.2022.107568.

[149] M. Li, X. Zhang, S. Zeng, L. Bai, H. Gao, J. Deng, Q. Yang, S. Zhang, Pebax-based composite membranes with high gas transport properties enhanced by ionic liquids for $CO_2$ separation, RSC Adv. 7 (2017) 6422–6431, https://doi.org/10.1039/c6ra27221e.

[150] S. Fujikawa, M. Ariyoshi, R. Selyanchyn, T. Kunitake, Ultra-fast, selective $CO_2$ permeation by free-standing siloxane Nanomembranes, Chem. Lett. 48 (11) (2019) 1351–1354, https://doi.org/10.1246/cl.190558.

[151] G. Firpo, E. Angeli, L. Repetto, U. Valbusa, Permeability thickness dependence of polydimethylsiloxane (PDMS) membranes, J. Membr. Sci. 481 (2015) 1–8, https://doi.org/10.1016/j.memsci.2014.12.043.

[152] Richard W. Baker (Ed.), Membrane Technology and Applications, 3rd Edition July, John Wiley & Sons ltd, Chichester, United Kingdom, 2012, ISBN 978-1-118-35969-3 (Figure 3.26).

[153] X. Li, Q. Huang, Y. Liu, B. Zhao, J. Li, Review of the Hydrogen Permeation Test of the Polymer Liner Material of Type IV On-Board Hydrogen Storage Cylinders, Materials (Basel) 16 (15) (2023), https://doi.org/10.3390/ma16155366, 5366.

[154] T.-H. Huang, F. Feng, T.-S. Chung, Pebax®1657-based membranes with organic gatekeepers for effective $CO_2$ capture, Chem. Eng. J. 513 (2025) 162596, https://doi.org/10.1016/j.cej.2025.162596.

[155] C. Pei, N. Wang, Y. Zhang, Y. Zhong, X. Liu, J. Hou, Y. Yuan, R. Zhang, A novel UIO-66/Pebax® 1657 mixed matrix membrane exhibiting superior $CO_2$ separation performance via nonthermal air plasma modification, ChemistrySelect 10 (11) (2025) e202405440, https://doi.org/10.1002/slct.202405440.

[156] A. Hosseinkhani, P. Safari, M.A. Omidkhah, E. Amooghin, A.M. Norouzi, A high-efficiency Pebax® 1657-based mixed matrix membrane containing molybdenum oxide particles for enhanced $CO_2/N_2$ separation, Int. J. Environ. Sci. Technol. 22 (2025) 6847–6862, https://doi.org/10.1007/s13762-025-06391-8.

[157] Y. Zhang, Y. Tong, X. Li, S. Guo, H. Zhang, X. Chen, K. Cai, L. Cheng, W. He, Pebax mixed-matrix membrane with highly dispersed ZIF-8@CNTs to enhance $CO_2/N_2$ separation, ACS Omega 6 (29) (2021) 18566–18575, https://doi.org/10.1021/acsomega.1c00493.

[158] F. Guo, D. Li, R. Ding, J. Gao, X. Ruan, X. Jiang, G. He, W. Xiao, Constructing MOF-doped two-dimensional composite material ZIF-90@$C_3N_4$ mixed matrix membranes for $CO_2/N_2$ separation, Sep. Purif. Technol. 280 (2022) 119803, https://doi.org/10.1016/j.seppur.2021.119803.

[159] J.H. Kim, S.Y. Ha, Y.M. Lee, Gas permeation of poly(amide-6-b-ethylene oxide) copolymer, J. Membr. Sci. 190 (2001) 179–193, https://doi.org/10.1016/S0376-7388(01)00444-6.

[160] P. Bernardo, G. Clarizia, Enhancing gas permeation properties of Pebax® 1657 Membranes via Polysorbate nonionic surfactants doping, Polymers 12 (2) (2020) 253, https://doi.org/10.3390/polym12020253.

[161] F. Shi, J. Sun, J. Wang, M. Liu, S. Wang, X. Cao, Z. Yan, Y. Li, S.P. Nunes, Exploration of the synergy between 2D nanosheets and a non-2D filler in mixed matrix membranes for gas separation, Front. Chem. 8 (2020) 58, https://doi.org/10.3389/fchem.2020.00058.

[162] H. Wang, W. Zheng, X. Yang, M. Ning, X. Li, Y. Xi, X. Yan, X. Zhang, Y. Dai, H. Liu, G. He, Pebax-based mixed matrix membranes derived from microporous carbon nanospheres for permeable and selective $CO_2$ separation, Sep. Purif. Technol. 274 (2021) 119015, https://doi.org/10.1016/j.seppur.2021.119015.

[163] F. Guo, B. Li, R. Ding, D. Li, X. Jiang, G. He, W. Xiao, A novel composite material UiO-66@HNT/Pebax mixed matrix membranes for enhanced $CO_2/N_2$ separation, Membranes 11 (2021) 693, https://doi.org/10.3390/membranes11090693.

[164] O. Selyanchyn, R. Selyanchyn, Sh. Fujikawa, A critical role of the molecular interface in double-layered Pebax-1657/PDMS nanomembranes on highly efficient $CO_2/N_2$ gas separation, ACS Appl. Mater. Interfaces 12 (29) (2020) 33196–33209, https://doi.org/10.1021/acsami.0c07344.

[165] Y. Chen, B. Wang, L. Zhao, P. Dutta, W.S.W. Ho, New Pebax/zeolite Y composite membranes for $CO_2$ capture from flue gas, J. Membr. Sci. 495 (2015) 415–423, https://doi.org/10.1016/j.memsci.2015.08.045.

[166] R. Selyanchyn, M. Ariyoshi, S. Fujikawa, Thickness effect on $CO_2/N_2$ separation in double layer Pebax-1657®/PDMS Membranes, Membranes 8 (2018) 121, https://doi.org/10.3390/membranes8040121.

[167] J. Liu, Y. Pan, J. Xu, Z. Wang, H. Zhu, G. Liu, J. Zhong, W. Jin, Introducing amphipathic copolymer into intermediate layer to fabricate ultra-thin Pebax composite membrane for efficient $CO_2$ capture, J. Membr. Sci. 667 (2023) 121183, https://doi.org/10.1016/j.memsci.2022.121183.

[168] X. Jiang, K. Goh, R. Wang, Air plasma assisted spray coating of Pebax-1657 thin-film composite membranes for post-combustion $CO_2$ capture, J. Membr. Sci. 658 (2022) 120741, https://doi.org/10.1016/j.memsci.2022.120741.

[169] H.Z. Chen, Z. Thong, P. Li, Tai-Shung Chung, High performance composite hollow fiber membranes for $CO_2/H_2$ and $CO_2/N_2$ separation, Int. J. Hydrog. Energy 39 (2014) 5043–5053, https://doi.org/10.1016/j.ijhydene.2014.01.047.

[170] Y. Wang, T. Hu, H. Li, G. Dong, W. Wong, V. Chen, Enhancing membrane permeability for $CO_2$ capture through blending commodity polymers with selected PEO and PEO-PDMS copolymers and composite hollow fibres, Energy Procedia 63 (2014) 202–209, https://doi.org/10.1016/j.egypro.2014.11.021.

[171] S. Singh, K.C. Khulbe, T. Matsuura, P. Ramamurthy, Membrane characterization by solute transport and atomic force microscopy, J. Membr. Sci. 142 (1998) 111–127, https://doi.org/10.1016/S0376-7388(97)00329-3.

[172] K.J. Kim, A.G. Fane, R.B. Aim, M.G. Liu, G. Jonsson, I.C. Tessaro, A.P. Broek, D. Bargeman, A comparative study of techniques used for porous membrane characterization: pore characterization, J. Membr. Sci. 87 (1–2) (1994) 35–46, https://doi.org/10.1016/0376-7388(93)E0044-E.

[173] L. Martínez-Izquierdo, C. Téllez, J. Coronas, Highly stable Pebax® renew® thin-film nanocomposite membranes with metal organic framework ZIF-94 and ionic liquid [Bmim][BF4] for $CO_2$ capture, J Mater Chem A 10 (2022) 18822, https://doi.org/10.1039/D2TA03958C.

[174] A. Breen, R. Baker, P. Behm, B. Freeman, P. Hao, T. Hofmann, J. Kniep, T. Merkel, W. Salim, R. McKaskle, D. Pierik, W. Morris, Large pilot testing of MTR'S membrane-based post-combustion $CO_2$ capture process, SSRN 5070818 (2025), https://doi.org/10.2139/ssrn.5070818.

[175] B. Comesana-Gandara, J. Chen, C.G. Bezzu, M. Carta, I. Rose, M.-C. Ferrari, E. Esposito, A. Fuoco, J.C. Jansen, N.B. McKeown, Redefining the Robeson upper bounds for $CO_2/CH_4$ and $CO_2/N_2$ separations using a series of ultrapermeable benzotriptycene based polymers of intrinsic microporosity, Energy Environ. Sci. 12 (2019) 2733, https://doi.org/10.1039/c9ee01384a.

[176] P.M. Visakh, O.B. Nazarenko (Eds.), Nanostructured Polymer Membranes vol. 2: Applications, chapter 4.6.1, Scrivener publishing LLC Beverly, Massachusetts and John Wiley & Sons Inc., Hoboken, New Jersey, 2016, p. 195. Table 4.5.

[177] D. Li, R. Wang, T.-S. Chung, Fabrication of lab-scale hollow fiber membrane modules with high packing density, Sep. Purif. Technol. 40 (1) (2004) 15–30, https://doi.org/10.1016/j.seppur.2003.12.019.

[178] A. Gökaltun, Y.B. (Abraham) Kang, M.L. Yarmush, O.B. Usta, A. Asatekin, Simple surface modification of poly(dimethylsiloxane) via surface segregating smart polymers for biomicrofluidics, Sci. Rep. 9 (2019) 7377, https://doi.org/10.1038/s41598-019-43625-5.

[179] M.G. Freire, P.J. Carvalho, A.J. Queimada, I.M. Marrucho, J.A.P. Coutinho, Surface tension of liquid Fluorocompounds, J. Chem. Eng. Data 51 (2006) 1820–1824, https://doi.org/10.1021/je060199g.

[180] T.C. Merkel, V.I. Bondar, K. Nagai, B.D. Freeman, I. Pinnau, Gas sorption, diffusion, and permeation in poly(dimethylsiloxane), journal of polymer science: part B: polymer, Physics 38 (2000) 415–434, https://doi.org/10.1002/(SICI)1099-0488(20000201)38:3<415::AID-POLB8>3.0.CO;2-Z.

[181] S.M. Allen, M. Fujii, V. Stannett, H.B. Hopfenberg, J.L. Williams, The barrier properties of polyacrylonitrile, J. Membr. Sci. 2 (1977) 153–164.

[182] L. Laysandra, C.-H. Chuang, S. Kobayashi, A.-N. Au-Duong, Y.-H. Cheng, Y.-T. Li, M.M. Mburu, T. Isono, T. Satoh, Y.-C. Chiu, Design of self-cross-linkable poly(n-butyl acrylate)-co-poly[N-(hydroxymethyl)acrylamide] amphiphilic copolymers toward elastic and self-healing properties, ACS Appl. Polym. Mater. 2 (12) (2020) 5432–5443, https://doi.org/10.1021/acsapm.0c00760.

[183] D. Kim, S.-H. Kim, J.Y. Park, Floating-on-water fabrication method for thin polydimethylsiloxane Membranes, Polymers 11 (2019) 1264, https://doi.org/10.3390/polym11081264.

[184] M. Kattula, K. Ponnuru, L.X. Zhu, W.G. Jia, H.Q. Lin, E.P. Furlani, Designing ultrathin film composite membranes: the impact of a gutter layer, Sci. Rep. 5 (2015) 15016, https://doi.org/10.1038/srep15016.

[185] C. Zhao, X. Zhou, Y. Yue, Determination of pore size and pore size distribution on the surface of hollow-fiber filtration membranes: a review of methods, Desalination 129 (2) (2000) 107–123, https://doi.org/10.1016/S0011-9164(00)00054-0.

[186] D. Kalmykov, A. Balynin, A. Yushkin, E. Grushevenko, S. Sokolov, A. Malakhov, A. Volkov, S. Bazhenov, Membranes based on PTMSP/PVTMS blends for membrane contactor applications, Membranes 12 (2022) 1160, https://doi.org/10.3390/membranes12111160.

[187] R. Srinivasan, S.R. Auvil, P.M. Burban, Elucidating the mechanism(s) of gas transport in poly[1-(trimethylsilyl)-1-propyne] (PTMSP) membranes, J. Membr. Sci. 86 (1–2) (1994) 67–86, https://doi.org/10.1016/0376-7388(93)E0128-7.

[188] T. Li, Y. Pan, K.-V. Peinemann, Z. Lai, Carbon dioxide selective mixed matrix composite membrane containing ZIF-7 nano-fillers, J. Membr. Sci. 425 (426) (2013) 235–242, https://doi.org/10.1016/j.memsci.2012.09.006.

[189] H. Li, W. Fam, P. Satrisna, J. Hou, V. Chen, New generation high performance composite hollow fiber membranes for low cost $CO_2$, in: 14th Greenhouse Gas Control Technologies Conference Melbourne 21–26 October 2018 (GHGT-14), 2018, https://doi.org/10.2139/ssrn.3365554.

[190] Y. Zhang, Y. Shen, J. Hou, Y. Zhang, W. Fam, J. Liu, T.D. Bennett, V. Chen, Ultraselective Pebax membranes enabled by templated microphase separation, ACS Appl. Mater. Interfaces 10 (2018) 20006–20013, https://doi.org/10.1021/acsami.8b03787.

[191] K. Berean, J.Z. Ou, M. Nour, K. Latham, C. McSweeney, D. Paull, A. Halim, S. Kentish, C.M. Doherty, A.J. Hill, K. Kalantar-Zadeh, The effect of crosslinking temperature on the permeability of PDMS membranes: evidence of extraordinary $CO_2$ and $CH_4$ gas permeation, Sep. Purif. Technol. 122 (2014) 96–104, https://doi.org/10.1016/j.seppur.2013.11.006.

[192] Y. Shen, H. Wang, X. Zhang, Y. Zhang, $MoS_2$ nanosheets functionalized mixed matrix membrane for enhanced $CO_2$ capture via surface drop-coating method, ACS Appl. Mater. Interfaces 8 (2016) 23371–23378.
[193] L. Hu, J. Cheng, Y. Li, J. Liu, J. Zhou, K. Cen, In-situ grafting to improve polarity of polyacrylonitrile hollow fiber-supported polydimethylsiloxane membranes for $CO_2$ separation, J. Colloid Interface Sci. 510 (2018) 12–19, https://doi.org/10.1016/j.jcis.2017.09.048.
[194] L. Wang, Y. Li, S. Li, P. Ji, C. Jiang, Preparation of composite poly(ether block amide) membrane for $CO_2$ capture, J. Energy Chem. 23 (2014) 717–725.
[195] T. Hong, Z. Niu, X. Hu, K. Gmernicki, S. Cheng, F. Fan, J.C. Johnson, E. Hong, S. Mahurin, D. Jiang, B. Long, J. Mays, A. Sokolov, T. Saito, Effect of cross-link density on carbon dioxide separation in polydimethylsiloxane-Norbornene Membranes, Chem. Sus. Chem. 8 (21) (2015) 3595–3604, https://doi.org/10.1002/cssc.201500903.
[196] D.S. Karousos, G.V. Theodorakopoulos, F. Chiesa, S. Barbe, M. Bouroushian, E. P. Favvas, $CO_2/CH_4$ and $CO_2$/CO selective Pebax-1657 based composite hollow fiber membranes prepared by a novel dip-coating technique, Separations 12 (2025) 3, https://doi.org/10.3390/separations12010003.
[197] G.V. Theodorakopoulos, D.S. Karousos, S. Rekleiti, E.P. Favvas, Fundamentals, advancements and challenges of $CO_2$/CO separation through polymeric membranes, 2025, https://doi.org/10.1080/15422119.2025.2571763 in press.
[198] C.-Y. Park, B.-J. Chang, J.-H. Kim, Y.M. Lee, UV-crosslinked poly(PEGMA-CO-MMA-CO-BPMA) membranes: synthesis, characterization, and $CO_2/N_2$ and $CO_2$/CO separation, J. Membr. Sci. 587 (2019) 117167, https://doi.org/10.1016/j.memsci.2019.06.007.
[199] S.L. Liu, L. Shao, M.L. Chua, C.H. Lau, H. Wang, S. Quan, Recent progress in the design of advanced PEO-containing membranes for $CO_2$ removal, Prog. Polym. Sci. 38 (7) (2013) 1089–1120, https://doi.org/10.1016/j.progpolymsci.2013.02.002.
[200] A. Car, C. Stropnik, W. Yave, K.-V. Peinemann, Pebax®/polyethylene glycol blend thin film composite membranes for CO2 separation: performance with mixed gases, Sep. Purif. Technol. 62 (2008) 110–117.
[201] B. Yu, H. Cong, Z. Li, J. Tang, X.S. Zhao, Pebax-1657 nanocomposite membranes incorporated with nanoparticles/colloids/carbon nanotubes for $CO_2/N_2$ and $CO_2/H_2$ separation, J. Appl. Polym. Sci. 130 (2013) 2867–2876, https://doi.org/10.1002/app.39500.
[202] Y. Wu, D. Zhao, S. Chen, J. Ren, K. Hua, H. Li, M. Deng, The effect of structure change from polymeric membrane to gel membrane on $CO_2$ separation performance, Sep. Purif. Technol. 261 (2021) 118243.
[203] A.A. Shamsabadi, A.P. Isfahani, S.K. Salestan, A. Rahimpour, B. Ghalei, E. Sivaniah, M. Soroush, Pushing rubbery polymer Membranes to be economic for $CO_2$ separation: embedment with $Ti_3C_2Tx$ MXene Nanosheets, ACS Appl. Mater. Interfaces 12 (2020) 3984–3992, https://doi.org/10.1021/acsami.9b19960.
[204] A. Car, C. Stropnik, W. Yave, K.-V. Peinemann, PEG modified poly(amide-b-ethylene oxide) membranes for $CO_2$ separation, J. Membr. Sci. 307 (2008) 88–95, https://doi.org/10.1016/j.memsci.2007.09.023.
[205] D. Nedeljkovic, The effect of the temperature and moisture to the permeation properties of PEO-based Membranes for carbon-dioxide separation, Polymers 13 (2021) 2053.
[206] E. Esposito, R. Bruno, M. Monteleone, A. Fuoco, J.F. Soria, E. Pardo, D. Armentano, J.C. Jansen, Glassy PEEK-WC vs. rubbery Pebax®1657 polymers: effect on the gas transport in CuNi-MOF based mixed matrix membranes, Appl. Sci. 10 (2020) 1310, https://doi.org/10.3390/app10041310.
[207] A. Jomekian, B. Bazooyar, R.M. Behbahani, T. Mohammadi, A. Kargari, Ionic liquid-modified Pebax® 1657 membrane filled by ZIF-8 particles for separation of $CO_2$ from $CH_4$, $N_2$ and $H_2$, J. Membr. Sci. 524 (2017) 652–662.
[208] S. Meshkat, S. Kaliaguine, D. Rodrigue, Mixed matrix membranes based on amine and non-amine MIL-53(Al) in Pebax® MH-1657 for $CO_2$ separation, Sep. Purif. Technol. 200 (2018) 177–190, https://doi.org/10.1016/j.seppur.2018.02.038.
[209] G. Huang, A.P. Isfahani, A. Muchtar, K. Sakurai, B.B. Shrestha, D. Qin, D. Yamaguchi, E. Sivaniah, B. Ghalei, Pebax/ionic liquid modified graphene oxide mixed matrix membranes for enhanced $CO_2$ capture, J. Membr. Sci. 565 (2018) 370–379, https://doi.org/10.1016/j.memsci.2018.08.026.
[210] I.R. Mazzei, D. Nikolaeva, A. Fuoco, S. Loïs, S. Fantini, M. Monteleone, E. Esposito, S.J. Ashtiani, M. Lanč, O. Vopička, K. Friess, I.F.J. Vankelecom, J. C. Jansen, Poly[3-ethyl-1-vinyl-imidazolium] diethyl phosphate/Pebax® 1657 composite membranes and their gas separation performance, Membranes 10 (2020) 224, https://doi.org/10.3390/membranes10090224.
[211] D. Zhao, J. Ren, H. Li, X. Li, M. Deng, Gas separation properties of poly(amide-6-b-ethylene oxide)/amino modified multi-walled carbon nanotubes mixed matrix membranes, J. Membr. Sci. 467 (2014) 41–47, https://doi.org/10.1016/j.memsci.2014.05.009.
[212] G.V. Theodorakopoulos, D.S. Karousos, K.G. Mansouris, A.A. Sapalidis, E. P. Kouvelos, E.P. Favvas, Graphene nanoplatelets based polyimide/Pebax dual-layer mixed matrix hollow fiber membranes for $CO_2/CH_4$ and $He/N_2$ separations, International Journal of Greenhouse Gas Control 114 (2022) 103588, https://doi.org/10.1016/j.ijggc.2022.103588.
[213] H. Lin, S.M. Thompson, A. Serbanescu-Martin, J.G. Wijmans, K.D. Amo, K. A. Lokhandwala, T.C. Merkel, Dehydration of natural gas using membranes. Part I: composite membranes, J. Membr. Sci. 413-414 (2012) 70–81, https://doi.org/10.1016/j.memsci.2012.04.009.
[214] F. Pardo, G. Zarca, A. Urtiaga, Effect of feed pressure and long-term separation performance of Pebax-ionic liquid membranes for the recovery of difluoromethane (R32) from refrigerant mixture R410A, J. Membr. Sci. 618 (2021) 118744, https://doi.org/10.1016/j.memsci.2020.118744.